



Norwegian University of
Science and Technology

Disturbance rejection of a High Speed Hydrofoil Craft using a Frequency Weighted H₂-Optimal Controller

Erik Bakkevig Piene

Marine Technology

Submission date: February 2018

Supervisor: Vahid Hassani, IMT

Norwegian University of Science and Technology
Department of Marine Technology

Preface

This master thesis has been written fall 2017 and beginning of winter 2018 at Norwegian University of Science and Technology (NTNU), Department of Marine Technology. The thesis is an extension of the work done in the author's project thesis, which can be found in the paper Piene (2017). While the project thesis focused on using conventional proportional-integral-derivative controllers in order to stabilize a fully submerged hydrofoil craft in calm water, this master thesis focuses on using more sophisticated optimal control theory in order to both stabilize and minimize the effect of disturbances on a similar craft when it is exposed to waves. The master thesis will in this report be presented as an independent study including all the information necessary for the reader. However, it is expected that the reader has some knowledge about linear algebra, basic control theory and maritime terms. MATLAB/Simulink is used for modelling and simulations, where all the code and the Simulink model is developed by the author.

The author want to give a great thank to his supervisor, Vahid Hassani, for providing inspiration, recommendations and relevant literature, as well as good motivation. A great thank also goes to the professors that have organized relevant courses at NTNU and written lecture notes used in the work with this thesis.

The topic was selected in order to contribute to the current *Flying Foil* project by NTNU Technology Transfer AS, where John Martin Kleven Godø and Jarle Vinje Kramer are working on reborn the hydrofoil passenger craft by using new technology. The author wishes John Martin and Jarle their best luck in realizing their *Flying Foil* project.

Abstract

The study presented in this report look into the design of a Ride Control System reducing wave-induced motions in heave, roll and pitch on a fully submerged hydrofoil craft sailing at 17 m/s. A frequency weighted, multiple-input multiple-output \mathcal{H}_2 -optimized feedback controller is used.

The craft is modelled in 6 Degrees of Freedom with nonlinear models for rigid-body dynamics and foil forces. Four identical and symmetrically located foils are carrying the weight of the craft, and four identical and symmetrically located rudders are controlling motions in yaw. The only external forces and moments acting on the craft-body are gravity, lift and drag forces from the foils and rudders, and a thrust force in surge keeping the speed constant. No air or other water resistance is modelled. The wave disturbances are implemented by letting the orbital motions of water particles change the magnitude and direction of the relative inflow velocity on the foils. These orbital motions are calculated from a linear model of one or more regular wave components. The craft model has four generalized control inputs, where three of them are controlling heave, roll and pitch by adjusting the angles of the lifting foils differently, and the fourth is controlling yaw by adjusting the rudder angles.

The simulation model of the craft is then linearized with respect to motions in heave, roll and pitch. The linearization is done about a trim condition with zero angles in roll and pitch, a constant position in heave, and zero velocity in all degrees of freedom, except for the constant speed in surge. Only control inputs for heave, roll and pitch are included. The linearized model is expressed as a nine-dimensional state-space model, where first three states are generalized actuator dynamics, and the last six are position and velocity in heave, roll and pitch.

The linearized model is then augmented with first-order frequency-weighting functions, in order to generate performance signals with frequency-dependent sensitivity to state errors and control inputs. The higher value of the performance signal, the higher penalty on the corresponding state error or control input. The state errors are given penalty at low frequencies, and the control inputs are given penalty at high frequencies. Additional frequency-weighting functions are used in order to transform white-noise signals into expected, colored wave disturbances. These white noise-signals, together with white sensor noise and reference state values, constitute the external inputs in the augmented model.

The \mathcal{H}_2 -optimized controller is minimizing the 2-norm of the closed-loop transfer matrix from external inputs to the performance signals. It is computed from the augmented model by using the `h2syn()` function in the Robust Control Toolbox in MATLAB. The yaw rate and surge speed of the craft is controlled by separate, external proportional-integral-derivative controllers, and the speed in sway is controlled to zero with an external proportional-integral controller updating the reference for the roll angle.

Simulink is used to simulate the system of the controlled craft in three different sea conditions: Regular long-crested waves, irregular long-crested waves, and irregular short-crested waves. For each sea condition, straight-line motion in both following and head sea is simulated. A coordinated turn is also simulated in irregular, short-crested waves. In total seven different cases are simulated. Sensor noise is added to the signals entering the \mathcal{H}_2 controller, but not the external controllers.

Simulation results shows that the Ride Control System in all of the cases is able to control the attitude of the craft, as well as reducing the wave-induced disturbances. Performance is better in regular than in irregular waves, better in short-crested than in long-crested irregular waves, and better in following sea than in head sea. The last is due to the choice of frequency-weighting functions for the error performance signals, since they are giving less penalty on errors caused by higher encounter frequencies. The results do also show large pitch accelerations in the case of head sea with long-crested, irregular waves. The choice of weighting functions is a trade-off between good performance, and minimization of sensor noise penetrating the controller and causing high-frequency vibrations in the actuators. Higher order weighting functions or a more accurate linearized model can reduce the problem.

Sammendrag

Arbeidet som er presentert i denne rapporten tar for seg design av et kontrollsystem for reduksjon av bølgeinduserte bevegelser i hiv, rull og stamp på en hydrofoilbåt med fult neddykkede foiler. Båten antas å ha en konstant fart på 17 m/s. Kontrollsystemet vil primært være basert på en frekvensvektet \mathcal{H}_2 -optimalisert feedback-kontroller.

Hydrofoilmartøyet er modellert i 6 frihetsgrader, med ulineære modeller for både stivt-legeme-dynamikk og hydrodynamiske krefter som virker på foilene. Martøyet bæres av fire identiske foiler som er symmetrisk plassert i både lengde- og bredderetning, mens fire identiske og symmetrisk plasserte ror styrer martøyet i gir. De eneste eksterne kreftene som virker på martøyet er tyngdekraft, løft- og drag-krefter fra foiler og ror, og en fremoverrettet skyvkraft som holder farten konstant. Luftmotstand og hydrodynamiske krefter fra andre deler enn foiler og ror er neglisjert. Bølgeinduserte forstyrrelser er implementert ved å la vannpartiklenes lokale orbitale hastighet inngå i beregningen av relativ hastighet mellom foil/ror og vann. Slik medfører bølgene endringer i fart og retning på vannet som strømmer in mot foilen/roret, og derav også endring i størrelse og retning på de relaterte hydrodynamiske kreftene. Vannpartiklenes hastighet beregnes ut fra en lineær bølgemodell bestående av en eller flere regulære komponenter av sinusformede bølger. Modellen kontrolleres med fire generaliserte, inngående signaler, derav tre kontrollerer krefter i hiv, rull og stamp ved å allokere ulike vinkelendringer på foilene, og den siste kontrollerer gir ved å justere vinkelen på rorene.

Simuleringsmodellen er deretter linearisert med hensyn på frihetsgradene hiv, rull og stamp. Lineariseringen gjøres omkring et likevektspunkt med null vinkel i rull og stamp, en konstant posisjon i hiv, og null hastighet i alle frihetsgradene unntatt i jag, der farten er konstant. Den lineariserte modellen kan kun kontrolleres i hiv, rull og stamp. Den lineariserte modellen uttrykkes som en niddimensjonal tilstandsrommodell, der generalisert aktuator dynamikk utgjør de tre første tilstandene, mens de resterende seks er posisjon og hastighet i hiv, rull og stamp.

Den lineariserte modellen utvides med førsteordens frekvensvektingsfunksjoner, med det formål å generere et sett av ytelses-signaler som har frekvensavhengig sensitivitet til tilstandsfeil (avvik fra referanseverdi i hiv, rull og stamp, eller deriverte av disse) og kontrollpådrag. Desto høyere verdien på ytelse-signalet er, desto mer ønsker vi at det lukkede systemet vi designer klarer å minimere den tilsvarende tilstandsfeilen eller kontrollpådraget. Tilstandsfeil ønskes minimert ved lave frekvenser, mens kontrollpådrag ønskes minimert ved høye frekvenser. I tillegg innføres frekvensvekting på de fysiske prosessforstyrrelsene som påvirker systemet. Dette med den hensikt å modellere at forstyrrelsene forventes å dominere i det frekvensområdet bølgeinduserte forstyrrelser opptrer. Denne frekvensvektingen transformerer signaler med "hvit støy" til signaler med "farget støy" i ønsket frekvensområde. Ellers antas hvit målestøy fra sensorer. Hvit støy fra prosessforstyrrelser og målestøy utgjør sammen med referanseverdier de eksterne input-signalene i det utvidede systemet.

Den \mathcal{H}_2 -optimaliserte kontrolleren minimerer 2-normen av transfermatrisen for det lukkede systemet fra eksterne input-signaler til ytelsesverdier. Den beregnes basert på den utvidede og frekvensvektede modellen ved bruk av funksjonen `h2syn()` i ”Robust Control Toolbox” i MATLAB. Fart og retning på fartøymodellen kontrolleres av separate PID-kontrollere, og sideveis hastighet kontrolleres til null av en PI-kontroller som oppdaterer referansen for vinkel i rull.

Simulink benyttes for å simulere systemet i følgende tre ulike sjøforhold: regulære langkammede bølger, irregulære langkammede bølger og irregulære kortkammede bølger. I hvert tilfelle simuleres rettlinjett bevegelse i både medsjø og motsjø. For irregulære kortkammede bølger simuleres også at fartøyet utfører en koordinert sving. Målestøy er kun lagt til i signalene som går til \mathcal{H}_2 -kontrolleren.

Resultatene viser at kontrollsyste­met i alle tilfellene klarer å kontrollere fartøyet stabilt i oppreist posisjon, samt redusere de bølgeinduserte bevegelsene. I noen av tilfellene mer effektivt enn andre. Kontrollsyste­met yter bedre i tilfellene med regulære bølger enn i tilfellene med irregulære bølger, og for irregulære bølger er ytelsen bedre for kortkammede enn for langkammede bølger. Ytelsen er også bedre for medsjø enn motsjø. Årsaken til dette er at bølger i motsjø genererer forstyrrelser med høyere frekvens enn bølger i medsjø, og frekvensvektingsfunksjonene gir lavere vekt­ing av tilstandsfeil ved høyere frekvenser. Resultatene viser også at det oppsto store akselerasjoner i stamp i tilfellet fartøyet beveget seg i motsjø med irregulære langkammede bølger.

Valget av frekvensvektingsfunksjoner er et kompromiss mellom bra reduksjon av bølgeinduserte bevegelser og minimering av målestøy som trenger gjennom kontrolleren og skaper høy-frekvente vibrasjoner i aktuatorene. Høyere ordens frekvensvektingsfunksjoner eller en mer nøyaktig linearisert modell kan redusere problemet.

Table of Contents

Preface	i
Abstract	iii
Sammendrag	v
Table of Contents	viii
List of Tables	ix
List of Figures	xiii
1 Introduction	1
1.1 Background:	1
1.2 Objective:	3
1.3 Scope of Work	4
1.4 Literature Review	5
1.4.1 Rejection of Wave Disturbances on a Hydrofoil Craft	5
1.4.2 \mathcal{H}_2 Control	7
1.4.3 Frequency Weighted Controller Design	11
2 Simulation Model	15
2.1 Dynamics	17
2.1.1 Kinematics:	17
2.1.2 Kinetics:	20
2.2 Lifting Foils	21
2.3 Rudders	26
2.4 Allocation of foil angles	29
2.5 Wave Model	31
2.5.1 Linear Wave Model	31
2.5.2 Wave Spectrum	34

2.5.3	Velocity of Water Particles in a Specific Location in the NED frame	37
2.6	Sensors and Measurement Noise	38
3	Linearized Model	41
3.1	Rigid Body Dynamics	41
3.1.1	Linearized Kinematics	43
3.1.2	Linearized Kinetics	43
3.1.3	Linearized Foil Forces due to Motions of the Craft	45
3.1.4	Linearized Control Force	51
3.2	State-Space Model	52
4	Controller Design and Maneuvering	55
4.1	Frequency Weighting	55
4.1.1	Weighted Output	56
4.1.2	Weighted Control	58
4.1.3	Weighted Plant Disturbance	60
4.2	Augmented Plant and Weight Dynamics	63
4.3	\mathcal{H}_2 Controller	64
4.4	External Controllers	66
4.4.1	Yaw-rate Controller	66
4.4.2	Sideslip Controller	66
4.4.3	Surge Speed Controller	68
4.5	Maneuvering	69
5	Results	71
5.1	Driving Straight Forward	72
5.1.1	Regular Long-Crested Waves	72
5.1.2	Irregular Long-Crested Waves	75
5.1.3	Irregular Short-Crested Waves	80
5.2	Turning In a Circle when Irregular Short-Crested Waves	88
6	Discussion	93
7	Conclusions and Further Work	97
7.1	Conclusions	97
7.2	Further Work	98
	Bibliography	99
	Appendix	101

List of Tables

2.1	Dimensions of the model	17
2.2	Constants	18
2.3	Controlled deviations in foil and rudder angles	30

List of Figures

1.1	Illustration of the Flying Foil hydrofoil craft	2
1.2	Variation of foil's lift by wave orbital motion (Kim and Yamato, 2004) . .	6
1.3	Closed-loop system containing a plant $P(s)$ and a feedback compensator $K(s)$. w includes external inputs, and z is the error (performance) signal .	8
1.4	Block diagram of the \mathcal{H}_2 controller	11
1.5	Block diagram of a frequency weighted plant	12
2.1	Shape of the vessel used for simulation: Projections into the yz- and xz-plane, respectively	16
2.2	NED versus body-fixed coordinate system	18
2.3	Forces acting on a lifting foil	22
2.4	Configuration of lifting foils	24
2.5	Configuration of rudders, seen from above	27
2.6	Profile of a rudder, seen from above	28
2.7	Regular Wave	33
2.8	PM Frequency spectrum for wind speed $U_{19.4} = 10$ m/s. Y-axis shows absolute values for $S(\omega)$	35
2.9	Frequency spectrum divided into rectangular components	37
2.10	Block diagram from Simulink showing the noise signal being added to the measurement signals before entering the \mathcal{H}_2 controller. The m-subscript denotes measured state with noise	39
3.1	Change in inflow velocity due to change in the foil velocity	46
4.1	Block diagram of the frequency weighted plant	56
4.2	Weighting function for the output error	57
4.3	Weighting function for the control input	59
4.4	Weighting function for the disturbance input	61
4.5	Singular values of closed-loop transfer functions from disturbance inputs in \mathbf{v} to position and velocity states in heave, roll and pitch	65
4.6	Singular values of $\phi/\phi_d(s)$	67

4.7	Outer feedback loop controlling sway velocity	68
5.1	Evolution of Heave, Roll and Pitch, when sailing in following sea with regular, long-crested waves	73
5.2	Evolution of Heave Speed, Roll Rate and Pitch Rate, when sailing in following sea with regular, long-crested waves	73
5.3	Evolution of Heave Acceleration, Roll Acceleration and Pitch Acceleration, when sailing in following sea with regular, long-crested waves	74
5.4	Evolution of deviations in foil angles giving forces/moments in Roll, Pitch and Heave, when sailing in following sea with regular, long-crested waves	74
5.5	Evolution of Heave, Roll and Pitch, when sailing in head sea with regular, long-crested waves	75
5.6	Evolution of Heave Speed, Roll Rate and Pitch Rate, when sailing in head sea with regular, long-crested waves	76
5.7	Evolution of Heave Acceleration, Roll Acceleration and Pitch Acceleration, when sailing in head sea with regular long-crested waves	76
5.8	Evolution of deviations in foil angles giving forces/moments in Roll, Pitch and Heave, when sailing in head sea with regular, long-crested waves	77
5.9	Evolution of Heave, Roll and Pitch, when sailing in following sea with irregular, long-crested waves	78
5.10	Evolution of Heave Speed, Roll Rate and Pitch Rate, when sailing in following sea with irregular, long-crested waves	79
5.11	Evolution of Heave Acceleration, Roll Acceleration and Pitch Acceleration, when sailing in following sea with irregular, long-crested waves	79
5.12	Evolution of deviations in foil angles giving forces/moments in Roll, Pitch and Heave, when sailing in following sea with irregular, long-crested waves	80
5.13	Evolution of Heave, Roll and Pitch, when sailing in head sea with irregular, long-crested waves	81
5.14	Evolution of Heave Speed, Roll Rate and Pitch Rate, when sailing in head sea with irregular, long-crested waves	81
5.15	Evolution of Heave Acceleration, Roll Acceleration and Pitch Acceleration, when sailing in head sea with irregular, long-crested waves	82
5.16	Evolution of deviations in foil angles giving forces/moments in Roll, Pitch and Heave, when sailing in head sea with irregular, long-crested waves	82
5.17	Evolution of Heave, Roll and Pitch, when sailing in following sea with irregular, short-crested waves	83
5.18	Evolution of Heave Speed, Roll Rate and Pitch Rate, when sailing in following sea with irregular, short-crested waves	84
5.19	Evolution of Heave Acceleration, Roll Acceleration and Pitch Acceleration, when sailing in following sea with irregular, short-crested waves	84
5.20	Evolution of deviations in foil angles giving forces/moments in Roll, Pitch and Heave, when sailing in following sea with irregular, short-crested waves	85
5.21	Evolution of Heave, Roll and Pitch, when sailing in head sea with irregular, short-crested waves	86
5.22	Evolution of Heave Speed, Roll Rate and Pitch Rate, when sailing in head sea with irregular, short-crested waves	86

5.23	Evolution of Heave Acceleration, Roll Acceleration and Pitch Acceleration, when sailing in head sea with irregular, short-crested waves	87
5.24	Evolution of deviations in foil angles giving forces/moments in Roll, Pitch and Heave, when sailing in head sea with irregular, short-crested waves	87
5.25	Path in the horizontal plane when driving in a circle with radius 100 m. Irregular, short-crested waves with mean direction North. Compared to results from controller designed for no sensor noise	89
5.26	Evolution of Heave, Roll and Pitch, when sailing in a circle path, in sea with irregular, short-crested waves	90
5.27	Evolution of Heave Speed, Roll Rate and Pitch Rate, when sailing in a circle path, in sea with irregular, short-crested waves	90
5.28	Evolution of Heading, Sway Speed and Yaw Rate, when sailing in a circle path, in sea with irregular, short-crested waves	91
5.29	Evolution of Heave Acceleration, Roll Acceleration and Pitch Acceleration, when sailing in a circle path, in sea with irregular, short-crested waves	91
5.30	Evolution of deviations in foil angles giving forces/moments in Roll, Pitch and Heave, when sailing in a circle path, in sea with irregular, short-crested waves	92

Abbreviations

CARE Control Algebraic Ricatti Equation.

CG Center of Gravity.

CO Body-Frame Origin.

DOF Degrees of Freedom.

EOM Equations of Motion.

FARE Filter Algebraic Ricatti Equation.

ITTC International Towing Tank Conference.

LQG Linear Quadratic Gaussian.

LQR Linear Quadratic Regulator.

LTI Linear Time Invariant.

MIMO Multiple-input multiple-output.

NED North-East-Down.

PI Proportional-Integral.

PID Proportional-Integral-Derivative.

RCS Ride Control System.

RMS Root Mean Square.

TTO *NTNU Technology Transfer AS*.

Introduction

1.1 Background:

NTNU Technology Transfer AS (TTO) is currently developing a new concept of a hydrofoil craft, currently called *Flying Foil*, where the idea is to use oscillating motions of the foils to obtain a thrust force at the same time as the foils are used to carry the weight of the craft. The goal is to achieve a significant higher propulsion efficiency compared to conventional hydrofoil crafts, leading to reduced fuel costs and emission of greenhouse gasses. TTO also expects the energy consumption to be further reduced by building the craft in new lightweight materials. The currently most potential market is for high-speed passenger boats operating along the Norwegian Coast. Here the political goal is to electrify both public car ferries and passenger boats in order to reduce the CO₂ emissions. The reduced energy demand of *Flying Foil* opens for using electrical propulsion systems powered by chargeable on-board batteries. By using modern lithium batteries with a much higher energy/weight ratio compared to old lead batteries, in combination with new technology for fast charging, *Flying Foil* has a good chance to be competitive in the tender process for high-speed passenger boats going in shuttle traffic with short stay in the dock.

In the concept of *Flying Foil*, two vertically arranged foils are oscillating with opposite phase in vertical direction, while the angle of each foil continuously is changing such that the sum of horizontal forces acting on the foils is giving thrust, while the sum of vertical forces is giving a constant lift force carrying the craft. It is not decided whether this concept shall be implemented both in the front and the aft of the craft, or just in one place. Figure 1.1 illustrates a concept where the concept is implemented both in the front and the aft. Anyway, it will be necessary to have lifting foils in at least two longitudinal positions of the craft in order to maintain balance in pitch. The load distribution between the front and the aft foils is not decided yet. Many configurations are possible, and one currently



Figure 1.1: Illustration of the Flying Foil hydrofoil craft

being studied has a large foil lifting the craft close behind the center of gravity, and two T-foils in the aft which are pulling the craft down as well as controlling the pitch. Independent of which configuration being selected, the foils used in the concept will be completely submerged, so a stabilizing control system is essential. Further will environmental disturbances, especially from waves and wind, cause oscillating motions giving bad passenger comfort and in the worst case make the craft unstable, so the control system also has to minimize these motions. In order to perform such control on this craft, the idea is to adjust the angles of the foils themselves or equip the foils with controlling flaps.

In the end, the craft shall be equipped with a control system keeping it stable in cruise conditions, and at the same time compensate environmental disturbances from waves, current and wind, such that the comfort of passengers and crew is satisfied. It also has to be equipped with an observer providing necessary state estimates based on available sensor measurements and a mathematical model of the dynamics of the craft. A longitudinal guidance system handling the take-off (craft rising up on the foils) and landing (hulls going back into the water) procedures has to be developed as well. Depending on potential customers' preferences, there may also be necessary to implement an autopilot and a more sophisticated guidance system.

In the first phase in developing this control and guidance system, Piene (2017) made a simplified simulation model of the craft and applied several Proportional-Integral-Derivative (PID) controllers to control heave, roll, pitch and yaw in independent closed loops. Successive loop closure where used to control the speed in sway to zero by updating the reference for the closed loop in roll, and the speed in surge was constantly fixed to 17 m/s as a part of the simulation model. The controllers where tuned according to methods provided by Beard and McLain (2011). Simulations where performed assuming calm water, but a constant wind load was applied and compared with similar simulations without the wind load. The simulation results showed good performance for no wind, both when sailing in straight line and when performing a turn. In the presence of wind the results where less

good, but still satisfactory.

The study presented in this report go one step ahead. There will be designed a more advanced Ride Control System (RCS) keeping the simulated craft stable in *heave*, *roll* and *pitch* as well as rejecting the wave disturbances in the same Degrees of Freedom (DOF) as good and optimal as possible. This is done in order to increase the passenger comfort when the craft is sailing in 17 m/s. The RCS will be based on a frequency weighted \mathcal{H}_2 -optimized Multiple-input multiple-output (MIMO) feedback controller, which also has the built-in observer property and can handle noise-contaminated sensor signals directly. Two independent PID controllers and one Proportional-Integral (PI) controller will also be applied in order to handle the DOF not covered by the RCS.

The RCS will be applied on the simplified simulation model made by Piene (2017). In this model, the propulsion concept with vertical oscillating foils is not modelled, so instead only single foils being translationally fixed to the craft will be considered. These will be four identical lifting foils, where the angle of each foil can be adjusted in order to maneuver the craft. The craft model will also be equipped with four rudders giving control in yaw. This simulation model is further extended with a wave model, implemented in order to simulate the impact the waves have on the foils due to the orbital motion of the water particles.

The performance of the RCS will be tested for different sea conditions with simulations in Simulink. This includes regular long-crested waves, irregular long-crested waves and irregular short-crested waves. The irregular waves will be generated according to a *Pierson Moskowitz* frequency spectrum for a wind speed of 10 m/s. However, since this study focus on rejecting the wave loads, there will be assumed zero wind load on the craft. The current in the water is also assumed to be zero. The main objective of the study will be emphasized in the following section.

1.2 Objective:

The main objective of this study is:

Designing a frequency weighted \mathcal{H}_2 -optimized feedback controller rejecting the wave disturbances in heave, roll and pitch for a high speed hydrofoil craft sailing in irregular sea, both for straight-line motion and when performing a coordinated turn.

The process of reaching this goal includes the following sub problems:

- Design of a 6 DOF nonlinear simulation model of a hydrofoil craft with a simplified shape and symmetric placement of four lifting foils and four vertical foils acting as rudders.
- Implementation of a wave model simulating the disturbances acting on each of the foils in different sea conditions.
- Linearization of the nonlinear simulation model about a trim condition equal the

expected cruise conditions for the craft. The linearized model has only the 3 DOF *heave, roll and pitch*.

- Using the linearized model in order to design the frequency weighted \mathcal{H}_2 -optimized feedback controller. This includes the design of transfer functions weighting the penalty on a defined performance error differently for different frequencies, as well as design of transfer functions representing the expected frequency distribution of disturbance forces and sensor noise.
- Design and implementation of additional, external feedback controllers supplementing the 3 DOF RCS in controlling the behaviour of the craft in all 6 DOF. This includes a simple PID controller which controls the yaw rate, and a simple PI controller updating the reference value for roll in order to minimize the speed in sway.
- Design of a simple guidance system making the craft performing a coordinated turn with a desired turning radius.

1.3 Scope of Work

The project will be done during the Fall 2017 and the first two months of 2018. The scope of work is as follows:

- Review of literature on hydrofoil control systems rejecting waves, \mathcal{H}_2 optimized control theory, and frequency weighted control. (August/September)
- Extend and improve the Simulink simulation model developed by Piene (2017). Include a wave model and implement wave forces on the foils. (September)
- Linearize the the simulation model with respect to *heave, roll and pitch*. (October)
- Augment the linearized model with frequency weighting and design the \mathcal{H}_2 -optimized controller. (October/November)
- Implement the controller in Simulink. Also include the external controllers. (November)
- Extensive simulations and tuning of controllers/weighting functions. (November/December)
- Report writing. (January/February)
- Deadline: February 25, 2018

The \mathcal{H}_2 -optimized controller designed in this study will be limited to only have guaranteed stability for a nominal plant equal the linearized model. No robustness design methods are implemented. All the controllers are designed for a constant surge speed of 17 m/s, and simulations are only performed for a limited number of wave conditions.

1.4 Literature Review

The literature review will be divided into three parts. The first part will consider historical research on rejection of wave disturbances on hydrofoil crafts in general, the second part will look into \mathcal{H}_2 -optimal control theory, and the third part will look into frequency weighted control. The theory presented in the two last parts of this section will be essential for the methods used in the design of the RCS in Chapter 4, and includes the basic theory behind the functions going to be used from the Robust Control Toolbox in MATLAB. The notations used in this section are introduced in order to present the theory, and does not necessarily refer to the same as notations using the same letter or symbol in later sections. Neither will vectors and matrices in this section be denoted by bold letters or symbols.

1.4.1 Rejection of Wave Disturbances on a Hydrofoil Craft

Motion control of fully submerged hydrofoil crafts has been studied for several decades. The present study will mainly call attention to more recent studies from the 90's and later, since a lot of results from computational and experimental studies using modern control theory were developed during this period. The studies highlighted in the rest of this subsection are looking into control in irregular waves and the significance of modelling the wave disturbance when designing the control system.

Lee and Rhee (2002) studied the design of a robust RCS enhancing the seakeeping performance in heave and pitch for a foil catamaran in head sea with irregular waves. They designed a controller which was stable and enhanced the performance with respect to disturbances from all regular wave components, and made the assumption that this controller also will be stable and enhance the performance with respect to disturbances from irregular waves composed of regular wave components, i.e. validity of the superposition principle. A constant feedback controller was designed using the Linear Quadratic Regulator (LQR) methodology, and it was used in combination with a low-pass filter reducing the sensor noise. They found that the assumption of superposition was valid, and the designed controller gave good performance, as well as robustness both in regular and irregular head waves. The ship motions were drastically reduced compared to when the RCS not was activated. However, the sensor noise included in the model had a significant and undesired impact on the control output, which got small but rapid vibrations.

Kim and Yamato (2004) did both theoretically and experimental studies on how to increase the seakeeping performance in heave and roll for a fully submerged hydrofoil craft sailing in following sea with regular waves. It was already well-known that a hydrofoil craft sailing in following seas usually has poor seakeeping performance, and the purpose of their study was to prove by experiment that this was due to the orbital motions of the waves. First they studied the variation of a foil's lift force and angle of attack in regular waves. In the case of head waves, there is an increase in the lift force when the foil is approaching the crest, and a decrease when leaving the crest. This helps the foil keeping a distance to the water surface, as well as contouring the waves. In the case of following waves,

the lift force is acting in the opposite directions. Figure 1.2 shows a good illustration of the problem. The figure is borrowed from Kim and Yamato (2004). From a linear,

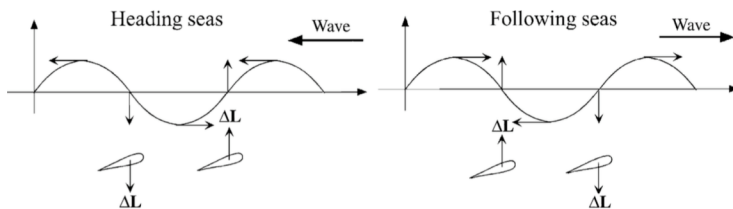


Figure 1.2: Variation of foil's lift by wave orbital motion (Kim and Yamato, 2004)

longitudinal state-space model of the model craft going to be used in the experiment, Kim and Yamato designed a linear feedback control system consisting of an LQR controller and a Kalman Filter for estimating the states. The wave-induced disturbances were only modelled as an ordinary disturbance input which was not limited to any frequency range. The experimental part of the study was a towing tank test of a model craft where the control system was implemented. The results from the experiments showed that the performance was not good in following waves, even when using large flap angles. The feedback control system did not manage to reduce the effect of the foil's lift variation due to orbital motions in the waves. However, in calm water the feedback control of motions was very effective. From these observations, they concluded that when designing a control system in order to improve the seakeeping performance in following waves, it is necessary to do this based on a mathematical model where the wave orbital motions are taken into account.

Kim and Yamato (2005) went further in studying how frequency shaping of the disturbance signals could improve the performance. This time by using simulations. The state-space model used for design of controller and Kalman Filter in the experimental study was augmented with a state-space model representing the disturbance forces, which were limited to a specific and expected range. The augmented model was used in design of new controller and Kalman Filter. The Kalman Filter also included the wave elevation for the corresponding modelled disturbance forces. The simulation model had included a sensor measuring the distance to the water in the front of the craft, such that the wave elevation could be calculated, and the Kalman Filter's estimated wave elevation and disturbances could be corrected towards more true values. The results showed that the wave elevations and disturbances acting on the foils were predicted with low errors.

Hatzakis and Sclavounos (2006) studied the use of LQR control for stabilization and disturbance rejection of a fully submerged hydrofoil craft sailing in regular and irregular waves. The simulated craft was modelled using a seakeeping model, with perturbations in heave and pitch. Added mass and damping forces were implemented in the model, and hydrostatic restoring forces were included for some of the simulations. Fluid memory effects were also accounted for. All states were assumed perfectly measured without any noise. The LQR controller was designed from a simplified linearized model where fluid memory effects were neglected, and the disturbance input did not have any frequency limitations. Simulation of both the craft with and without the hydrostatic restoring forces

in heave and pitch were performed. The latter is of interest in the present study. Results from initial simulations showed problems with steady-state errors in both heave and pitch. The solution to the problem was to augment the state-space model with integral states for heave and pitch, in order to include an integral feedback gain. Simulations using the controller designed from the augmented model showed good performance in both regular and irregular waves, and the craft remained stable during all of the simulations.

Bai and Kim (2010) studied motion control of a fast ship equipped with fully submerged hydrofoils in following waves. This craft was modelled in the two DOF heave and pitch, with the linear state-space model introduced by Kim and Yamato (2004). Bai and Kim (2010) applied the three different control algorithms PID, LQR and sliding mode control to the state-space model, and by simulations they compared the performance and robustness of the different controllers both in regular and irregular following waves. In the case of PID control, the flaps on the front and aft foil were controlled with a phase shift in order to compensate for different local velocity of the water. The performance was overall good for regular waves, but for irregular waves the sensitivity to wave height was strong, and for large waves instability occurred. They concluded that this was because of the derivative controller being sensitive to rapid change of the disturbance. The LQR controller showed very good performance in both regular and irregular waves. The heave and pitch motions were effectively reduced with small flap angles, and the system was stable for all the simulated cases. The sliding mode controller did also give good performance of motion response in irregular waves, but it had to use much larger control inputs compared to the other controllers. Jagging of the control signal did also cause the Root Mean Square (RMS) value of the acceleration to be large. In addition, they simulated the experiment from Kim and Yamato (2004) with the same LQR controller and a simulation model with the same properties as the one used in the towing tank experiment. The results showed that the simulated control session gave significantly better performance than the experimental one.

1.4.2 \mathcal{H}_2 Control

The \mathcal{H}_2 control problem will be presented according to description provided by Doyle et al. (1989) and Athans (2004).

Definition of the \mathcal{H}_2 norm:

First, the definition of the \mathcal{H}_2 norm has to be presented. Consider a stable Linear Time Invariant (LTI) system, described in the time domain by the following state-space model:

$$\begin{aligned}\dot{x}(t) &= \mathcal{A}x(t) + \mathcal{B}w(t) \\ y(t) &= \mathcal{C}x(t)\end{aligned}\tag{1.1}$$

Let the stable transfer matrix $G(s) = \mathcal{C}(sI - \mathcal{A})^{-1}\mathcal{B}$ describe the same LTI system in the frequency domain. The \mathcal{H}_2 norm of $G(s)$ is defined as:

$$\|G(s)\|_2 = \left(\frac{1}{2\pi} \int_{-\infty}^{\infty} \text{tr} \left[G(j\omega) G^\top(-j\omega) \right] d\omega \right)^{1/2} \quad (1.2)$$

The \mathcal{H}_2 norm can also be computed from the state-space model in (1.1). Assume $w(t)$ is continuous-time, zero-mean, white noise with unit intensity. Let L_c denote the *controllability Gramian* of $(\mathcal{A}, \mathcal{B})$, then

$$\|G(s)\|_2^2 = \text{tr} \left[\mathcal{C} L_c \mathcal{C}^\top \right]. \quad (1.3)$$

L_c can be found by solving the Lyapunov equation,

$$\mathcal{A} L_c + L_c \mathcal{A}^\top + \mathcal{B} \mathcal{B}^\top = 0. \quad (1.4)$$

Alternatively, let L_o denote the *observability Gramian* of $(\mathcal{C}, \mathcal{A})$, then

$$\|G(s)\|_2^2 = \text{tr} \left[\mathcal{B}^\top L_o \mathcal{B} \right]. \quad (1.5)$$

L_o can be found by solving the Lyapunov equation,

$$\mathcal{A}^\top L_o + L_o \mathcal{A} + \mathcal{C}^\top \mathcal{C} = 0. \quad (1.6)$$

Definition of the \mathcal{H}_2 -optimal controller:

Next step is to define the \mathcal{H}_2 -optimal controller. Consider the block diagram in Figure 1.3. The plant $P(s)$ is subject to control by a stabilizing feedback compensator $K(s)$. The signal w contains all external inputs, including disturbances, sensor noise and commands, z is an error signal (also referred to as the *performance signal*), y contains all measured states available for the controller, and u is the control input. Let $T_{wz}(s)$ denote the transfer

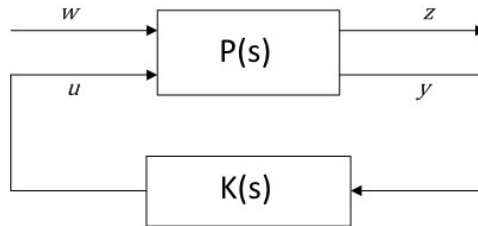


Figure 1.3: Closed-loop system containing a plant $P(s)$ and a feedback compensator $K(s)$. w includes external inputs, and z is the error (performance) signal

matrix of the stable closed-loop system, from the vector of external inputs, w , to the error vector z . The \mathcal{H}_2 -optimal controller is defined as the stabilizing feedback compensator $K(s) = K_2(s)$ minimizing $\|T_{wz}(s)\|_2$.

Procedure of calculating the \mathcal{H}_2 -optimal controller $K_2(s)$:

Assuming $P(s)$ is an LTI plant, which in the time domain has the state-space representation

$$\dot{x}(t) = Ax(t) + B_1w(t) + B_2u(t) \quad (1.7)$$

$$z(t) = C_1x(t) + D_{12}u(t) \quad (1.8)$$

$$y(t) = C_2x(t) + D_{21}w(t) + D_{22}u(t), \quad (1.9)$$

where (1.7) is the equation of the linear state dynamics, with x as the state vector, (1.8) is the *performance* equation, and (1.9) is the *measurement equation*.

The process of solving the \mathcal{H}_2 -optimal control problem can be divided into two main steps. The first step is the state feedback problem. Assume that all the states in x are available for the controller, and assume that (A, B_2) is stabilizable, i.e. all plant unstable modes are controllable from the control input $u(t)$, and that (C_1, A) is detectable, i.e. all plant unstable modes are observable in the the performance signal $z(t)$. Minimizing $\|T_{wz}(s)\|_2$, equals minimizing the covariance of $z(t)$:

$$\begin{aligned} \|T_{wz}(s)\|_2^2 &= \text{cov}[z(t), z(t)] = E\{z^\top(t)z(t)\} = \lim_{T \rightarrow \infty} \frac{1}{2T} \int_{-T}^T z^\top(t)z(t)dt \\ &= \lim_{T \rightarrow \infty} \frac{1}{2T} \int_{-T}^T [C_1x(t) + D_{12}u(t)]^\top [C_1x(t) + D_{12}u(t)] dt \\ &= \lim_{T \rightarrow \infty} \frac{1}{2T} \int_{-T}^T [x^\top(t)C_1^\top C_1x(t) + 2x^\top(t)C_1^\top D_{12}u(t) + u^\top(t)D_{12}^\top D_{12}u(t)] dt \end{aligned} \quad (1.10)$$

The feedback controller minimizing this equation is

$$u(t) = F_2x(t), \quad (1.11)$$

where F_2 is the static feedback gain given by

$$F_2 = -(D_{12}^\top D_{12})^{-1}(D_{12}^\top C_1 + B_2^\top X_2). \quad (1.12)$$

$X_2 = X_2^\top \geq 0$ is the unique solution of the Control Algebraic Ricatti Equation (CARE):

$$\begin{aligned} 0 &= X_2 A_r^\top + A_r^\top X_2 + C_1^\top C_1 - C_1^\top D_{12} (D_{12}^\top D_{12})^{-1} D_{12}^\top C_1 \\ &\quad - X_2 B_2 (D_{12}^\top D_{12})^{-1} B_2^\top X_2, \end{aligned} \quad (1.13)$$

where

$$A_r := A - B_2 (D_{12}^\top D_{12})^{-1} D_{12}^\top C_1. \quad (1.14)$$

In the case the cross-product penalties are zero, which equals $C_1^\top D_{12} = 0$, then $A_r = A$, and the CARE simplifies to

$$0 = X_2 A_r^\top + A_r^\top X_2 + C_1^\top C_1 - X_2 B_2 (D_{12}^\top D_{12})^{-1} B_2^\top X_2, \quad (1.15)$$

and the control gain becomes

$$F_2 = -(D_{12}^\top D_{12})^{-1} B_2^\top X_2. \quad (1.16)$$

This equals an LQR feedback gain $F_2 = -R^{-1} B_2^\top X_2$ minimizing the Quadratic Cost Function

$$J = E \left\{ \lim_{T \rightarrow \infty} \frac{1}{2T} \int_{-T}^T [x^\top(t) Q x(t) + u^\top(t) R u(t)] dt \right\}, \quad (1.17)$$

for $Q = C_1^\top C_1$ and $R = D_{12}^\top D_{12}$.

The next step is the estimation problem. If, for $x \in \mathbb{R}^n$ and $y \in \mathbb{R}^m$, $m \leq n$ and $D_{21}w(t) \neq 0$, or the measurements are contaminated with noise, the state vector $x(t)$ has to be estimated. Let \hat{x} denote the estimate of x . Assume (A, B_1) is stabilizable, i.e. all plant unstable modes are controllable from the process noise $w(t)$, and assume (C_2, A) is detectable, i.e. all plant unstable modes are observable in the the sensor output $y(t)$. Then,

$$\dot{\hat{x}} = A\hat{x} + B_2 u + L_2(C_2\hat{x} + D_{22}u - y), \quad (1.18)$$

where L_2 is the filter gain given by

$$L_2 = -(Y_2 C_2^\top + B_1 D_{21}^\top)(D_{21} D_{21}^\top)^{-1}. \quad (1.19)$$

$Y_2 = Y_2^\top \geq 0$ is the unique solution of the Filter Algebraic Ricatti Equation (FARE):

$$\begin{aligned} 0 = & Y_2 A_e^\top + A_e^\top Y_2 + B_1 B_1^\top - B_1 D_{21}^\top (D_{21} D_{21}^\top)^{-1} D_{21} B_1^\top \\ & - Y_2 C_2^\top (D_{21} D_{21}^\top)^{-1} C_2 Y_2, \end{aligned} \quad (1.20)$$

where

$$A_e = A - B_1 D_{21}^\top (D_{21} D_{21}^\top)^{-1} C_2. \quad (1.21)$$

In the case process and sensor noises are uncorrelated, which equals $B_1 D_{21}^\top = 0$, then $A_e = A$, and the FARE simplifies to

$$0 = Y_2 A^\top + A^\top Y_2 + B_1 B_1^\top - Y_2 C_2^\top (D_{21} D_{21}^\top)^{-1} C_2 Y_2, \quad (1.22)$$

and the filter gain becomes

$$L_2 = -Y_2 C_2^\top (D_{21} D_{21}^\top)^{-1}. \quad (1.23)$$

This equals the filter-gain matrix $L_2 = -Y_2 C_2^\top \Theta^{-1}$ of a steady-state, continuous-time Kalman filter minimizing the covariance of the estimation error, $E\{(x - \hat{x})(x - \hat{x})^\top\}$, when $\Theta = D_{21} D_{21}^\top$ is the covariance matrix of the measurement noise.

With the state estimator in (1.18), and the controller in (1.11), the \mathcal{H}_2 -optimal controller $K_2(s)$ can be presented as a state-space model

$$\begin{aligned} \dot{\hat{x}} &= (A + L_2 C_2 + B_2 F_2 + L_2 D_{22} F_2) \hat{x} - L_2 y \\ u &= F_2 \hat{x}, \end{aligned} \quad (1.24)$$

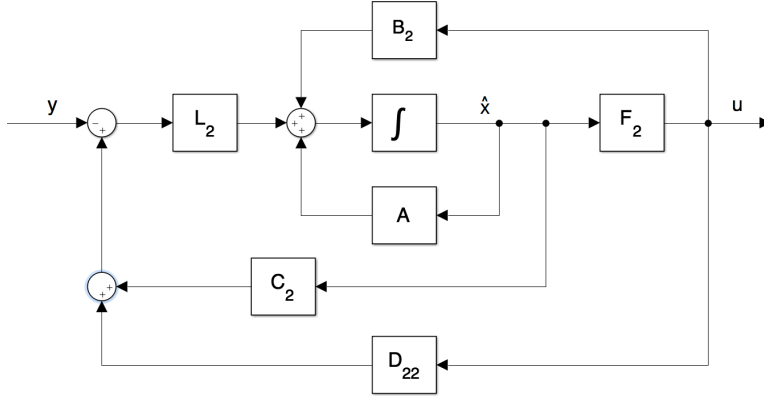


Figure 1.4: Block diagram of the \mathcal{H}_2 controller

where F_2 and B_2 are as defined in (1.12) and (1.19) respectively. Figure 1.4 illustrates the controller in a block diagram. As a combination of an LQR controller and a Kalman Filter, the \mathcal{H}_2 controller solves the Linear Quadratic Gaussian (LQG) control problem.

It is important to notice that this controller only guarantee nominal stability and performance, i.e. in the case the plant being controlled is identical to the linear plant $P(s)$. However, for real physical systems there will in almost every case be impossible to reconstruct an exact mathematical representation, so there will usually be unmodelled dynamics and/or linearization of the dynamics being modelled. Hence, there is no guarantee that an \mathcal{H}_2 controller being designed according to the procedure above gives stability or performance robustness when applied to the real plant $P(s)$ is supposed to represent (Athans, 2004).

1.4.3 Frequency Weighted Controller Design

Frequency weighting in the controller design will be presented according to description provided by Athans (2004).

For more sophisticated controllers, there might be preferable to penalize state errors and control inputs differently at different frequencies. E. g. penalize the state errors due to disturbances and/or change in the commands more at low frequencies, and penalize the control input more at high frequencies, where sensor noise and dynamic model errors are expected. Consider the state-space model in (1.7) to (1.9) for the plant $P(s)$. Define the frequency weighted performance signals $z_1(s) = W_y(s)z(s)$ for the output error, and $z_2(s) = W_u(s)u(s)$ for the control input. $W_y(s)$ and $W_u(s)$ are diagonal frequency-weighting matrices, designed according to the control engineer's preferences. By augmenting these weighting matrices to the plant model $P(s)$, it is possible to design a feed-

back controller $K(s)$ minimizing the performance signals $z_1(s)$ and $z_2(s)$ such that the desired frequency weighting is taken into account. By just penalizing the signals in $z(s)$ and $u(s)$ directly, as for the \mathcal{H}_2 controller presented in previous section, or for a static LQR controller with static cost matrices Q and R , it will not be possible to obtain this frequency weighting flexibility.

It also might be necessary to use frequency weights on the external inputs to the system. The \mathcal{H}_2 (LQG) controller presented in Section 1.4.2 assumes the elements of the external-input vector $w(s)$ being continuous-time, zero-mean, white noise with unit intensity. However, this is not necessarily the case for the plant subject to control. Process disturbances and commands are typically limited to specific frequency regions, and the sensor noises might also be limited to high frequencies. Consider a plant being exposed to process disturbances $d(s)$ dominating in a specific frequency region, and where the sensor noise $v(s)$ is strong for high frequencies, or it is desired to make the close-loop system insensitive to the high-frequency sensor noise. This problem can be solved by augmenting the weighting matrices $W_d(s)$ and $W_v(s)$ to the plant model, such that the process disturbances $d(s)$ and sensor noise $v(s)$ can be modelled as functions of the zero-mean, unit-intensity, white-noise vectors $w_1(s)$ and $w_2(s)$, respectively:

$$d(s) = W_d(s)w_1(s) \quad (1.25)$$

$$v(s) = W_v(s)w_2(s) \quad (1.26)$$

Figure 1.5 shows a block diagram of a frequency weighted plant model, where the objective is to control the measured states, y_p to zero. It includes the performance weighting matrices $W_y(s)$ and $W_u(s)$, and the disturbance weighting matrices $W_d(s)$ and $W_v(s)$. The disturbance inputs w_1 and w_2 are continuous-time, zero-mean, white noise with unit intensity. The matrices B and L in the figure corresponds to B_2 and B_1 in (1.7), respectively. In this block diagram, C_1 in the performance equation (1.8), and C_2 in the measurement equation (1.9) are identical and denoted by C . The frequency weighted \mathcal{H}_2 -optimal con-

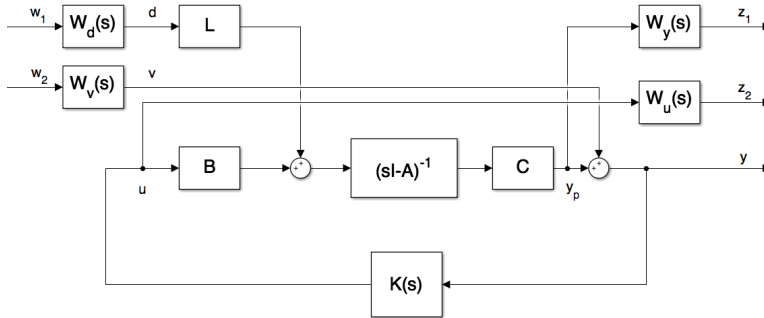


Figure 1.5: Block diagram of a frequency weighted plant

troller for this augmented plant will be the dynamic feedback compensator $K(s) = K_2(s)$

minimizing $\|T_{wz}(s)\|_2$, for $T_{wz}(s)$ being the transfer matrix of the closed-loop system from the external input vector $[w_1, w_2]^\top$ to the performance output vector $[z_1, z_2]^\top$.

The augmentation of the plant model and frequency weights can be implemented in the time domain by realizing all the weighting matrices into state-space models and augment these to the state-space model of the plant. The order of this augmented system will equal the plant order plus the sum of the order of each weighting matrix. The feedback compensator $K(s)$ will typically be of the same order. Even in the case all the states in the plant were perfectly measured and the estimation problem vanished, the feedback compensator $K(s)$ has to be dynamic in order to handle the frequency-weighting dynamics.

Simulation Model

The model used for the simulations in this study has a simplified geometry, build up of rectangular cuboid blocks. The craft has a catamaran shape, with two side blocks representing the two hulls and one middle block connecting these. The body-fixed coordinate system is as shown in Figure 2.1. The origin is located in the center of the area spanned by the length and width of the craft, at a height level equal to the bottom of the hulls.

The craft is equipped with four identical foils with a constant profile, arranged as one pair in the front and one pair in the aft. Each pair has the same distance to the origin, and is supporting the rest of the craft with two identical legs. Hence, the craft is completely symmetric about both the xz and the yz plane. All foils are completely submerged during normal operating conditions.

The dimensions of the craft model are given in Table 2.1. Definitions of the dimensions are provided in Figure 2.1. Length and width is set to approximately the same as for the passenger catamaran *Trondheimsfjord I*, whose values are available at the homepage of Brødrene AA (2017). The height is chosen to be $3/4$ of the width. Due to improvements in the technology of low-weight materials during the last years, the weight can be assumed to be significant less than the weight of *Trondheimsfjord I*. The location of the center of gravity (COG) and the moments of inertia are calculated assuming a homogeneous mass distribution.

Table 2.2 lists the constants used for gravity acceleration, water density, cruising speed and operating elevation, which is the distance between the water surface and the body-frame origin in cruising conditions. The cruising speed is approximately the same as for *Trondheimsfjord I*

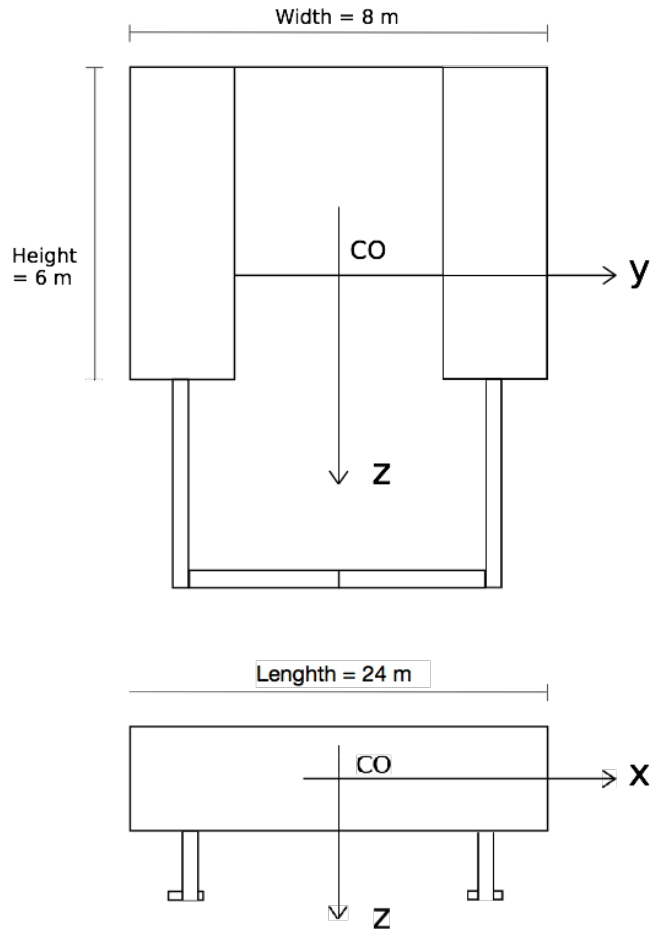


Figure 2.1: Shape of the vessel used for simulation: Projections into the yz- and xz-plane, respectively

Table 2.1: Dimensions of the model

Length	24.0 <i>m</i>
Width	8.0 <i>m</i>
Height	6.0 <i>m</i>
Mass	$60 \cdot 10^3$ <i>kg</i>
Center of gravity:	
x_g	0 <i>m</i>
y_g	0 <i>m</i>
z_g	−3.33 <i>m</i>
Moments of inertia:	
I_x	$1.036 \cdot 10^6$ <i>kg · m²</i>
I_y	$3.570 \cdot 10^6$ <i>kg · m²</i>
I_z	$3.270 \cdot 10^6$ <i>kg · m²</i>
I_{xy}, I_{xz}, I_{yz}	0 <i>kg · m²</i>
x position front foils	9.0 <i>m</i>
x position aft foils	−9.0 <i>m</i>
z position of all foils	4.0 <i>m</i>
Dimensions of each foil:	
Chord length (<i>c</i>)	1.0 <i>m</i>
Span (<i>b</i>)	2.8 <i>m</i>
Dimensions of each rudder:	
Chord length (<i>c^r</i>)	0.25 <i>m</i>
Span (<i>b^r</i>)	1.12 <i>m</i>

2.1 Dynamics

The goal of this section is to find the equations of motion describing the dynamics of the craft. According to Fossen (2011), the dynamics can be divided into two parts: *kinematics*, which describes the geometrical aspects of motion, and *kinetics*, which relates the motions of a body to the forces acting on it.

2.1.1 Kinematics:

For the hydrofoil craft, the kinematics relates the body-frame velocities of the craft to the *North-East-Down* (NED) coordinate system, $\{n\} = (x_n, y_n, z_n)$. The NED frame is a local Cartesian coordinate system with origin on a desired point of the Earth surface, and where the x-axis point toward North, the y-axis point toward East and the z-axis point downward normal to the Earth's surface (Fossen, 2011).

Table 2.2: Constants

Gravity acceleration:	g	9.81 m/s^2
Water density (salt water):	ρ	1025 kg/m^3
Cruising speed:	U_0	17 m/s
Operating elevation:	h_0	2.5 m

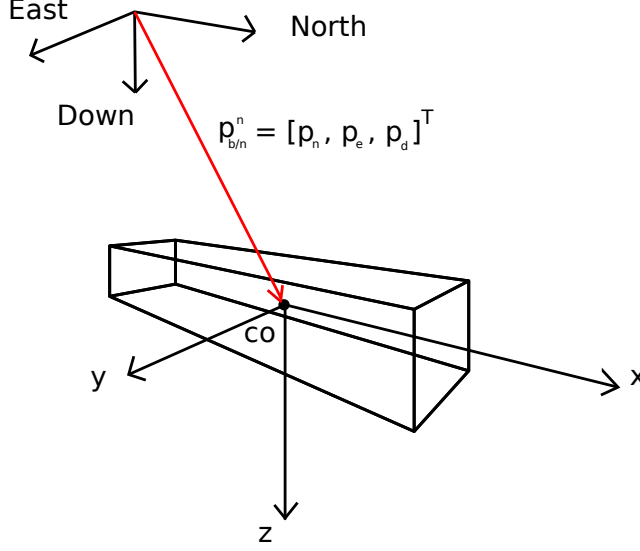


Figure 2.2: NED versus body-fixed coordinate system

Figure 2.2 shows the relation between the NED frame and the body frame for the hydrofoil craft. The position of the Body-Frame Origin (CO) is given by p_n , p_e and p_d denoting the *North*, *East* and *Down* coordinates, respectively. Following Fossen's convention, these coordinates can be combined into one vector:

$$\mathbf{p}_{b/n}^n := \begin{bmatrix} p_n \\ p_e \\ p_d \end{bmatrix} \in \mathbb{R}^3 \quad (2.1)$$

The orientation of the body frame relative to the NED frame will in this paper be described with the *Euler angles* ϕ , θ and ψ , which also will be denoted as *roll*, *pitch*, and *yaw*, respectively. The Euler angles are represented by the following vector:

$$\boldsymbol{\Theta}_{nb} := \begin{bmatrix} \phi \\ \theta \\ \psi \end{bmatrix} \in \mathbb{R}^3 \quad (2.2)$$

Combining $\mathbf{p}_{b/n}^n$ and Θ_{nb} into one vector representing all the 6 DOF:

$$\boldsymbol{\eta} := \begin{bmatrix} \mathbf{p}_{b/n}^n \\ \Theta_{nb} \end{bmatrix} \in \mathbb{R}^6 \quad (2.3)$$

The velocities of the craft are described in body frame. There are three linear velocities u , v and w along the body-frame x-, y- and z-axis, respectively. These three velocities are combined into the vector

$$\mathbf{v}_{b/n}^b := \begin{bmatrix} u \\ v \\ w \end{bmatrix} \in \mathbb{R}^3. \quad (2.4)$$

There are also three angular velocities p , q and r about the x , y and z -axis, respectively. These three velocities are combined into the vector

$$\boldsymbol{\omega}_{b/n}^b := \begin{bmatrix} p \\ q \\ r \end{bmatrix} \in \mathbb{R}^3. \quad (2.5)$$

Combining all velocities into one vector $\boldsymbol{\nu}$ for all the 6 DOF:

$$\boldsymbol{\nu} := \begin{bmatrix} \mathbf{v}_{b/n}^b \\ \boldsymbol{\omega}_{b/n}^b \end{bmatrix} = \begin{bmatrix} u \\ v \\ w \\ p \\ q \\ r \end{bmatrix} \in \mathbb{R}^6 \quad (2.6)$$

According to Fossen (2011) is the kinematic relation between the body frame and the NED frame given by

$$\dot{\boldsymbol{\eta}} = \mathbf{J}_{\Theta}(\boldsymbol{\eta})\boldsymbol{\nu}, \quad (2.7)$$

where \mathbf{J}_{Θ} is the transformation matrix, build up of the rotation matrix $\mathbf{R}_b^n(\Theta_{nb})$ and the angular transformation matrix $\mathbf{T}_{\Theta}(\Theta_{nb})$, such that

$$\begin{bmatrix} \dot{\mathbf{p}}_{b/n}^n \\ \dot{\Theta}_{nb} \end{bmatrix} = \begin{bmatrix} \mathbf{R}_b^n(\Theta_{nb}) & \mathbf{0}_{3 \times 3} \\ \mathbf{0}_{3 \times 3} & \mathbf{T}_{\Theta}(\Theta_{nb}) \end{bmatrix} \begin{bmatrix} \mathbf{v}_{b/n}^b \\ \boldsymbol{\omega}_{b/n}^b \end{bmatrix}. \quad (2.8)$$

Fossen (2011) provides the following definitions of $\mathbf{R}_b^n(\Theta_{nb})$ and $\mathbf{T}_{\Theta}(\Theta_{nb})$:

$$\mathbf{R}_b^n(\Theta_{nb}) = \begin{bmatrix} c\psi c\theta & -s\psi c\theta + c\psi s\theta s\phi & s\psi s\theta + c\psi c\theta s\phi \\ s\psi c\theta & c\psi c\theta + s\psi s\theta s\phi & -c\psi s\theta + s\psi c\theta s\phi \\ -s\theta & c\theta s\phi & c\theta c\phi \end{bmatrix} \quad (2.9)$$

$$\mathbf{T}_{\Theta}(\Theta_{nb}) = \begin{bmatrix} 1 & s\phi t\theta & c\phi t\theta \\ 0 & c\phi & -s\phi \\ 0 & s\phi/c\theta & c\phi/c\theta \end{bmatrix} \quad (2.10)$$

Here, using the abbreviations $s \cdot = \sin(\cdot)$, $c \cdot = \cos(\cdot)$ and $t \cdot = \tan(\cdot)$. The definitions of $\mathbf{R}_b^n(\Theta_{nb})$ and $\mathbf{T}_{\Theta}(\Theta_{nb})$, shows that \mathbf{J}_{Θ} depends on the Euler angles. Hence, the kinematic equation for the system is nonlinear.

2.1.2 Kinetics:

According to Fossen (2011), the rigid body kinetics of the craft can be expressed in the vectorial setting

$$\mathbf{M}_{RB}\dot{\boldsymbol{\nu}} + \mathbf{C}_{RB}(\boldsymbol{\nu})\boldsymbol{\nu} = \boldsymbol{\tau}_{RB}, \quad (2.11)$$

where \mathbf{M}_{RB} is the rigid-body mass matrix, $\mathbf{C}_{RB}(\boldsymbol{\nu})$ is the rigid-body Coriolis and centripetal matrix, due to the rotation of the body frame about the inertial frame, and $\boldsymbol{\tau}_{RB}$ is a vector of external forces and moments acting on the body, expressed in body frame.

The rigid-body mass matrix is according to Fossen (2011) defined by

$$\mathbf{M}_{RB} = \begin{bmatrix} m\mathbf{I}_{3 \times 3} & -m\mathbf{S}(\mathbf{r}_g^b) \\ m\mathbf{S}(\mathbf{r}_g^b) & \mathbf{I}_b \end{bmatrix}, \quad (2.12)$$

where m is the body mass, $\mathbf{I}_b \in \mathbb{R}^{3 \times 3}$ is the inertia matrix about CO, $\mathbf{r}_g^b = [x_g, y_g, z_g]^\top$ is the distance vector from CO to CG, and $\mathbf{S}(\mathbf{r}_g^b)$ is a skew-symmetric matrix defined by

$$\mathbf{S}(\boldsymbol{\lambda}) = \begin{bmatrix} 0 & -\lambda_3 & \lambda_2 \\ \lambda_3 & 0 & -\lambda_1 \\ -\lambda_2 & \lambda_1 & 0 \end{bmatrix}, \quad \boldsymbol{\lambda} = \begin{bmatrix} \lambda_1 \\ \lambda_2 \\ \lambda_3 \end{bmatrix}. \quad (2.13)$$

There exists several representations of the Coriolis and centripetal matrix $\mathbf{C}_{RB}(\boldsymbol{\nu})$, which all gives the same vector $\mathbf{C}_{RB}(\boldsymbol{\nu})\boldsymbol{\nu}$ (Fossen, 2011). We are here using the representation that is independent of the linear velocities,

$$\mathbf{C}_{RB}(\boldsymbol{\nu}) = \begin{bmatrix} m\mathbf{S}(\boldsymbol{\nu}_2) & -m\mathbf{S}(\boldsymbol{\nu}_2)\mathbf{S}(\mathbf{r}_g^b) \\ m\mathbf{S}(\mathbf{r}_g^b)\mathbf{S}(\boldsymbol{\nu}_2) & -\mathbf{S}(\mathbf{I}_b\boldsymbol{\nu}_2) \end{bmatrix}, \quad (2.14)$$

where $\boldsymbol{\nu}_2 = \boldsymbol{\omega}_{b/n}^n = [p, q, r]^\top$.

The external forces are given by the sum

$$\boldsymbol{\tau}_{RB} = -\mathbf{g}(\boldsymbol{\eta}) + \boldsymbol{\tau}_w + \boldsymbol{\tau}_c, \quad (2.15)$$

where $-\mathbf{g}(\boldsymbol{\eta})$ is the body-frame force vector only due to gravity, $\boldsymbol{\tau}_c$ contains the actuator forces, and $\boldsymbol{\tau}_w$ contains the reminding forces due to environmental disturbances. The buoyancy, as well as the added mass, from foils and other submerged equipment is neglected.

The gravity force vector $\mathbf{g}(\boldsymbol{\eta})$, derived from the definition in Fossen (2011) by setting buoyancy equal to zero, is

$$\mathbf{g}(\boldsymbol{\eta}) = - \begin{bmatrix} \mathbf{R}_b^n(\boldsymbol{\Theta}_{nb})^{-1}\mathbf{f}_g^n \\ \mathbf{r}_g^b\mathbf{R}_b^n(\boldsymbol{\Theta}_{nb})^{-1}\mathbf{f}_g^n \end{bmatrix}, \quad (2.16)$$

where

$$\mathbf{f}_g^n = \begin{bmatrix} 0 \\ 0 \\ m \cdot g \end{bmatrix} \quad (2.17)$$

is the gravity force vector expressed in NED frame, and

$$\mathbf{r}_g^b = [x_g, y_g, z_g]^\top \quad (2.18)$$

is the vector from CO to Center of Gravity (CG).

For a hydrofoil craft in cruising speed, the resistance from the water is small compared to a displacement vessel, and it is mainly due to the pressure and viscous drag on the lifting foils, which will be treated as a part of the actuator forces described in Section 2.2. Resistance from foil legs, both in surge and sway, is neglected. However, the air resistance and lateral wind disturbances have a significant impact on the craft's behaviour, due to relatively high cruising speed and a large side area, respectively. Hence, we have made it possible to include these forces as an external force vector $\boldsymbol{\tau}_w = \boldsymbol{\tau}_{wind}$ in the body frame. However, as mentioned in the introduction, we will in this study neglect such forces, and will for now set $\boldsymbol{\tau}_w = \mathbf{0}$. The wave-induced disturbance forces are due to change in inflow angle and speed relative to the lifting foils and rudders, and will therefor be considered as a part of the actuator forces $\boldsymbol{\tau}_c$.

Finally, the total dynamics of the simulation model can be written:

$$\dot{\boldsymbol{\eta}} = \mathbf{J}_\Theta(\boldsymbol{\eta})\boldsymbol{\nu} \quad (2.19)$$

$$\mathbf{M}_{RB}\dot{\boldsymbol{\nu}} + \mathbf{C}_{RB}(\boldsymbol{\nu})\boldsymbol{\nu} + \mathbf{g}(\boldsymbol{\eta}) = \boldsymbol{\tau}_c \quad (2.20)$$

2.2 Lifting Foils

Figure 2.3 shows the profile of a lifting foil. x_f and z_f denotes the x and z-axis of the local foil coordinate frame $\{f\} = (x_f, y_f, z_f)$, and are parallel to the body-frame x- and z-axis, respectively. The y-axis, y_f , is not drawn in Figure 2.3, but according to the right-hand rule it is supposed to go inward and is parallel to the body-frame y-axis. V_∞ is the speed of the inflow due to the relative motion between the foil and the water. α_∞ is the angle between the inflow direction and the x-axis of the foil, and α is the geometrical angle between the chord line of the foil and the x_f axis. The hinge axis of each foil is aligned with its y_f axis, and positive direction of the geometric angle α is determined by the right-hand rule for rotation about the y_f axis. The net force vector acting on the foil, due to pressure distribution and viscosity, is divided into a lifting component F_L^f , which is perpendicular to the inflow direction, and one drag component F_D^f in the same direction as the inflow. Side-way drag forces, i.e. in the y direction of the foil, as well as the vessel's body frame, are in this study neglected. The foil can be rotated about its origin, which is assumed located such that the moment acting on the foil due to the pressure distribution becomes small compared to the inertia of the craft and can be neglected.

The angle α_i is called *ideal angle of attack*. At this angle all of the lift force is due to the curvature of the foil, and it is usually giving the lowest risk of cavitation (Steen, 2011). We assume the lifting foils are designed such that, when the craft is in a trim condition with

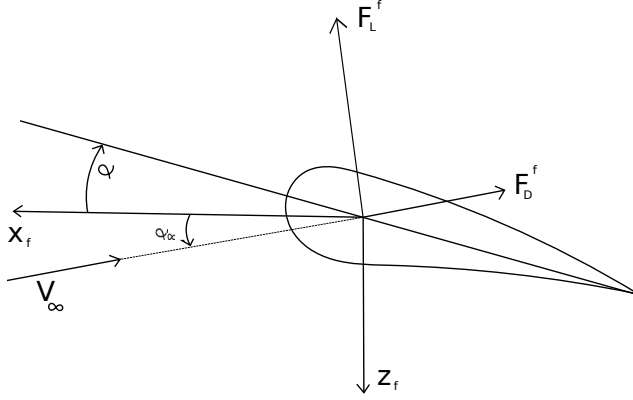


Figure 2.3: Forces acting on a lifting foil

a surge speed equal to the cruising speed U_0 , and all other velocity components and Euler angles equal to zero, then $\alpha = \alpha_i$ for all foils gives a total lift force equal to the weight of the craft. Since the simulation will be done around the cruising speed, $\alpha^* = \alpha_i|_{\alpha_\infty=0}$ is set to be the default angle of the foils. Deviation from α^* is denoted by δ , which will be the input from the controller. The total geometrical angle relative to the body-frame x-axis becomes

$$\alpha = \alpha^* + \delta. \quad (2.21)$$

The relative angle between the chord line and the inflow direction is denoted by α_r :

$$\alpha_r = \alpha + \alpha_\infty = \alpha^* + \delta + \alpha_\infty \quad (2.22)$$

The inflow speed V_∞ and direction α_∞ depends on the local velocity of the foil, relative to the water. This relative velocity will here be denoted by

$$\mathbf{v}_{rel}^f := \begin{bmatrix} u_{rel}^f \\ v_{rel}^f \\ w_{rel}^f \end{bmatrix}, \quad (2.23)$$

where u_{rel}^f , v_{rel}^f and w_{rel}^f are the relative velocity components along the x_f , y_f and z_f axes, respectively. Projection into the foil's xz plane gives:

$$V_\infty = \sqrt{(u_{rel}^f)^2 + (w_{rel}^f)^2} \quad (2.24)$$

$$\alpha_\infty = \tan^{-1} \left(\frac{w_{rel}^f}{u_{rel}^f} \right) \quad (2.25)$$

The relative-velocity vector \mathbf{v}_{rel}^f is defined as the difference between the local velocity of the foil relative to the NED frame, $\mathbf{v}_{f/n}^f$, and the local velocity of the water particles

relative to the NED frame, $\mathbf{v}_{w/n}^f$, both expressed in the foil's reference frame:

$$\mathbf{v}_{rel}^f := \mathbf{v}_{f/n}^f - \mathbf{v}_{w/n}^f \quad (2.26)$$

For each foil, $\mathbf{v}_{f/n}^f$ depends on the craft's velocity $\boldsymbol{\nu}$ and the position of the foil in the body frame. Hence, the different foils might experience different velocities due to rotational motions of the craft. Figure 2.4 shows the configuration of the four foils seen from above. The origin of each foil is located by a distance vector \mathbf{r}_f^b from CO. Due to motions of the craft, the local velocity $\mathbf{v}_{f/n}^f$ becomes

$$\mathbf{v}_{f/n}^f = \boldsymbol{\nu}_1 + \boldsymbol{\nu}_2 \times \mathbf{r}_f^b = \boldsymbol{\nu}_1 - \mathbf{S}(\mathbf{r}_f^b)\boldsymbol{\nu}_2, \quad (2.27)$$

where $\boldsymbol{\nu}_1 = \mathbf{v}_{b/n}^b = [u, v, w]^\top$ and $\boldsymbol{\nu}_2$ is as previously defined. A more compact expression is

$$\mathbf{v}_{f/n}^f = [\mathbf{I}_{3 \times 3} \quad -\mathbf{S}(\mathbf{r}_f^b)] \boldsymbol{\nu}. \quad (2.28)$$

The local velocity of the water particles, $\mathbf{v}_{w/n}^f$, will in this study only be related to waves. However, in a real situation it may also be affected by currents. In Section 2.5 a wave model and its relation to $\mathbf{v}_{w/n}^f$ for each foil will be derived.

Applying aerodynamic theory from Beard and McLain (2011), the lift and drag force can be expressed in terms of non-dimensional coefficients:

$$F_L = \frac{1}{2} \rho V_\infty^2 S \left[C_L(\alpha_r) + C_{L_q} \frac{c}{2V_\infty} q_{f/n}^f \right] \quad (2.29)$$

$$F_D = \frac{1}{2} \rho V_\infty^2 S \left[C_D(\alpha_r) + C_{D_q} \frac{c}{2V_\infty} q_{f/n}^f \right] \quad (2.30)$$

Here, $S = c \cdot b$, where c and b is chord length and span of the foil, respectively. The terms on the right-hand side in the brackets depends on the rotation of the foil relative to the NED frame. To simplify, C_{L_q} and C_{D_q} is in this study assumed to be zero. Equation (2.29) and (2.30) becomes

$$F_L = \frac{1}{2} \rho V_\infty^2 S C_L(\alpha_r) \quad (2.31)$$

$$F_D = \frac{1}{2} \rho V_\infty^2 S C_D(\alpha_r). \quad (2.32)$$

The coefficient $C_L(\alpha_r)$ is nonlinear. According to Beard and McLain (2011), it can be composed out of a linear coefficient

$$C_{L_{lin}}(\alpha_r) = C_{L_{lin},0} + C_{L_\alpha} \alpha_r \quad (2.33)$$

that dominates for small angles of attack, and a nonlinear coefficient

$$C_{L_{flat\ plate}} = 2 \text{sign}(\alpha_r) \sin^2(\alpha_r) \cos(\alpha_r), \quad (2.34)$$

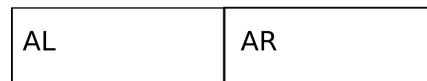
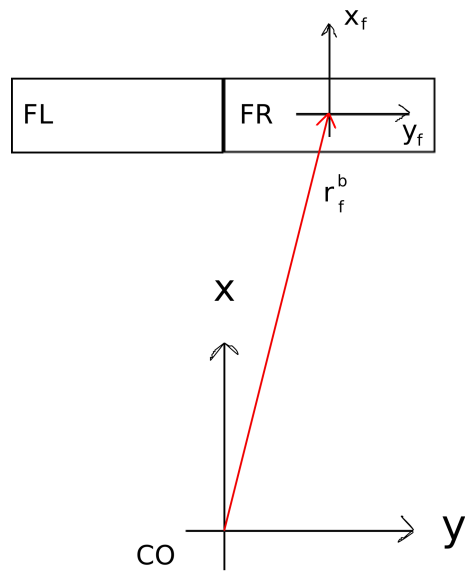


Figure 2.4: Configuration of lifting foils

which equals the corresponding coefficient of a flat plate and is dominating at large angles of attack, when stall conditions occur. The two coefficients are combined together with the equation

$$C_L(\alpha_r) = (1 - \sigma(\alpha_r))C_{L_{lin}} + \sigma(\alpha_r)C_{L_{flat\ plate}}, \quad (2.35)$$

where

$$\sigma(\alpha_r) = \frac{1 + e^{-M(\alpha_r - \alpha_0)} + e^{M(\alpha_r + \alpha_0)}}{(1 + e^{-M(\alpha_r - \alpha_0)})(1 + e^{M(\alpha_r + \alpha_0)})}. \quad (2.36)$$

This is a blending function with cutoff at $\pm\alpha_0$ and transition rate M , with the result that

$$C_L(\alpha_r) \approx C_{L_{lin}}(\alpha_r), \quad \forall -\alpha_0 < \alpha_r < \alpha_0. \quad (2.37)$$

$\alpha_0 = 20^\circ$ and $M = 2$ has been used in the model. Inserting (2.22) into (2.33) gives

$$\begin{aligned} C_{L_{lin}}(\alpha_r) &= C_{L_{lin},0} + C_{L_\alpha}(\alpha^* + \delta + \alpha_\infty) \\ &= (C_{L_{lin},0} + C_{L_\alpha}\alpha^*) + C_{L_\alpha}(\delta + \alpha_\infty), \end{aligned} \quad (2.38)$$

where the first term is constant. Then we define

$$C_{L_0} := C_{L_{lin},0} + C_{L_\alpha}\alpha^* \quad (2.39)$$

and obtain

$$C_{L_{lin}}(\delta, \alpha_\infty) = C_{L_0} + C_{L_\alpha}(\delta + \alpha_\infty). \quad (2.40)$$

We assume the foil is designed such that

$$C_{L_0} = C_L(\alpha^*) = \frac{\frac{1}{4}mg}{\frac{1}{2}\rho V_\infty^2 S} = \frac{mg}{2\rho V_\infty^2 S} \quad (2.41)$$

in order to give lift equal to a quarter of the weight of the craft when $\alpha = \alpha^*$. An approximation for C_{L_α} provided by Beard and McLain (2011) is

$$C_{L_\alpha} = \frac{\pi AR}{1 + \sqrt{1 + (AR/2)^2}}, \quad (2.42)$$

where $AR = b/c$ is the *aspect ratio* of the foil.

The drag coefficient $C_D(\alpha_r)$ in (2.32) is also nonlinear. Beard and McLain (2011) is approximating this by the formula

$$C_D(\alpha_r) = C_{D_p} + \frac{C_{L_{lin}}(\delta, \alpha_\infty)^2}{\pi e AR}, \quad (2.43)$$

where C_{D_p} is a constant due to *plastic drag*, and e is *Oswald efficiency factor*, with a range between 0.8 and 1.0 (Beard and McLain, 2011). In this simulation model, we have simplified by assuming $C_{D_p} = 0$, and $e = 1$ has been used.

The foil forces has to be expressed in the body frame of the craft. Because the lift and drag force for each foil is expressed normal and parallel to the local inflow, these forces first

have to be expressed in the local coordinate system of each foil. A rotation matrix for the cross section of the foil can be used:

$$\mathbf{f}^f = \begin{bmatrix} f_x^f \\ f_y^f \\ f_z^f \end{bmatrix} = \begin{bmatrix} -\cos(\alpha_\infty) & \sin(\alpha_\infty) \\ 0 & 0 \\ -\sin(\alpha_\infty) & -\cos(\alpha_\infty) \end{bmatrix} \begin{bmatrix} F_D \\ F_L \end{bmatrix} \quad (2.44)$$

In body frame each foil is giving a force $\mathbf{f}^b = \mathbf{f}^f$ and a moment $\mathbf{m}^b = \mathbf{r}_f^b \times \mathbf{f}^f = \mathbf{S}(\mathbf{r}_f^b)\mathbf{f}^f$. Expressed as one vector which can be applied to the dynamics model:

$$\Delta\boldsymbol{\tau}_{c,foil} = \begin{bmatrix} \mathbf{f}^f \\ \mathbf{S}(\mathbf{r}_f^b)\mathbf{f}^f \end{bmatrix} \quad (2.45)$$

The physical limitation for deviation in foil angles is assumed to be $\pm 20^\circ$.

2.3 Rudders

The craft is equipped with four flaps giving lateral forces, one behind each foil leg. Figure 2.5 shows the configuration of these flaps seen from above. The deflection of a flap is denoted by δ^r , and positive direction is determined by applying the right-hand rule about the body-frame z-axis. This corresponds to positive deflection in clockwise direction, when seen from above. Since the hydrodynamics of the foil legs is not implemented to the model, the flaps will here be modelled as vertical standing foils with a profile symmetric about the chord line. Hence, each of these foils will behave almost like a rudder, and will be referred to as *rudders* to distinguish from the lifting foils.

Figure 2.6 shows the profile of a rudder. x_r and y_r denotes the x- and y-axis of the local rudder coordinate frame $\{r\} = (x_r, y_r, z_r)$, and are parallel to the body-frame x- and y-axis, respectively. V_∞^r is the velocity of the inflow, due to the relative motion between the rudder and the water. α_∞^r is the angle between the inflow direction and the x-axis of the rudder. The net force vector acting on the rudder is divided into a lifting component F_L^r , which is perpendicular to the inflow direction, and one drag component F_D^r in the same direction as the inflow. Vertical drag forces, i.e. in the z direction of the craft's body frame, are in this study neglected.

Due to the symmetric profile, there is no lift force due to curvature, and no ideal angle of attack. Figure 2.6 gives that the angle relative to the inflow becomes:

$$\alpha_r^r = \delta^r - \alpha_\infty^r \quad (2.46)$$

V_∞^r and α_∞^r are calculated in the same way as for the lifting foils, but with the local relative velocities u_{rel}^r along the x_r axis and v_{rel}^r along the y_r axis:

$$V_\infty^r = \sqrt{(u_{rel}^r)^2 + (v_{rel}^r)^2} \quad (2.47)$$

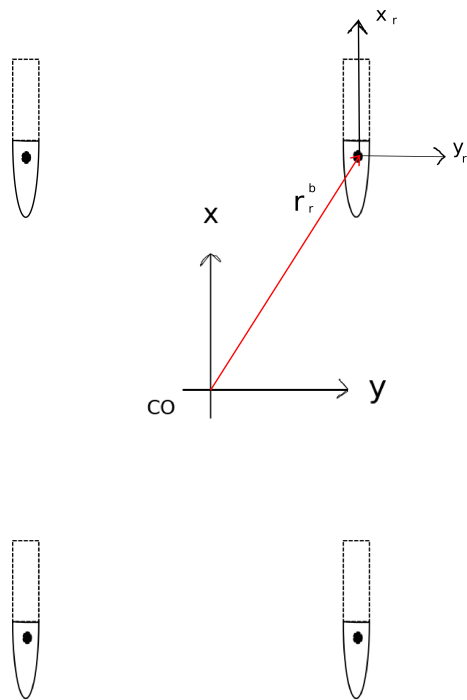


Figure 2.5: Configuration of rudders, seen from above

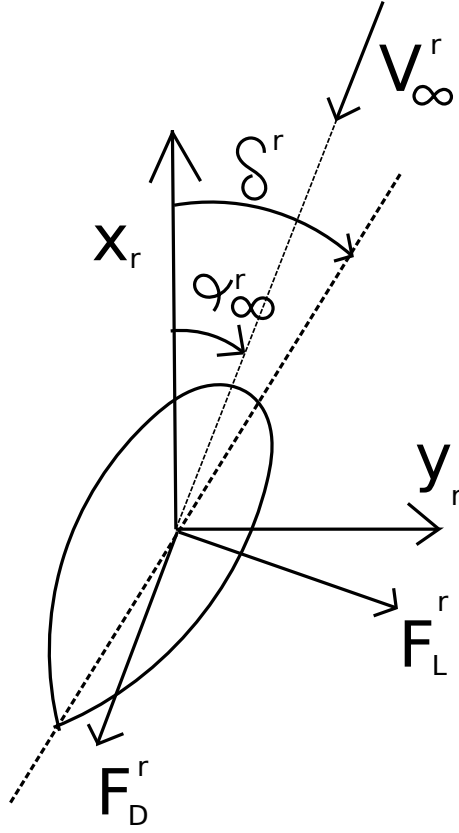


Figure 2.6: Profile of a rudder, seen from above

$$\alpha_{\infty}^r = \tan^{-1} \left(\frac{v_{rel}^r}{u_{rel}^r} \right) \quad (2.48)$$

Similarly as for the lifting foils, the relative velocity $\mathbf{v}_{rel}^r = [u_{rel}^r, v_{rel}^r, w_{rel}^r]^{\top}$ is defined by

$$\mathbf{v}_{rel}^r := \mathbf{v}_{r/n}^r - \mathbf{v}_{w/n}^r, \quad (2.49)$$

where the local velocity vector $\mathbf{v}_{r/n}^r = [u^r, v^r, w^r]^{\top}$ depends on the rudder position \mathbf{r}_r^b relative to the body-frame CO:

$$\mathbf{v}_{r/n}^r = [\mathbf{I}_{3 \times 3} \quad -\mathbf{S}(\mathbf{r}_r^b)] \boldsymbol{\nu} \quad (2.50)$$

The velocity of the water particles, $\mathbf{v}_{w/n}^r$, will depend on the wave model being derived in Section 2.5.

Assuming small rudder deflections, and considering the fact that loss of lift not is as critical as for the lifting foils, the linear model of the lift coefficient is chosen:

$$C_L^r(\alpha_r^r) = C_{L_{\alpha}}^r \alpha_r^r = C_{L_{\alpha}}^r (\delta^r + \alpha_{\infty}^r) \quad (2.51)$$

Due to symmetry, there is no lift at $\alpha_r^r = 0$, so $C_L^r(0)$ has to be zero.

The plastic drag force at zero deflection angle is assumed such small compared to the drag forces of the foils that it can be neglected. Hence, a simplification of (2.43) is used to find the drag coefficient:

$$C_D^r(\alpha_r^r) = \frac{[C_{L_\alpha}^r(\delta^r + \alpha_\infty^r)]^2}{\pi e AR} \quad (2.52)$$

The lift and drag forces on each rudder becomes

$$F_L^r = \frac{1}{2} \rho S^r V_\infty^2 C_L^r(\alpha_r^r) \quad (2.53)$$

$$F_D^r = \frac{1}{2} \rho S^r V_\infty^2 C_D^r(\alpha_r^r), \quad (2.54)$$

where $S^r = c^r b^r$ is the 2D area of the rudder, similar as for a lifting foil. c^r and b^r are cord length and height of the rudder, respectively.

Figure 2.6 gives that the lift and drag force transformed into the rudder frame becomes:

$$\mathbf{f}^r = \begin{bmatrix} f_x^r \\ f_y^r \\ f_z^r \end{bmatrix} = \begin{bmatrix} -\cos(\alpha_\infty^r) & -\sin(\alpha_\infty^r) \\ -\sin(\alpha_\infty^r) & \cos(\alpha_\infty^r) \\ 0 & 0 \end{bmatrix} \begin{bmatrix} F_D^r \\ F_L^r \end{bmatrix} \quad (2.55)$$

Similarly as for the lifting foils, this force vector is transformed into body frame with the formula

$$\Delta \boldsymbol{\tau}_{c,rudder} = \begin{bmatrix} \mathbf{f}^r \\ \mathbf{S}(\mathbf{r}_r^b) \mathbf{f}^r \end{bmatrix}. \quad (2.56)$$

The physical limitation for rudder angles is assumed to be $\pm 20^\circ$.

The total actuator forces becomes:

$$\boldsymbol{\tau}_c = \sum_{i=1}^4 \Delta \boldsymbol{\tau}_{c,foil}^i + \sum_{j=1}^4 \Delta \boldsymbol{\tau}_{c,rudder}^j \quad (2.57)$$

2.4 Allocation of foil angles

The inputs from the controller is given in quantities associated with motions in the different DOF. The craft is supposed to be controlled in heave, roll, pitch and yaw. The following control inputs will be used:

- δ_a : Giving positive moment in roll
- δ_e : Giving positive moment in pitch

- δ_z : Giving upward force in heave
- δ_r : Giving positive moment in yaw

The subscripts a , e and r are adopted from the aircraft terminology used by Beard and McLain (2011), and are abbreviations for *aileron*, *elevator* and *rudder*, respectively. Following the convention used by Beard and McLain (2011), these inputs can be thought of as a composite deflection, where the magnitude equals the average of the net angular deviation contributing to force or moment in the respective DOF, on each foil or rudder. The definitions are:

$$\delta_a := \frac{1}{4}[\delta_{FL} - \delta_{FR} + \delta_{AL} - \delta_{AR}] \quad (2.58)$$

$$\delta_e := \frac{1}{4}[\delta_{FL} + \delta_{FR} - \delta_{AL} - \delta_{AR}] \quad (2.59)$$

$$\delta_z := \frac{1}{4}[\delta_{FL} + \delta_{FR} + \delta_{AL} + \delta_{AR}] \quad (2.60)$$

$$\delta_r := \frac{1}{4}[\delta_{FL}^r + \delta_{FR}^r - \delta_{AL}^r - \delta_{AR}^r] \quad (2.61)$$

The capital letter subscripts denotes the position of the respective foil or rudder, each defined in Table 2.3.

Table 2.3: Controlled deviations in foil and rudder angles

δ_{FL}	Front left foil
δ_{FR}	Front right foil
δ_{AL}	Aft left foil
δ_{AR}	Aft right foil
δ_{FL}^r	Front left rudder
δ_{FR}^r	Front right rudder
δ_{AL}^r	Aft left rudder
δ_{AR}^r	Aft right rudder

Applying the constraint that change in one control input shall only result in a net force or moment (due to lift forces) in the respective DOF, and assuming equal inflow on each foil and rudder, a solution of the equation set (2.58) - (2.61) gives

$$\delta_{FL} = \delta_a + \delta_e + \delta_z \quad (2.62)$$

$$\delta_{FR} = -\delta_a + \delta_e + \delta_z \quad (2.63)$$

$$\delta_{AL} = \delta_a - \delta_e + \delta_z \quad (2.64)$$

$$\delta_{AR} = -\delta_a - \delta_e + \delta_z \quad (2.65)$$

and

$$\delta_{FL}^r = \delta_{FR}^r = \delta_r \quad (2.66)$$

$$\delta_{AL}^r = \delta_{AR}^r = -\delta_r. \quad (2.67)$$

Equation (2.62) - (2.62) assumes the foil and rudder angles such small that the linear lift coefficients are dominating. Hence, the superposition principle holds. Written in matrix form:

$$\begin{bmatrix} \delta_{FL} \\ \delta_{FR} \\ \delta_{AL} \\ \delta_{AR} \\ \delta_{FL}^r \\ \delta_{FR}^r \\ \delta_{AL}^r \\ \delta_{AR}^r \end{bmatrix} = \begin{bmatrix} 1 & 1 & 1 & 0 \\ -1 & 1 & 1 & 0 \\ 1 & -1 & 1 & 0 \\ -1 & -1 & 1 & 0 \\ 0 & 0 & 0 & 1 \\ 0 & 0 & 0 & 1 \\ 0 & 0 & 0 & -1 \\ 0 & 0 & 0 & -1 \end{bmatrix} \begin{bmatrix} \delta_a \\ \delta_e \\ \delta_z \\ \delta_r \end{bmatrix} \quad (2.68)$$

Actuator dynamics of both foils and rudders are implemented to the model as first order a low-pass filters with time constant $T_\delta = 1/20 \text{ s}$. The transfer function from a commanded angle deviation δ^c to the actual deviation δ becomes

$$\frac{\delta}{\delta^c}(s) = \frac{20}{s + 20}. \quad (2.69)$$

2.5 Wave Model

A dynamic model of waves is implemented to the simulation model in order to perform simulations of the craft when affected by waves. The interaction between the waves and the craft will in our simulations solely be related to the wave-induced local velocity of the water surrounding the lifting foils and rudders. Wave-induced forces due to local pressure differences in undisturbed water (Froude-Kriloff forces), as well as added-mass effects due to local acceleration of the water, are neglected. We also assume that the waves are unaffected by the foils, such that the front and aft foils are experiencing the same unaffected waves, but in different positions. Struts and other submerged appendices are assumed unaffected. In the end of this section we will have a model for the local water velocity around the lifting foils and the rudders.

2.5.1 Linear Wave Model

In order to describe the waves with a mathematical model, we do the following assumptions:

-
- Infinite water depth
 - Free water surface of infinite horizontal extent
 - Irrotational water particles
 - The water is incompressible and inviscid
 - Waves are such low compared to their wave length that a first-order approximation is valid

Remark that these assumptions are only applied to the wave model and not necessarily to other parts of the simulation model. E. g. the foils would not achieve any lifting force without some viscosity in the fluid (Faltinsen, 2005).

The craft will be simulated when sailing in *long-crested regular* waves, long-crested *irregular* waves and *short-crested* irregular waves. Mathematical models of these waves will be provided in the rest of this subsection. For the irregular waves, the distribution of frequencies are determined by a *wave spectrum* described in Section 2.5.2.

Long-crested regular waves

Figure 2.7 shows a regular *long-crested* wave in an xz coordinate frame. It is propagating in positive x direction with a mean free-surface at $z = 0$. Let ζ denote the *wave profile*, i.e. the elevation of the water surface compared to completely calm water, and let ϕ denote the *velocity potential* of the water particles in the wave. With the assumptions above, Faltinsen (1990) provides the following expressions to describe ζ and ϕ :

$$\zeta(x, t) = \zeta_A \cos(kx - \omega t) \quad (2.70)$$

$$\phi(x, z, t) = \frac{g\zeta_A}{\omega} e^{kz} \sin(kx - \omega t) \quad (2.71)$$

Here, ζ_A is the *wave amplitude*, k is the *wave number*, ω is the *circular frequency*, g is the gravity acceleration and t is the time. Due to our assumption of infinite water depth, the wave number is given by the *dispersion relation*

$$k = \frac{\omega^2}{g}. \quad (2.72)$$

The velocity components of the water particles are derived by taking the partial derivatives of ϕ with respect to x and z :

$$u(x, z, t) = \frac{\partial \phi}{\partial x} = \frac{kg\zeta_A}{\omega} e^{kz} \cos(kx - \omega t) \quad (2.73)$$

$$w(x, z, t) = \frac{\partial \phi}{\partial z} = \frac{kg\zeta_A}{\omega} e^{kz} \sin(kx - \omega t) \quad (2.74)$$

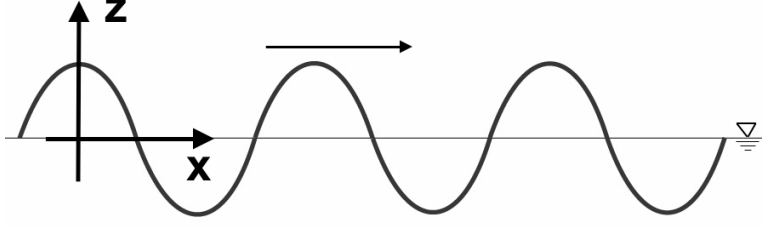


Figure 2.7: Regular Wave

Long-crested irregular waves

Long-crested *irregular* waves cannot be described by a single sinusoidal term since the water surface does not follow a regular sinus curve. For linear waves, the superposition principle can be used to describe irregular waves as a finite or infinite sum of regular waves with different amplitude, frequency and phase (Faltinsen, 1990). Considering a long-crested irregular sea that propagates along the positive x -axis and can be described as the sum of N regular wave components. The wave elevation and velocity potential can then be written as

$$\zeta(x, t) = \sum_{n=1}^N \zeta_{A_n} \cos(k_n x - \omega_n t + \varepsilon_n) \quad (2.75)$$

$$\phi(x, z, t) = \sum_{n=1}^N \frac{g \zeta_{A_n}}{\omega_n} e^{k_n z} \sin(k_n x - \omega_n t + \varepsilon_n), \quad (2.76)$$

where ζ_{A_n} , k_n , ω_n and ε_n respectively denotes the wave amplitude, wave number, circular frequency and phase angle of wave component number n . It follows from (2.76) that

$$u(x, z, t) = \sum_{n=1}^N \frac{k_n g \zeta_{A_n}}{\omega_n} e^{k_n z} \cos(k_n x - \omega_n t + \varepsilon_n) \quad (2.77)$$

$$w(x, z, t) = \sum_{n=1}^N \frac{k_n g \zeta_{A_n}}{\omega_n} e^{k_n z} \sin(k_n x - \omega_n t + \varepsilon_n). \quad (2.78)$$

Short-crested irregular waves

Short-crested sea consist of two or more wave components propagating in different directions. Let the xy -frame represent the sea surface, and z the vertical direction. For an arbitrarily wave component propagating in direction θ relative to the x -axis (positive angle determined by the right-hand rule), the surface elevation and velocity potential respectively

becomes (Faltinsen, 1990)

$$\zeta(x, y, t) = \zeta_A \cos(kx \cos \theta + ky \sin \theta - \omega t + \varepsilon) \quad (2.79)$$

$$\phi(x, y, z, t) = \frac{g\zeta_A}{\omega} e^{kz} \sin(kx \cos \theta + ky \sin \theta - \omega t + \varepsilon). \quad (2.80)$$

Summarizing regular wave components with N frequencies and K directions, we get

$$\zeta(x, y, t) = \sum_{n=1}^N \sum_{k=1}^K \zeta_{A_{nk}} \cos(k_n x \cos \theta_k + k_n y \sin \theta_k - \omega_n t + \varepsilon_{nk}) \quad (2.81)$$

$$\phi(x, y, z, t) = \sum_{n=1}^N \sum_{k=1}^K \frac{g\zeta_{A_{nk}}}{\omega_n} e^{k_n z} \sin(k_n x \cos \theta_k + k_n y \sin \theta_k - \omega_n t + \varepsilon_{nk}). \quad (2.82)$$

With partial derivation of ϕ with respect to x , y and z , we respectively obtain the velocity components in the x-, y- and z-direction:

$$u(x, y, z, t) = \sum_{n=1}^N \sum_{k=1}^K \frac{k_n g \zeta_{A_{nk}}}{\omega_n} e^{k_n z} \cos(k_n x \cos \theta_k + k_n y \sin \theta_k - \omega_n t + \varepsilon_{nk}) \cos \theta_k \quad (2.83)$$

$$v(x, y, z, t) = \sum_{n=1}^N \sum_{k=1}^K \frac{k_n g \zeta_{A_{nk}}}{\omega_n} e^{k_n z} \cos(k_n x \cos \theta_k + k_n y \sin \theta_k - \omega_n t + \varepsilon_{nk}) \sin \theta_k \quad (2.84)$$

$$w(x, y, z, t) = \sum_{n=1}^N \sum_{k=1}^K \frac{k_n g \zeta_{A_{nk}}}{\omega_n} e^{k_n z} \sin(k_n x \cos \theta_k + k_n y \sin \theta_k - \omega_n t + \varepsilon_{nk}) \quad (2.85)$$

2.5.2 Wave Spectrum

Natural waves generated by wind are in almost every situations irregular, with the energy distributed over a range of frequencies. This energy distribution is referred to as the *wave spectrum* of the sea and can be described by a mathematical function $S(\omega)$ depending on location and other parameters as e.g. the wind speed. $S(\omega)$ is, by definition, related to the total wave energy E in one unit area by integration over all frequencies (Myrhaug, 2007):

$$\frac{E}{\rho g} = \int_0^{\infty} S(\omega) d\omega \quad (2.86)$$

Here ρ is the water density, and g is the gravity acceleration.

With the assumption of free surface and infinite water depth, the original standardized wave spectrum developed by Pierson and Moskowitz (1963) will be satisfactory for modelling the irregular waves in our simulations. This spectrum, also known as the *PM spectrum*, is based on collected data from fully developed wind-generated seas in the North

Atlantic Ocean. The PM spectrum is given by

$$S(\omega) = A\omega^{-5} \exp(-B\omega^{-4}), \quad (2.87)$$

where

$$A = 8.1 \times 10^{-3} g^2 = \text{constant} \quad (2.88)$$

and

$$B = 0.74 \left(\frac{g}{U_{19.4}} \right)^4 = \frac{3.11}{H_s^2}. \quad (2.89)$$

Here, g is the gravity acceleration, $U_{19.4}$ is the wind speed at 19.4 m above the sea surface, and H_s is the significant wave height. Figure 2.8 shows the plot of $S(\omega)$ for wind speed $U_{19.4} = 10$ m/s.

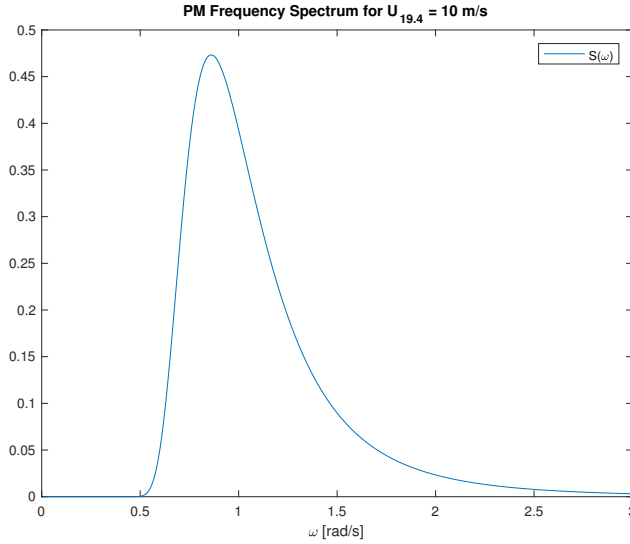


Figure 2.8: PM Frequency spectrum for wind speed $U_{19.4} = 10$ m/s. Y-axis shows absolute values for $S(\omega)$

For short-crested sea, the energy is also distributed over waves propagating in different directions. This can be modelled by a two-dimensional wave spectrum called *directional spectrum*:

$$S(\omega, \theta) = S(\omega)f(\theta) \quad (2.90)$$

Here $f(\theta)$ is the *spreading function*. According Myrhaug (2007), a standardized spreading function recommended by International Towing Tank Conference (ITTC) is

$$f(\theta) = \begin{cases} \frac{2}{\pi} \cos^2(\theta - \theta_0), & -\frac{\pi}{2} \leq (\theta - \theta_0) \leq \frac{\pi}{2}, \\ 0; & \text{elsewhere} \end{cases} \quad (2.91)$$

where θ_0 is the main wave-propagation direction. With this spreading function, and the PM spectrum $S(\omega)$, the directional spectrum $S(\omega, \theta)$ depends on two parameters which can be adjusted specifically for each simulation: $U_{19.4}$ (or H_s) and θ_0 . The total wave energy for short crested waves is found by integrating $S(\omega, \theta)$ with respect to both ω and θ :

$$\frac{E}{\rho g} = \int_0^{2\pi} \int_0^\infty S(\omega) d\omega d\theta \quad (2.92)$$

The wave and directional spectra can be used to find ζ_{A_n} and $\zeta_{A_{nk}}$ for the components of irregular long-crested and short-crested waves, respectively. According to Myrhaug (2007), the wave energy per unit area of a linear wave component is directly related to the square of its amplitude ζ_{A_n} :

$$\frac{E_n}{\rho g} = \frac{1}{2} \zeta_{A_n}^2 \quad (2.93)$$

If the frequency spectrum $S(\omega)$ is divided into N small intervals of $\Delta\omega$ (see Figure 2.9), and ω_n is the average frequency inside the n 'th interval, the energy of all wave components inside this interval becomes approximately

$$\frac{E_n}{\rho g} = S(\omega_n) \Delta\omega. \quad (2.94)$$

For short-crested waves, the spreading function can be divided into K small sectors of $\Delta\theta$. This means that for each frequency interval $\Delta\omega$, the energy $\frac{E_n}{\rho g}$ can further be divided into K sectors of $\Delta\theta$, with energy

$$\frac{E_{nk}}{\rho g} = S(\omega_n, \theta_k) \Delta\omega \Delta\theta. \quad (2.95)$$

From (2.93) and (2.94) it follows that the amplitude of each component in a frequency spectrum is given by

$$\zeta_{A_n} = \sqrt{2S(\omega_n) \Delta\omega}. \quad (2.96)$$

For a directional spectrum, it follows from (2.93) and (2.95) that the amplitude of each component is given by

$$\zeta_{A_{nk}} = \sqrt{2S(\omega_n, \theta_k) \Delta\omega \Delta\theta}. \quad (2.97)$$

In order to make a realistic simulation of the waves, Faltinsen (1990) recommends using a large number of wave components, minimum 1000. However, this will increase the computational demand and, depending on the computer running the simulation, significantly increase the simulation time. In our case, the goal is to study how the RCS being designed in Chapter 4 is able to penalize the disturbances caused by orbital motions of the water particles around each foil, when sailing in irregular waves. We do the assumption that the controller's behaviour is similar when the foils are exposed to disturbances due to a smaller number of components. Hence, we choose to use maximum 100 wave component in the simulations. Anyway, by only considering wave loads from orbital motions of particles,

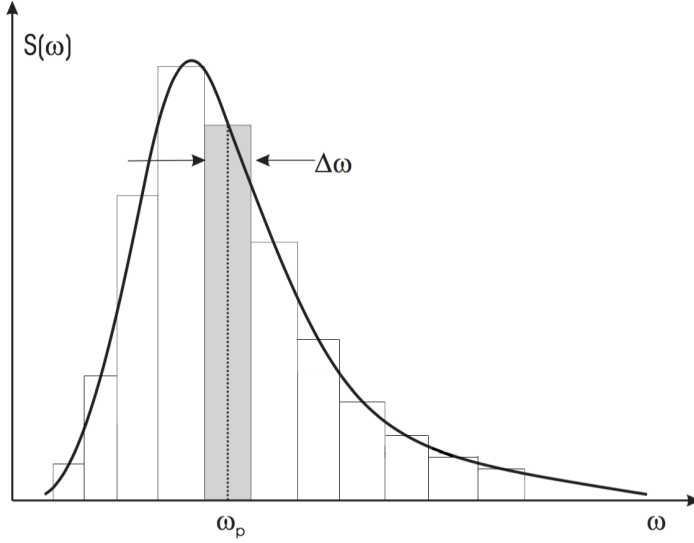


Figure 2.9: Frequency spectrum divided into rectangular components

and with all the other assumptions applied to the wave model and the hydrodynamics of the foils, we cannot assume our simulation model recreating realistic magnitudes for the wave loads. However, we obtain different, irregular disturbance forces on each foil.

2.5.3 Velocity of Water Particles in a Specific Location in the NED frame

In order to implement the wave model to the rest of the simulation model, we let the wave components be described by a coordinates in the NED frame. We let the x-, y- and z-axis equal the *North*, *East* and *Down* axis, respectively, and the rotation θ becomes positive in clockwise direction when seen from above. For a water particle in position $\mathbf{P}_{w/n}^n = [p_n, p_e, p_d]^\top$ in the NED frame, p_n and p_e can directly replace x and y , respectively, in the equations for $\zeta(x, y, t)$ and $\phi(x, y, z, t)$. However, since the direction of the gravity acceleration always is pointing downward, z has to be replaced with $-p_d$. According to the rules of differentiation, this will change the sign of $w(x, y, t)$, which now is defined as positive downward. If we now define $u_{w/n}^n$, $v_{w/n}^n$ and $w_{w/n}^n$ as the water particle's velocity components along the *North*, *East* and *Down* axis, respectively, substitutions into Equation (2.83) to (2.85) gives

$$u_{w/n}^n(p_n, p_e, p_d, t) = \sum_{n=1}^N \sum_{k=1}^K \frac{k_n g \zeta_{A_{nk}}}{\omega_n} e^{-k_n p_d} \cos[W(p_n, p_e, t)] \cos \theta_k, \quad (2.98)$$

$$v_{w/n}^n(p_n, p_e, p_d, t) = \sum_{n=1}^N \sum_{k=1}^K \frac{k_n g \zeta_{A_{nk}}}{\omega_n} e^{-k_n p_d} \cos[W(p_n, p_e, t)] \sin \theta_k \quad (2.99)$$

and

$$w_{w/n}^n(p_n, p_e, p_d, t) = - \sum_{n=1}^N \sum_{k=1}^K \frac{k_n g \zeta_{A_{nk}}}{\omega_n} e^{-k_n p_d} \sin[W(p_n, p_e, t)], \quad (2.100)$$

where

$$W(p_n, p_e, t) = k_n p_n \cos \theta_k + k_n p_e \sin \theta_k - \omega_n t + \varepsilon_{nk}. \quad (2.101)$$

Since we want to find the velocity of the water particles surrounding each foil and rudder, we need to find the instant position of each foil and rudder relative to the NED frame. For each time instant, the origin of the craft has a position $\mathbf{P}_{b/n}^n$ and orientation Θ_{nb} relative to the NED frame. For each foil, located by a vector \mathbf{r}_f^b in the crafts' body frame, the position relative to the NED frame becomes

$$\mathbf{P}_{f/n}^n = \mathbf{P}_{b/n}^n + \mathbf{R}_b^n(\Theta_{nb}) \mathbf{r}_f^b, \quad (2.102)$$

where $\mathbf{R}_b^n(\Theta_{nb})$ is the rotation matrix defined in (2.9). Similarly for each rudder located in the crafts' body frame by a vector \mathbf{r}_r^b :

$$\mathbf{P}_{r/n}^n = \mathbf{P}_{b/n}^n + \mathbf{R}_b^n(\Theta_{nb}) \mathbf{r}_r^b \quad (2.103)$$

The components p_n , p_e and p_d of $\mathbf{P}_{f/n}^n$ or $\mathbf{P}_{r/n}^n$ can be inserted into Equation (2.99) to (2.100) in order to find the local velocity of the water particles expressed in the NED frame. We denote this velocity by the vector

$$\mathbf{v}_{w/n}^n = \begin{bmatrix} u_{w/n}^n \\ v_{w/n}^n \\ w_{w/n}^n \end{bmatrix}. \quad (2.104)$$

Finally, in order to find the velocity of the water particles expressed in the local frame of each foil and rudder, a rotation matrix between the NED frame and these coordinate frames has to be applied. Since all these coordinate frames are parallel with the body frame, the transpose of the rotation matrix $\mathbf{R}_b^n(\Theta_{nb})$ can be used:

$$\mathbf{v}_{w/n}^f = \mathbf{R}_b^n(\Theta_{nb})^\top \mathbf{v}_{w/n}^n \quad (2.105)$$

$$\mathbf{v}_{w/n}^r = \mathbf{R}_b^n(\Theta_{nb})^\top \mathbf{v}_{w/n}^n \quad (2.106)$$

2.6 Sensors and Measurement Noise

We let the model be equipped with sensors measuring the states that are necessary for the different controllers. In real situations, it is typical to not measure all the states independently, but rather measure some of the states and use an observer to estimate the remaining

states as well as filtering out the sensor noise (Sørensen, 2013). This observer can also be used to predict the states in the case of temporally loss of measurements. However, in this study we assume that all the states necessary for the controllers are measured. The \mathcal{H}_2 receives signals for position and velocity in heave, roll and pitch, and these six signals are contaminated with white measurement noise which has a standard deviation of approximately 1-3% of the expected standard deviation of the state being measured. This is implemented in Simulink by using the block for Band-Limited White Noise, where the sampling time is set to 0.01 s, and the variance is set to $1 \cdot 10^{-8}$. The noise signal is added to each measurement signals going to the \mathcal{H}_2 controller, as illustrated in Figure 2.10.

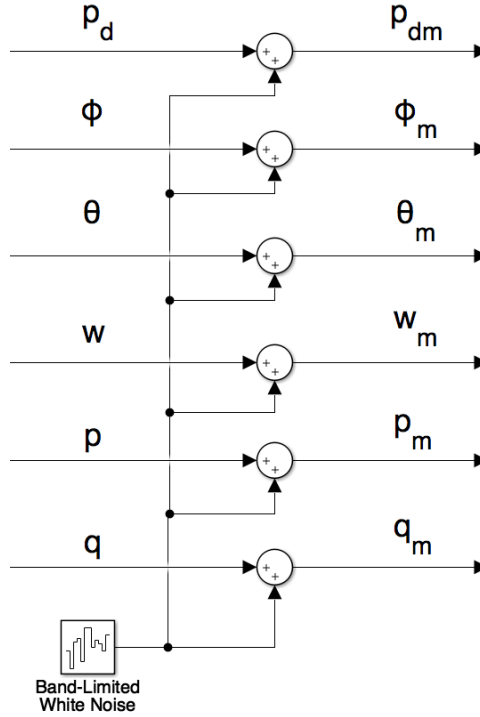


Figure 2.10: Block diagram from Simulink showing the noise signal being added to the measurement signals before entering the \mathcal{H}_2 controller. The m-subscript denotes measured state with noise

All the external controllers (i. e. not the \mathcal{H}_2 controller) are fed with signals not containing noise. This is because we in this study primarily are focusing on designing the \mathcal{H}_2 controller and using its built-in observer functionality, while the external controllers, as mentioned in the introduction, more are used as a tool to handle surge sway and yaw when simulating in 6 DOF.

Linearized Model

Design of both the \mathcal{H}_2 -optimized and the LQR controller assumes that the plant that are going to be controlled is linear. See Section 1.4.2. But, the simulation model of the craft is highly nonlinear, and when considering all its 6 DOF given in Equation (2.3), it will not make sense to linearize about a trim condition where all the sates remain constant. This because one or more of the states related to the craft's position or heading in the *North-East* plane is changing as the craft is moving along the surface of the water. However, since the objective of the RCS is to enforce the craft to maintain approximately constant states in *heave*, *roll* and *pitch*, we only need linearized Equations of Motion (EOM) for these DOF. Of same reason, the RCS will only use actuators acting in these 3 DOF, which means only the lifting foils. Later in this chapter we will see that the linearized dynamics for heave, roll and pitch is independent of the remaining DOF, assuming a constant speed in surge and negligible motions in sway.

3.1 Rigid Body Dynamics

Recall the equations (2.19) and (2.20), in Section 2.1.2, for the nonlinear rigid-body dynamics of the simulation model:

$$\dot{\boldsymbol{\eta}} = \mathbf{J}_{\Theta}(\boldsymbol{\eta})\boldsymbol{\nu}$$

$$\mathbf{M}_{RB}\dot{\boldsymbol{\nu}} + \mathbf{C}_{RB}(\boldsymbol{\nu})\boldsymbol{\nu} + \mathbf{g}(\boldsymbol{\eta}) = \boldsymbol{\tau}_c$$

Considering only *heave*, *roll* and *pitch*, we define the new, reduced position and velocity vectors $\boldsymbol{\eta}_3$ and $\boldsymbol{\nu}_3$, respectively:

$$\boldsymbol{\eta}_3 = [p_d \quad \phi \quad \theta]^\top \tag{3.1}$$

$$\boldsymbol{\nu}_3 = [w \quad p \quad r]^\top \quad (3.2)$$

We only consider control inputs from the lifting foils. From Section 2.4, we see that these are δ_a , δ_e and δ_z , controlling roll, pitch and heave, respectively. We define the control-input vector

$$\boldsymbol{\delta} = [\delta_a \quad \delta_e \quad \delta_z]^\top. \quad (3.3)$$

We choose to linearize about a trim condition $(\boldsymbol{\eta}_3^*, \boldsymbol{\nu}_3^*, \boldsymbol{\delta}^*)$ corresponding to the expected cruise condition, with surge speed U_0 and vertical position $-h_0$, as defined in Table 2.2. In the linearization process, we also assume the speed in sway, v to be zero, and that the yaw rate r is small. The trim states and input vector are respectively defined as

$$\boldsymbol{\eta}_3^* := \begin{bmatrix} -h_0 \\ 0 \\ 0 \end{bmatrix}, \quad (3.4)$$

$$\boldsymbol{\nu}_3^* := \begin{bmatrix} 0 \\ 0 \\ 0 \end{bmatrix} \quad (3.5)$$

and

$$\boldsymbol{\delta}^* := [0, 0, 0]^\top. \quad (3.6)$$

We let $\bar{\boldsymbol{\eta}}_3 := \boldsymbol{\eta}_3 - \boldsymbol{\eta}_3^*$, $\bar{\boldsymbol{\nu}}_3 := \boldsymbol{\nu}_3 - \boldsymbol{\nu}_3^*$ and $\bar{\boldsymbol{\delta}} := \boldsymbol{\delta} - \boldsymbol{\delta}^*$ denote the deviations away from the trim condition. Expanded:

$$\bar{\boldsymbol{\eta}}_3 = \begin{bmatrix} \bar{z} \\ \phi \\ \theta \end{bmatrix}, \quad (3.7)$$

$$\bar{\boldsymbol{\nu}}_3 = \begin{bmatrix} w \\ p \\ q \end{bmatrix} = \boldsymbol{\nu}_3 \quad (3.8)$$

and

$$\bar{\boldsymbol{\delta}} = [\delta_a, \delta_e, \delta_z]^\top = \boldsymbol{\delta}, \quad (3.9)$$

where $\bar{z} := p_d - (-h_0)$. Since $\bar{\boldsymbol{\delta}} = \boldsymbol{\delta}$ and $\bar{\boldsymbol{\nu}}_3 = \boldsymbol{\nu}_3$, they will from now only be denoted as $\boldsymbol{\delta}$ and $\boldsymbol{\nu}_3$, respectively.

We define the functions

$$\mathbf{f}_1(\boldsymbol{\eta}_3, \boldsymbol{\nu}_3, \boldsymbol{\delta}) := \dot{\boldsymbol{\eta}}_3 \quad (3.10)$$

and

$$\mathbf{f}_2(\boldsymbol{\eta}_3, \boldsymbol{\nu}_3, \boldsymbol{\delta}) := \dot{\boldsymbol{\nu}}_3. \quad (3.11)$$

The linearizations about the trim condition are defined by

$$\dot{\boldsymbol{\eta}}_3 = \frac{\partial \mathbf{f}_1(\boldsymbol{\eta}_3^*, \boldsymbol{\nu}_3^*, \boldsymbol{\delta}^*)}{\partial \boldsymbol{\eta}_3} \bar{\boldsymbol{\eta}}_3 + \frac{\partial \mathbf{f}_1(\boldsymbol{\eta}_3^*, \boldsymbol{\nu}_3^*, \boldsymbol{\delta}^*)}{\partial \boldsymbol{\nu}_3} \boldsymbol{\nu}_3 + \frac{\partial \mathbf{f}_1(\boldsymbol{\eta}_3^*, \boldsymbol{\nu}_3^*, \boldsymbol{\delta}^*)}{\partial \boldsymbol{\delta}} \boldsymbol{\delta} \quad (3.12)$$

and

$$\dot{\boldsymbol{\nu}}_3 = \frac{\partial \mathbf{f}_2(\boldsymbol{\eta}_3^*, \boldsymbol{\nu}_3^*, \boldsymbol{\delta}^*)}{\partial \boldsymbol{\eta}_3} \bar{\boldsymbol{\eta}}_3 + \frac{\partial \mathbf{f}_2(\boldsymbol{\eta}_3^*, \boldsymbol{\nu}_3^*, \boldsymbol{\delta}^*)}{\partial \boldsymbol{\nu}_3} \boldsymbol{\nu}_3 + \frac{\partial \mathbf{f}_2(\boldsymbol{\eta}_3^*, \boldsymbol{\nu}_3^*, \boldsymbol{\delta}^*)}{\partial \boldsymbol{\delta}} \boldsymbol{\delta}. \quad (3.13)$$

3.1.1 Linearized Kinematics

The kinematic equations for heave roll and pitch can easily be separated from the similar equations of the remaining DOF. From (2.8) and (2.9) we extract

$$\dot{p}_d = -\sin(\theta)u + \cos(\theta)\sin(\phi)v + \cos(\theta)\cos(\phi)w, \quad (3.14)$$

and from (2.8) and (2.10) we extract

$$\dot{\phi} = p + \sin(\phi)\tan(\theta)q + \cos(\phi)\tan(\theta)r \quad (3.15)$$

$$\dot{\theta} = \cos(\phi)q - \sin(\phi)r. \quad (3.16)$$

Linearizing these according to (3.12) gives:

$$\dot{\hat{z}} = -U_0\theta + w \quad (3.17)$$

$$\dot{\phi} = p \quad (3.18)$$

$$\dot{\theta} = q. \quad (3.19)$$

These can be expressed in vectorial form as

$$\dot{\bar{\eta}}_3 = \mathbf{A}_{\eta_3} \bar{\eta}_3 + \boldsymbol{\nu}_3, \quad (3.20)$$

where

$$\mathbf{A}_{\eta_3} = \begin{bmatrix} 0 & 0 & -U_0 \\ 0 & 0 & 0 \\ 0 & 0 & 0 \end{bmatrix}. \quad (3.21)$$

3.1.2 Linearized Kinetics

For the kinetics, (2.20) can be rewritten as

$$\dot{\boldsymbol{\nu}} = \mathbf{M}_{RB}^{-1} \left(-\mathbf{C}_{RB}(\boldsymbol{\nu})\boldsymbol{\nu} - \mathbf{g}(\boldsymbol{\eta}) + \boldsymbol{\tau}_c(\boldsymbol{\nu}, \boldsymbol{\delta}) \right). \quad (3.22)$$

Here, it is more difficult to directly extract three uncoupled differential equations for the desired DOF. This due to the mass matrix \mathbf{M}_{RB} , which is not necessarily diagonal. We see this by expanding the the definition given in (2.12):

$$\mathbf{M}_{RB} = \begin{bmatrix} m & 0 & 0 & 0 & mz_g & -my_g \\ 0 & m & 0 & -mz_g & 0 & mx_g \\ 0 & 0 & m & my_g & -mx_g & 0 \\ 0 & -mz_g & my_g & I_x & -I_{xy} & -I_{xz} \\ mz_g & 0 & -mx_g & -I_{yx} & I_y & -I_{yz} \\ -my_g & mx_g & 0 & -I_{zx} & -I_{zy} & I_z \end{bmatrix} \quad (3.23)$$

We have from Table 2.1 that $I_{xy} = I_{xz} = I_{yx} = I_{yz} = I_{zx} = I_{zy} = 0$, and that $x_g = y_g = 0$, but $z_g \neq 0$. Hence, we see from the mass matrix in (3.23) that forces acting in the x- and y-direction, in the body frame CO, will cause angular accelerations in pitch and roll, respectively. In order to not loose the effect of these coupled dynamics, we linearize the right-hand side of all the six equations concatenated in (3.22), with respect to the three DOF heave, roll and pitch. After that, we use a *selection matrix*

$$\mathbf{L}_3 = \begin{bmatrix} 0 & 0 & 1 & 0 & 0 & 0 \\ 0 & 0 & 0 & 1 & 0 & 0 \\ 0 & 0 & 0 & 0 & 1 & 0 \end{bmatrix}, \quad (3.24)$$

satisfying $\dot{\boldsymbol{\nu}}_3 = \mathbf{L}_3 \boldsymbol{\nu}$, in order to pick the equations for the desired states. Hence, the derivative of $\boldsymbol{\nu}_3$ becomes

$$\dot{\boldsymbol{\nu}}_3 = \mathbf{L}_3 \mathbf{M}_{RB}^{-1} \left(-\mathbf{C}_{RB}(\boldsymbol{\nu}) \boldsymbol{\nu} - \mathbf{g}(\boldsymbol{\eta}) + \boldsymbol{\tau}_c(\boldsymbol{\nu}, \boldsymbol{\delta}) \right). \quad (3.25)$$

Since $\mathbf{L}_3 \mathbf{M}_{RB}^{-1}$ is constant with respect to $\boldsymbol{\eta}_3$, $\boldsymbol{\nu}_3$ and $\boldsymbol{\delta}$, the linearization of \mathbf{f}_2 , according to (3.13), becomes

$$\dot{\boldsymbol{\nu}}_3 = \mathbf{L}_3 \mathbf{M}_{RB}^{-1} \left[-\frac{\partial \mathbf{c}(\boldsymbol{\nu}_3^*)}{\partial \boldsymbol{\nu}_3} \boldsymbol{\nu}_3 - \frac{\partial \mathbf{g}(\boldsymbol{\eta}_3^*)}{\partial \boldsymbol{\eta}_3} \boldsymbol{\eta}_3 + \frac{\partial \boldsymbol{\tau}_c(\boldsymbol{\nu}_3^*, \boldsymbol{\delta}^*)}{\partial \boldsymbol{\nu}_3} \boldsymbol{\nu}_3 + \frac{\partial \boldsymbol{\tau}_c(\boldsymbol{\nu}_3^*, \boldsymbol{\delta}^*)}{\partial \boldsymbol{\delta}} \boldsymbol{\delta} \right]. \quad (3.26)$$

Here, we have defined $\mathbf{c}(\boldsymbol{\nu}_3^*) := \mathbf{C}_{RB}(\boldsymbol{\nu}^*) \boldsymbol{\nu}^*$, where \mathbf{C}_{RB} is as defined in (2.14), and $\boldsymbol{\nu}^* = [U_0 \quad 0 \quad \boldsymbol{\nu}_3^{*\top} \quad 0]^\top$ is the trim condition for velocity when including all 6 DOF.

According to Fossen (2011), we can express

$$\frac{\partial}{\partial \boldsymbol{\nu}_3} \left(\mathbf{C}_{RB}(\boldsymbol{\nu}^*) \boldsymbol{\nu}^* \right) = \mathbf{M}_{RB} \mathbf{L}_c \mathbf{U}_0 =: \mathbf{C}_{RB}^*, \quad (3.27)$$

where \mathbf{L}_c is a selection matrix defined as

$$\mathbf{L}_c = \begin{bmatrix} 0 & 0 & 0 \\ 0 & 0 & 0 \\ 0 & 0 & -1 \\ 0 & 0 & 0 \\ 0 & 0 & 0 \\ 0 & 0 & 0 \end{bmatrix}. \quad (3.28)$$

The gravity force vector can be expanded to (Fossen, 2011)

$$\mathbf{g}(\boldsymbol{\eta}_3) = mg \begin{bmatrix} \sin(\theta) \\ -\cos(\theta) \sin(\phi) \\ -\cos(\theta) \cos(\phi) \\ -y_g \cos(\theta) \cos(\phi) + z_g \cos(\theta) \sin(\phi) \\ z_g \sin(\phi) + x_g \cos(\theta) \cos(\phi) \\ -x_g \cos(\theta) \sin(\phi) - y_g \sin(\phi) \end{bmatrix}, \quad (3.29)$$

and linearization gives

$$\frac{\partial}{\partial \eta_3} \left(g(\eta_3^*) \right) \eta_3 = \mathbf{G}^* \eta_3, \quad (3.30)$$

where

$$\mathbf{G}^* := g \begin{bmatrix} 0 & 0 & m \\ 0 & -m & 0 \\ 0 & 0 & 0 \\ 0 & z_g m & 0 \\ 0 & 0 & z_g m \\ 0 & -x_g m & -y_g m \end{bmatrix}. \quad (3.31)$$

Similary as for \mathbf{C}_{RB}^* , we can express \mathbf{G}^* as a function of \mathbf{M}_{RB}

$$\mathbf{G}^* = \mathbf{M}_{RB} \mathbf{L}_g g, \quad (3.32)$$

where \mathbf{L}_g is a selection matrix defined as

$$\mathbf{L}_g = \begin{bmatrix} 0 & 0 & 1 \\ 0 & -1 & 0 \\ 0 & 0 & 0 \\ 0 & 0 & 0 \\ 0 & 0 & 0 \\ 0 & 0 & 0 \end{bmatrix}. \quad (3.33)$$

Now, we can rewrite (3.34) as

$$\begin{aligned} \dot{\nu}_3 &= \mathbf{L}_3 \mathbf{M}_{RB}^{-1} \left[-\mathbf{C}_{RB}^* \nu_3 - \mathbf{G}^* \eta_3 + \frac{\partial \tau_c(\nu_3^*, \delta^*)}{\partial \nu_3} \nu_3 + \frac{\partial \tau_c(\nu_3^*, \delta^*)}{\partial \delta} \delta \right] \\ &= -U_0 \mathbf{L}_3 \mathbf{L}_c \nu_3 - g \mathbf{L}_3 \mathbf{L}_g \eta_3 + \mathbf{L}_3 \mathbf{M}_{RB}^{-1} \left[\frac{\partial \tau_c(\nu_3^*, \delta^*)}{\partial \nu_3} \nu_3 + \frac{\partial \tau_c(\nu_3^*, \delta^*)}{\partial \delta} \delta \right]. \end{aligned} \quad (3.34)$$

Linearization of the last two terms is more extensive and will be handled in the following subsections.

3.1.3 Linearized Foil Forces due to Motions of the Craft

From Section 2.2 we find that the foils' lift and drag forces (F_L and F_D) depends on both the water's inflow speed V_∞ and direction α_∞ . Further, (2.44) gives that the transformation of F_L and F_D into the local foil frame, and hence also the craft's body frame, depends on α_∞ . We will now show how the velocity components of ν_3 affects V_∞ and α_∞ for an arbitrarily lifting foil, and how the body-frame forces $\Delta \tau_c$ for that foil can be linearized with respect to ν_3 . Finally, the linearized terms of all four foils will be summarized in order to find the total force. When deriving these linear terms, we assume calm water,

such that V_∞ and α_∞ only depends on the motions of the craft.

Since each local foil frame is constantly fixed with respect to the CO, we can start by linearizing the foil forces expressed in the foil frame. Applying (2.44), we find these forces to be

$$\mathbf{f}^f = \begin{bmatrix} f_x^f \\ f_y^f \\ f_z^f \end{bmatrix} = \begin{bmatrix} -F_D \cos(\alpha_\infty) + F_L \sin(\alpha_\infty) \\ 0 \\ -F_D \sin(\alpha_\infty) - F_L \cos(\alpha_\infty) \end{bmatrix}. \quad (3.35)$$

Partial differentiation with respect to ν_3 yields:

$$\frac{\partial \mathbf{f}^f}{\partial \nu_3} = \begin{bmatrix} -\frac{\partial F_D}{\partial \nu_3} \cos(\alpha_\infty) + F_D \sin(\alpha_\infty) \frac{\partial \alpha_\infty}{\partial \nu_3} + \frac{\partial F_L}{\partial \nu_3} \sin(\alpha_\infty) + F_L \cos(\alpha_\infty) \frac{\partial \alpha_\infty}{\partial \nu_3} \\ 0 \\ -\frac{\partial F_D}{\partial \nu_3} \sin(\alpha_\infty) - F_D \cos(\alpha_\infty) \frac{\partial \alpha_\infty}{\partial \nu_3} - \frac{\partial F_L}{\partial \nu_3} \cos(\alpha_\infty) + F_L \sin(\alpha_\infty) \frac{\partial \alpha_\infty}{\partial \nu_3} \end{bmatrix} \quad (3.36)$$

From (3.36), we see that we have to express α_∞ , F_L , F_D , $\frac{\partial \alpha_\infty}{\partial \nu_3}$, $\frac{\partial F_L}{\partial \nu_3}$ and $\frac{\partial F_D}{\partial \nu_3}$ as functions of ν_3 , for then applying the trim conditions ν_3^* and δ^* in order to find $\frac{\partial \mathbf{f}(\nu_3^*, \delta^*)}{\partial \nu_3}$. This process will be divided into the following steps.

Step 1:

To find $\frac{\partial \alpha_\infty(\nu_3^*)}{\partial \nu_3}$ and $\alpha_\infty(\nu_3^*)$.

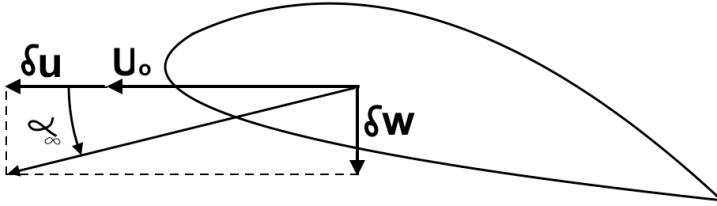


Figure 3.1: Change in inflow velocity due to change in the foil velocity

Figure 3.1 illustrates how the inflow angle α_∞ changes due to velocity perturbations δu and δw in the foil's x- and z-direction, respectively. The inflow angle becomes

$$\alpha_\infty = \tan^{-1} \left(\frac{\delta w}{U_0 + \delta u} \right). \quad (3.37)$$

Assuming δw small compared to $U_0 + \delta u$, an approximation for α_∞ is

$$\alpha_\infty \approx \frac{\delta w}{U_0 + \delta u}. \quad (3.38)$$

δu and δw can be expressed as functions of the components ν_3 , which are w , p and q . Let x , y and z denote the body-frame position of the foil, satisfying $\mathbf{r}_f^b = [x, y, z]^\top$ according to definition of \mathbf{r}_f in Section 2.2. From (2.27) or (2.28), we find:

$$\delta u = qz \quad (3.39)$$

$$\delta w = w + py - qx \quad (3.40)$$

Inserted into (3.38):

$$\alpha_\infty \approx \frac{w + py - qx}{U_0 + qz} \quad (3.41)$$

Now, we have an expression for α_∞ which can be used to find its partial derivative with respect to ν_3 :

$$\frac{\partial \alpha_\infty}{\partial \nu_3} = \left[\frac{\partial \alpha_\infty}{\partial w} \quad \frac{\partial \alpha_\infty}{\partial p} \quad \frac{\partial \alpha_\infty}{\partial q} \right] = \left[\frac{1}{U_0 + qz} \quad \frac{y}{U_0 + qz} \quad \frac{-x(U_0 + qz) - z(w + py - qx)}{(U_0 + qz)^2} \right] \quad (3.42)$$

For the trim condition $\nu_3 = \nu_3^*$, it becomes:

$$\frac{\partial \alpha_\infty(\nu_3^*)}{\partial \nu_3} = \left[\frac{1}{U_0} \quad \frac{y}{U_0} \quad -\frac{x}{U_0} \right] \quad (3.43)$$

It is also clear that for the trim condition, the inflow angle becomes zero:

$$\alpha_\infty(\nu_3^*) = 0 \quad (3.44)$$

Step 2:

To find $\frac{\partial F_L(\nu_3^*, \delta^*)}{\partial \nu_3}$ and $F_L(\nu_3^*, \delta^*)$.

From (2.31) in Section 2.2, we have

$$F_L = \frac{1}{2} \rho V_\infty^2 S C_L(\alpha_r).$$

Differentiation using the product rule gives

$$\frac{\partial F_L}{\partial \nu_3} = \frac{1}{2} \rho S \left(\frac{\partial (V_\infty^2)}{\partial \nu_3} C_L(\alpha_r) + V_\infty^2 \frac{\partial C_L(\alpha_r)}{\partial \nu_3} \right). \quad (3.45)$$

According to Figure 3.1, we can express V_∞^2 as a function of δu and δw :

$$V_\infty^2 = (U_0 + \delta u)^2 + (\delta w)^2 = (U_0 + qz)^2 + (w + py + qx)^2 \quad (3.46)$$

This gives

$$\begin{aligned} \frac{\partial (V_\infty^2)}{\partial \nu_3} &= \left[\frac{\partial (V_\infty^2)}{\partial w} \quad \frac{\partial (V_\infty^2)}{\partial p} \quad \frac{\partial (V_\infty^2)}{\partial q} \right] \\ &= \left[2(w + py - qx) \quad 2y(w + py - qx) \quad 2z(U_0 + qz) - 2x(w + py - qx) \right], \end{aligned} \quad (3.47)$$

such that

$$\frac{\partial(V_\infty^2(\boldsymbol{\nu}_3^*))}{\partial\boldsymbol{\nu}_3} = \begin{bmatrix} 0 & 0 & 2zU_0 \end{bmatrix}. \quad (3.48)$$

It also follows from (3.46) that

$$V_\infty^2(\boldsymbol{\nu}_3^*) = U_0^2. \quad (3.49)$$

We assume the total relative angle of attack to be such small that the linear term of the lift coefficient $C_L(\alpha_r)$ is dominating. Hence,

$$C_L(\alpha_r) = C_{L_{lin}}(\delta, \alpha_\infty) = C_{L_0} + C_{L_\alpha} \cdot (\delta + \alpha_\infty), \quad (3.50)$$

where C_{L_0} and C_{L_α} are as defined in (2.41) and (2.42), respectively. Partial differentiation with respect to $\boldsymbol{\nu}_3$ gives

$$\begin{aligned} \frac{\partial C_L(\alpha_r)}{\partial\boldsymbol{\nu}_3} &= \frac{\partial C_L(\alpha_r)}{\partial\alpha_\infty} \frac{\partial\alpha_\infty}{\partial\boldsymbol{\nu}_3} \\ &= C_{L_\alpha} \begin{bmatrix} \frac{1}{U_0+qz} & \frac{y}{U_0+qz} & \frac{-x(U_0+qz)-z(w+py-qx)}{(U_0+qz)^2} \end{bmatrix}, \end{aligned} \quad (3.51)$$

such that

$$\frac{\partial C_L(\boldsymbol{\nu}_3^*)}{\partial\boldsymbol{\nu}_3} = C_{L_\alpha} \frac{1}{U_0} \begin{bmatrix} 1 & y & -x \end{bmatrix}. \quad (3.52)$$

It also follows from (3.50) that

$$C_L(\boldsymbol{\nu}_3^*, \boldsymbol{\delta}^*) = C_{L_0}. \quad (3.53)$$

Now, we have linearized all four expressions inside the parentheses in (3.63), about $(\boldsymbol{\nu}_3^*, \boldsymbol{\delta}^*)$. When put together,

$$\frac{\partial F_L(\boldsymbol{\nu}_3^*)}{\partial\boldsymbol{\nu}_3} = \frac{1}{2}\rho S U_0 \begin{bmatrix} C_{L_\alpha} & yC_{L_\alpha} & 2zC_{L_0} - xC_{L_\alpha} \end{bmatrix}. \quad (3.54)$$

In order to find $F_L(\boldsymbol{\nu}_3^*, \boldsymbol{\delta}^*)$, we combine (2.31), (3.49) and (3.53):

$$F_L(\boldsymbol{\nu}_3^*, \boldsymbol{\delta}^*) = \frac{1}{2}\rho U_0^2 S C_{L_0} \quad (3.55)$$

Step 3:

To find $\frac{\partial F_D(\boldsymbol{\nu}_3^*, \boldsymbol{\delta}^*)}{\partial\boldsymbol{\nu}_3}$ and $F_D(\boldsymbol{\nu}_3^*, \boldsymbol{\delta})$.

From (2.32) in Section 2.2, we have

$$F_D = \frac{1}{2}\rho V_\infty^2 S C_D(\alpha_r).$$

Differentiation using the product rule gives

$$\frac{\partial F_L}{\partial \nu_3} = \frac{1}{2} \rho S \left(\frac{\partial(V_\infty^2)}{\partial \nu_3} C_D(\alpha_r) + V_\infty^2 \frac{\partial C_D(\alpha_r)}{\partial \nu_3} \right). \quad (3.56)$$

From (2.43) we have that

$$C_D(\alpha_r) = \frac{C_{L_{lin}}(\delta, \alpha_\infty)^2}{\pi e A R}, \quad (3.57)$$

when we assumes $C_L = C_{L_{lin}}$ and the plastic drag C_{D_p} to be zero. This gives

$$C_D(\nu_3^*, \delta^*) = \frac{C_{L_0}^2}{\pi e A R} \quad (3.58)$$

and

$$\frac{\partial C_D(\alpha_r)}{\partial \nu_3} = \frac{\partial C_D(\alpha_r)}{\partial C_{L_{lin}}(\alpha_r)} \frac{\partial C_{L_{lin}}(\alpha_r)}{\partial \nu_3} = \frac{2C_{L_{lin}}(\alpha_r)}{\pi e A R} \frac{\partial C_{L_{lin}}(\alpha_r)}{\partial \nu_3}, \quad (3.59)$$

such that

$$\frac{\partial C_D(\nu_3^*, \delta^*)}{\partial \nu_3} = \frac{2C_{L_0}}{\pi e A R} C_{L_\alpha} \frac{1}{U_0} \begin{bmatrix} 1 & y & -x \end{bmatrix}. \quad (3.60)$$

To simplify, we define

$$C_{D_\alpha} := \frac{2C_{L_0}}{\pi e A R} C_{L_\alpha} \quad (3.61)$$

and

$$C_{D_0} := \frac{C_{L_0}^2}{\pi e A R}. \quad (3.62)$$

Reusing the expressions for $\frac{\partial(V_\infty^2(\nu_3^*, \delta^*))}{\partial \nu_3}$ and $V_\infty^2(\nu_3^*, \delta^*)$ derived in Step 2, we get

$$\frac{\partial F_D(\nu_3^*, \delta^*)}{\partial \nu_3} = \frac{1}{2} \rho S U_0 \begin{bmatrix} C_{D_\alpha} & y C_{D_\alpha} & 2z C_{D_0} - x C_{D_\alpha} \end{bmatrix}. \quad (3.63)$$

In order to find $F_D(\nu_3^*, \delta^*)$, we combine (2.32), (3.49), (3.58) and (3.62):

$$F_D(\nu_3^*, \delta^*) = \frac{1}{2} \rho U_0^2 S C_{L_0} \quad (3.64)$$

Step 4:

Now, we can use (3.36) and the expressions derived in Step 1-3 to express $\frac{\partial \mathbf{f}^f(\nu_3^*, \delta^*)}{\partial \nu_3}$:

$$\frac{\partial \mathbf{f}^f(\nu_3^*, \delta^*)}{\partial \nu_3} = \frac{1}{2} \rho S U_0 \begin{bmatrix} (C_{L_0} - C_{D_\alpha}) & y(C_{L_0} - C_{D_\alpha}) & x(C_{D_\alpha} - C_{L_0}) - 2z C_{D_0} \\ 0 & 0 & 0 \\ -(C_{D_0} + C_{L_\alpha}) & -y(C_{D_0} + C_{L_\alpha}) & x(C_{D_0} + C_{L_\alpha}) - 2z C_{L_0} \end{bmatrix} \quad (3.65)$$

Then we define

$$D_{\nu_3}^f = -\frac{\partial \mathbf{f}^f(\nu_3^*, \delta^*)}{\partial \nu_3}, \quad (3.66)$$

such that the linearization of \mathbf{f}^f with respect to ν_3 can be expressed as

$$\mathbf{f}_{\nu_3}^f = -D_{\nu_3}^f \nu_3. \quad (3.67)$$

Step 5:

To express the linearized force in body frame, we apply (2.45) from Section 2.2, which can be rewritten as

$$\Delta \tau_{c,foil} = \begin{bmatrix} \mathbf{I}_{3 \times 3} \\ \mathbf{S}(\mathbf{r}_f^b) \end{bmatrix} \mathbf{f}^f. \quad (3.68)$$

Combining (3.67) and (3.68), the linearized force contribution expressed in body frame becomes

$$\Delta \tau_{foil}^{\nu_3} = -\begin{bmatrix} \mathbf{I}_{3 \times 3} \\ \mathbf{S}(\mathbf{r}_f^b) \end{bmatrix} D_{\nu_3}^f \nu_3 =: -D_{\nu_3}^b \nu_3. \quad (3.69)$$

Here, we have defined

$$D_{\nu_3}^b = \begin{bmatrix} \mathbf{I}_{3 \times 3} \\ \mathbf{S}(\mathbf{r}_f^b) \end{bmatrix} D_{\nu_3}^f, \quad (3.70)$$

which can be expanded to

$$D_{\nu_3}^b = -\frac{1}{2} \rho S U_0 \begin{bmatrix} C_{L_0} - C_{D_0} & y(C_{L_0} - C_{D_0}) & x(C_{D_0} - C_{L_0}) - 2zC_{D_0} \\ 0 & 0 & 0 \\ -(C_{D_0} + C_{L_0}) & -y(C_{D_0} + C_{L_0}) & x(C_{D_0} + C_{L_0}) - 2zC_{L_0} \\ -y(C_{D_0} + C_{L_0}) & -y^2(C_{D_0} + C_{L_0}) & xy(C_{D_0} + C_{L_0}) - 2yzC_{L_0} \\ z(C_{L_0} - C_{D_0}) + x(C_{D_0} + C_{L_0}) & yz(C_{L_0} - C_{D_0}) + xy(C_{D_0} + C_{L_0}) & xz(C_{L_0} - C_{D_0}) - 2z^2C_{D_0} - x^2(C_{D_0} + C_{L_0}) + 2xzC_{L_0} \\ -xy(C_{L_0} - C_{D_0}) & -y^2(C_{L_0} - C_{D_0}) & -xy(C_{L_0} - C_{D_0}) + 2yzC_{D_0} \end{bmatrix}. \quad (3.71)$$

Total Force

Since the craft has four lifting foils, the total linearized force due to motions of the craft becomes

$$\tau_{foil}^{\nu_3} = \sum_{i=1}^4 \Delta \tau_{foil,i}^{\nu_3} = -\sum_{i=1}^4 D_{\nu_3,i}^b \nu_3, \quad (3.72)$$

where i denotes the index of the foils, defined in an arbitrarily order. Finally, we define the total linearization matrix D representing all the four foils:

$$D = \sum_{i=1}^4 D_{\nu_3,i}^b \quad (3.73)$$

The term to insert in the linearized equation for $\dot{\nu}_3$ becomes

$$L_3 M_{RB}^{-1} \frac{\partial \tau_c(\nu_3^*, \delta^*)}{\partial \nu_3} \nu_3 = -L_3 M_{RB}^{-1} D \nu_3.$$

It can be shown that the diagonal numerical values for $\mathbf{L}_3 \mathbf{M}_{RB}^{-1} \mathbf{D}$ are positive, which means that the linearized forces and moments are acting in the opposite direction as the motion in the corresponding DOF and can therefore be considered as damping forces. Hence, the notation \mathbf{D} is used.

3.1.4 Linearized Control Force

The last term in 3.34 gives linearization with respect to the input δ . In order to derive an expression, we start by linearizing the lift and drag coefficients for an arbitrarily foil, with respect to its angular deviation δ . Assuming the linear part of the lift coefficient in (2.35) is dominating, we get

$$\frac{\partial C_L(\alpha^*)}{\partial \delta} = \frac{\partial C_{L_{lin}}(\alpha^*)}{\partial \delta} = C_{L_\alpha}. \quad (3.74)$$

For the drag coefficient, we apply the chain rule on the definition in (2.43), and get

$$\frac{\partial C_D(\alpha^*)}{\partial \delta} = \frac{\partial C_D(\alpha^*)}{\partial C_L} \frac{\partial C_L(\alpha^*)}{\partial \delta} = \frac{2C_{L_0}}{\pi e AR} C_{L_\alpha} = C_{D_\alpha}, \quad (3.75)$$

where α^* , as defined in Section 2.2, is the angle of attack when $\delta = \alpha_\infty = 0$, i.e. in trim conditions and mean inflow angle. Linearized lift and drag forces for $\boldsymbol{\eta}_3 = \boldsymbol{\eta}_3^*$ and $\boldsymbol{\nu}_3 = \boldsymbol{\nu}_3^*$ becomes:

$$\bar{F}_L = \frac{1}{2} \rho S U_0^2 C_{L_\alpha} \delta \quad (3.76)$$

$$\bar{F}_D = \frac{1}{2} \rho S U_0^2 C_{D_\alpha} \delta \quad (3.77)$$

Using the linearized expressions for lift and drag forces, we obtain the following body-frame force vector:

$$\frac{\partial \boldsymbol{\tau}_c(\boldsymbol{\nu}^*, \boldsymbol{\delta}^*)}{\partial \boldsymbol{\delta}} \boldsymbol{\delta} = \frac{1}{2} \rho S U_0^2 \begin{bmatrix} -C_{D_\alpha}(\delta_{FL} + \delta_{FR} + \delta_{AL} + \delta_{AR}) \\ 0 \\ -C_{L_\alpha}(\delta_{FL} + \delta_{FR} + \delta_{AL} + \delta_{AR}) \\ C_{L_\alpha}(\delta_{FL} - \delta_{FR} + \delta_{AL} - \delta_{AR}) y_{foil} \\ C_{L_\alpha}(\delta_{FL} + \delta_{FR} - \delta_{AL} - \delta_{AR}) x_{foil} \\ C_{D_\alpha}(-\delta_{FL} + \delta_{FR} - \delta_{AL} + \delta_{AR}) y_{foil} \end{bmatrix} \quad (3.78)$$

Due to geometrical symmetry, we have simplified by using x_{foil} , y_{foil} and z_{foil} as the absolute values of the x-, y- and z-positions, respectively, of the force-attack points for each foil.

Applying the configuration in (2.68), the linearized term can be expressed as a function of δ :

$$\frac{\partial \tau_c(\boldsymbol{\nu}^*, \boldsymbol{\delta}^*)}{\partial \boldsymbol{\delta}} \boldsymbol{\delta} = \frac{1}{2} \rho S U_0^2 \begin{bmatrix} -4C_{D_\alpha} \delta_z \\ 0 \\ -4C_{L_\alpha} \delta_z \\ 4C_{L_\alpha} y_{foil} \delta_a \\ 4C_{L_\alpha} x_{foil} \delta_e - 4C_{D_\alpha} z_{foil} \delta_z \\ -4C_{D_\alpha} y_{foil} \delta_a \end{bmatrix} = \mathbf{B}_\tau \boldsymbol{\delta}, \quad (3.79)$$

where

$$\mathbf{B}_\tau := 2\rho S U_0^2 \begin{bmatrix} 0 & 0 & -C_{D_\alpha} \\ 0 & 0 & 0 \\ 0 & 0 & -C_{L_\alpha} \\ C_{L_\alpha} y_{foil} & 0 & 0 \\ 0 & C_{L_\alpha} x_{foil} & C_{D_\alpha} z_{foil} \\ C_{D_\alpha} y_{foil} & 0 & 0 \end{bmatrix} \quad (3.80)$$

The term to insert in the linearized equation for $\dot{\boldsymbol{\nu}}_3$ becomes

$$\mathbf{L}_3 \mathbf{M}_{RB}^{-1} \frac{\partial \tau_c(\boldsymbol{\nu}_3^*, \boldsymbol{\delta}^*)}{\partial \boldsymbol{\delta}} \boldsymbol{\delta} = \mathbf{L}_3 \mathbf{M}_{RB}^{-1} \mathbf{B}_\tau \boldsymbol{\delta}.$$

3.2 State-Space Model

The linearized rigid-body dynamics and foil forces derived in Section 3.1 will be put into a *state-space model*, which also will include the actuator dynamics defined in the end of Section 2.4.

The actuator dynamics of each foil is modelled by the first order transfer function given in (2.69):

$$\frac{\delta}{\delta^c}(s) = \frac{1}{T_\delta s + 1}$$

A realization in the time domain becomes:

$$\dot{\delta} = -\frac{1}{T_\delta} \delta + \frac{1}{T_\delta} \delta^c \quad (3.81)$$

Since the control inputs δ_a , δ_e and δ_z are defined as linear combinations of the controlled deviations in the foil angles, and $T_\delta = 1/20$ s for all foils, we can apply the transfer function to the control inputs instead of the foil angles directly. For $\boldsymbol{\delta}^c := [\delta_a^c, \delta_e^c, \delta_z^c]^\top$ being the vector of commanded control inputs, and $\boldsymbol{\delta} = [\delta_a, \delta_e, \delta_z]^\top$ as defined in (3.3), the multivariable dynamics becomes:

$$\dot{\boldsymbol{\delta}} = -\frac{1}{T_\delta} \boldsymbol{\delta} + \frac{1}{T_\delta} \boldsymbol{\delta}^c \quad (3.82)$$

Later, we will also refer to δ_a , δ_e and δ_a as *generalized* deviations in foil angles.

For the total state-space model, we define the state vector

$$\mathbf{x} = \begin{bmatrix} \delta \\ \bar{\eta}_3 \\ \nu_3 \end{bmatrix}. \quad (3.83)$$

Also, let $\mathbf{u} = \delta^c$ be the commanded input from the controller, \mathbf{d} , be a vector of colored noise representing system disturbances from waves, and \mathbf{v} be a vector of zero-mean, white Gaussian sensor noise.

The state-space model describing both the linearized rigid-body dynamics and foil forces, as well as the linear actuator dynamics, becomes:

$$\dot{\mathbf{x}} = \mathbf{A}\mathbf{x} + \mathbf{B}\mathbf{u} + \mathbf{L}\mathbf{d} \quad (3.84)$$

$$\mathbf{y} = \mathbf{C}\mathbf{x} + \mathbf{v}, \quad (3.85)$$

where

$$\mathbf{A} = \begin{bmatrix} -\frac{1}{T_\delta} \mathbf{I}_{3 \times 3} & \mathbf{0}_{3 \times 3} & \mathbf{0}_{3 \times 3} \\ \mathbf{0}_{3 \times 3} & \mathbf{A}_{\eta_3} & \mathbf{I}_{3 \times 3} \\ L_3 \mathbf{M}_{RB}^{-1} \mathbf{B}_\tau & -g L_3 \mathbf{L}_g & -L_3 (L_c U_0 + \mathbf{M}_{RB}^{-1} \mathbf{D}) \end{bmatrix}, \quad (3.86)$$

$$\mathbf{B} = \begin{bmatrix} \frac{1}{T_\delta} \mathbf{I}_{3 \times 3} \\ \mathbf{0}_{9 \times 3} \end{bmatrix}, \quad (3.87)$$

$$\mathbf{L} = \begin{bmatrix} \mathbf{0}_{6 \times 3} \\ L_3 \mathbf{M}_{RB}^{-1} \mathbf{B}_\tau \end{bmatrix} \quad (3.88)$$

and

$$\mathbf{C} = [\mathbf{0}_{6 \times 6} \quad \mathbf{I}_{6 \times 6}]. \quad (3.89)$$

Remark that we in the disturbance matrix \mathbf{L} has chosen to use the relation from deviations in foil angles to body-frame acceleration. This because the wave impact modelled in this study is mainly due to changes in the angles of attack (see Section 2.2 and 2.5, and Kim and Yamato (2004)), so now the disturbance vector \mathbf{d} can be considered as changes in the foil angles, in the same frequency domain as the velocity components of the water particles. Hence, we are one step closer to meet the suggestion from Kim and Yamato (2004) of having a linear model where the disturbances are based on the wave orbital motions. Numerical values for the matrices \mathbf{A} , \mathbf{B} , \mathbf{L} and \mathbf{C} are given in Appendix A.

Chapter 4

Controller Design and Maneuvering

4.1 Frequency Weighting

Frequency weighting is applied in order to satisfy our design criteria for the \mathcal{H}_2 -optimized feedback controller, as well as taking the expected frequency distribution of disturbances into account. In order to do so, we design an augmented plant containing the linearized state-space model from previous chapter, and dynamics that are implementing the desired frequency weighting. The \mathcal{H}_2 controller will in the end be designed based on the state-space for this augmented plant.

The augmented plant with frequency weighting is illustrated with a block diagram in Figure 4.1. The matrices \mathbf{A} , \mathbf{B} , \mathbf{C} and \mathbf{L} represents linearized craft model derived in previous chapter, and $\mathbf{K}(s)$ is the dynamic feedback compensator we are going to design. $\mathbf{y}_d \in \mathbb{R}^6$ is the vector containing reference values for the measured states, i.e. desired positions and velocities in heave, roll and pitch. $\mathbf{y}_p \in \mathbb{R}^6$ is the vector containing the measured states, before the measurement noise is added. $\mathbf{y}_e \in \mathbb{R}^6$ is the vector containing noise-contaminated state errors for the measurable states. $\mathbf{w}_1 \in \mathbb{R}^3$ and $\mathbf{w}_2 \in \mathbb{R}^6$ are zero-mean, unit-intensity white-noise vectors, and $\mathbf{z}_1 \in \mathbb{R}^6$ and $\mathbf{z}_2 \in \mathbb{R}^3$ are vector containing performance signals for state errors and control inputs, respectively. $\mathbf{W}_y(s)$, $\mathbf{W}_u(s)$ and $\mathbf{W}_v(s)$ are dynamic frequency-weighting transfer matrices, which will be designed in the following subsections. $\mathbf{W}_v = A_v \mathbf{I}_{6 \times 6}$ is a constant, diagonal gain matrix for the sensor noise. Since the sensor noise is white, i.e. equally distributed over all frequencies, no frequency weighting is necessary. In the process of tuning the augmented plant (in order to achieve the desired feedback compensator), we found that $A_v = 1000$ is a suitable gain in order to minimize the sensor-noise impact.

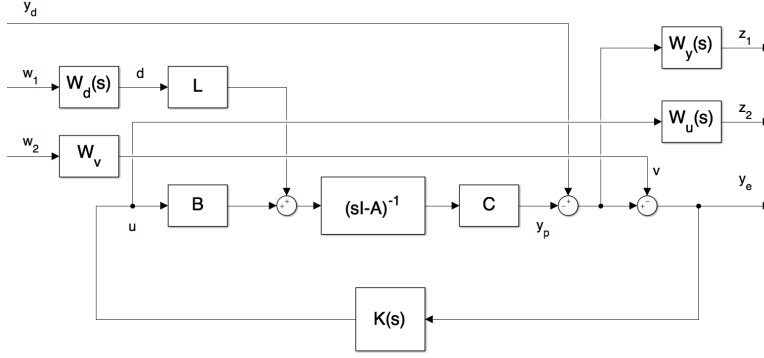


Figure 4.1: Block diagram of the frequency weighted plant

4.1.1 Weighted Output

The RCS is supposed to damp the wave induced motions, as well as keeping the craft stable in an upright position according to the reference signal. Errors due to high-frequency unmodelled dynamics (e.g. vibrations in materials) and sensor noise shall not be considered by the controller, so we want a performance signal z_1 that equals the low-pass filtered error, y_e . We choose to use a first-order low-pass filter, which according to Sørensen (2013) has the transfer function

$$w_{LP}(s) = \frac{\omega_c}{s + \omega_c}, \quad (4.1)$$

where ω_c is the cut-off frequency. From the chosen frequency spectrum in Section 2.5.2, we find that the most of the wave energy is in components with frequency below 2.5 rad/s, so we define that this is the upper wave-frequency limit ω_{max} . However, since the craft is moving, we have to consider the *encounter frequency*, which according to Fossen (2011) is defined as

$$\omega_e = \left| \omega_0 - \frac{\omega_0^2}{g} U_0 \cos(\beta) \right|, \quad (4.2)$$

where ω_0 is the wave frequency and β is the heading between the craft's velocity and the wave propagation direction. If the craft moves in head sea, i.e. $\beta = 180^\circ$, with a forward speed of $U_0 = 17$ m/s, this gives a maximum encounter frequency of

$$\omega_{e,max} = \left| \omega_{max} - \frac{\omega_{max}^2}{g} U_0 \cos(180^\circ) \right| = 2.5 + \frac{2.5^2}{9.81} 17 = 13.33 \text{ rad/s}. \quad (4.3)$$

We define ω_y as the cut-off frequency for the low-pass filter. We could choose to set this equal to e.g. 14 rad/s for all the components of y_e , such that $\omega_y > \omega_{e,max}$. However, in the tuning process we found it better to use $\omega_y = 1$ rad/s. This because the the first-order low pass filter has such a wide transition region that $\omega_y = 14$ rad/s makes the controller penalizing high-frequency virtual state errors caused by the influence of sensor noise. The

scalar frequency-weighting function becomes

$$w_y(s) = \frac{\omega_y}{s + \omega_y}. \quad (4.4)$$

Figure 4.2 shows the singular-value plot of (4.4).

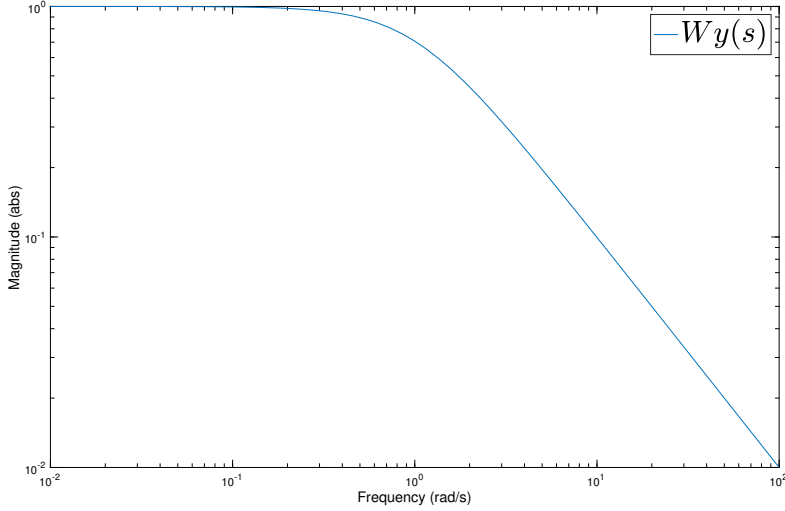


Figure 4.2: Weighting function for the output error

For all the 6 measured states, we define the transfer matrix

$$\mathbf{W}_y(s) = A_p w_y(s) \mathbf{I}_{6 \times 6}, \quad (4.5)$$

where we have included a *performance parameter*, A_p , which is supposed to be increased as much as possible without making the system unstable (Hassani et al., 2017). The performance vector \mathbf{z}_1 , which equals the frequency weighted errors multiplied by A_p becomes:

$$\mathbf{z}_1 = \mathbf{W}_y(s) \mathbf{y}_e \quad (4.6)$$

In the process of tuning the frequency weights, we found that A_p could be as high as 1000 without making the system unstable (no exact upper limit is determined). However, the sensor noise penetrated the controller, got amplified, and gave noisy control inputs not suitable for being applied on a real plant. We found $A_p = 10$ to be a good compromise giving satisfying performance and low noise penetration.

Realization in the time domain

We let y_e be an arbitrarily component of \mathbf{y}_e , and z_1 be the corresponding component of \mathbf{z}_1 . The transfer function in (4.4) can be rewritten as follows:

$$\begin{aligned}\frac{z_1}{y_e}(s) &= A_p \mathbf{w}_y(s) = A_p \frac{\omega_y}{s + \omega_y} \\ \Rightarrow sz_1 &= -\omega_y z_1 + A_p \omega_y y_e\end{aligned}\tag{4.7}$$

Then, a realization in the time domain gives the differential equation

$$\dot{z}_1 = -\omega_y z_1 + A_p \omega_y y_e.\tag{4.8}$$

For all the six states, we write

$$\dot{\mathbf{z}}_1 = \mathbf{A}_y \mathbf{z}_1 + \mathbf{B}_y \mathbf{y}_e = \mathbf{A}_y \mathbf{z}_1 - \mathbf{B}_y \mathbf{C} \mathbf{x} + \mathbf{B}_y \mathbf{y}_d,\tag{4.9}$$

where we have defined

$$\mathbf{A}_y = -\omega_y \mathbf{I}_{6 \times 6}, \quad \mathbf{B}_y = A_p \omega_y \mathbf{I}_{6 \times 6}.\tag{4.10}$$

4.1.2 Weighted Control

For the same reason as not penalizing high-frequency state errors, high-frequency control action can be penalized by letting the second performance signal \mathbf{z}_2 equal the high-pass filtered commanded control input \mathbf{u} . For all three control inputs we choose to use the following weighting function, which is a first order high-pass filter:

$$\mathbf{w}_u(s) = \frac{s + a}{s + \omega_u}\tag{4.11}$$

From (2.69) in Section 2.4, we see that the actuator dynamics can be considered as a low-pass filter with cut-off frequency $\omega_c = 1/T_\delta = 20$ rad/s. Hence, control signals varying with higher frequencies will not have any significant effect on the physical system, so we can choose $\omega_u = 20$ rad/s as the cut-off frequency for $\mathbf{w}_u(s)$. This also satisfies $\omega_u > \omega_y$, such that the control action is not strictly penalized inside the frequency range where we want to penalize state errors. We choose the parameter a to be 2 in order to keep a small penalty of $\mathbf{w}_u(s) > 0.1$ for low frequencies. This in order to keep the control inputs, and hence the deviations in foil angles, small enough to stay inside both physical limitations and the range where the assumption of linear forces holds. From Section 2.2, we have that the cut-off angle is $\alpha_0 = \pm 20^\circ$ for the blending function distinguishing linear and nonlinear lift coefficients. Accounting for some transition region, we should avoid foil angles greater than 15° or less than -15° . Therefore, a thumb rule will be to keep the control inputs, and hence the generalized deviations in foil angles, less than 5° and greater than -5° in order to avoid a single foil angle exceeding $\pm 15^\circ$. Figure 4.3 shows a singular-value plot of $\mathbf{w}_u(s)$.

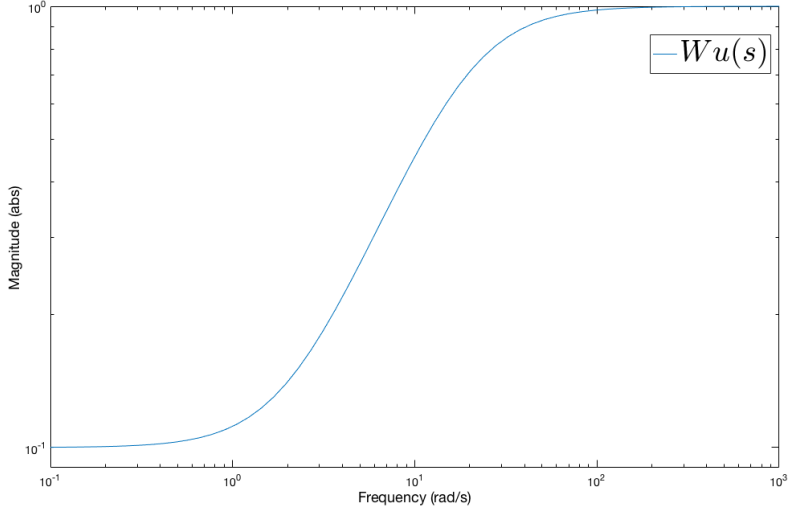


Figure 4.3: Weighting function for the control input

For all the three control inputs, the transfer matrix becomes

$$\mathbf{W}_u(s) = w_u(s)\mathbf{I}_{3 \times 3}, \quad (4.12)$$

such that

$$\mathbf{z}_2 = \mathbf{W}_u(s)\mathbf{u} \quad (4.13)$$

Realization in the time domain

We let u be an arbitrarily component of \mathbf{u} , and z_2 be the corresponding component of \mathbf{z}_2 . The transfer function in (4.11) can be rewritten as follows:

$$\begin{aligned} \frac{z_2}{u}(s) &= w_u(s) = \frac{s+a}{s+\omega_u} = \frac{s+a+\omega_u-\omega_u}{s+\omega_u} = 1 - \frac{\omega_u-a}{s+\omega_u} \\ \Rightarrow z_2 &= u - \frac{\omega_u-a}{s+\omega_u}u \end{aligned} \quad (4.14)$$

We see that z_2 equals u minus the low-pass filtered value of u , so we define a new variable for the low-pass filtered signal:

$$z_{2LP} = \frac{\omega_u-a}{s+\omega_u}u \quad (4.15)$$

This transfer function can be realized in the time domain in the same way as for $w_y(s)$. A realization of $w_u(s)$ can then be done by the following state-space model:

$$\begin{aligned}\dot{z}_{2LP} &= -\omega_u z_2 + (\omega_u - a)u \\ z_2 &= -z_{2LP} + u\end{aligned}\tag{4.16}$$

For all the three control inputs, we write

$$\begin{aligned}\dot{\mathbf{z}}_{2LP} &= \mathbf{A}_u \mathbf{z}_{2LP} + \mathbf{B}_u \mathbf{u} \\ \mathbf{z}_2 &= \mathbf{C}_u \mathbf{z}_{2LP} + \mathbf{D}_u \mathbf{u}\end{aligned}\tag{4.17}$$

where we have defined \mathbf{z}_{2LP} as the vector of z_{2LP} for all control inputs, and

$$\mathbf{A}_u = -\omega_u \mathbf{I}_{3 \times 3}, \quad \mathbf{B}_u = (\omega_u - a) \mathbf{I}_{3 \times 3}, \quad \mathbf{C}_u = -\mathbf{I}_{3 \times 3}, \quad \mathbf{D}_u = \mathbf{I}_{3 \times 3}\tag{4.18}$$

4.1.3 Weighted Plant Disturbance

The disturbance forces acting on the craft are dominated by the waves, so we let the controller be designed with respect to disturbances dominating in the range of expected encounter frequencies. We have already found an upper limit of $\omega_{e,max} = 13.33$ rad/s. According to (4.2), the encounter frequency can be as low as zero rad/s, if all wave components have the right frequency and angle relative to the heading of the craft. However, this is unlikely to happen in a realistic situation with short-crested irregular waves, so we can expect that the most of the wave induced disturbances are concentrated in a more narrow interval with a lower bound higher than zero. Hence, the disturbance weighting function can be modelled as a *band-pass filter*, which here will be a cascade of a first order low-pass filters with cut-off frequency ω_{dH} and a first order high-pass filter with cut-off frequency ω_{dL} :

$$w_d(s) = \frac{\omega_{dH}}{s + \omega_{dH}} \cdot \frac{s}{s + \omega_{dL}} = \frac{\omega_{dH} s}{s^2 + (\omega_{dH} + \omega_{dL})s + \omega_{dH} \omega_{dL}}\tag{4.19}$$

By performing simulations with the complete simulation model and controller in different wave conditions, we have found $\omega_{dL} = 0.2$ rad/s and $\omega_{dH} = 2$ rad/s to be suitable limits in order to achieve good disturbance rejection. It became less good for wider intervals. The singular-value plot of $w_d(s)$ is given in Figure 4.4. We also had to multiply $w_d(s)$ with a scaling gain $A_d = 1 \cdot 10^5$.

For disturbances in all the three DOF, the transfer matrix becomes

$$\mathbf{W}_d(s) = A_d w_d(s) \mathbf{I}_{3 \times 3},\tag{4.20}$$

such that

$$\mathbf{d} = \mathbf{W}_d(s) \mathbf{w}_1,\tag{4.21}$$

where \mathbf{w}_1 is a 3-element vector of white-noise signals.

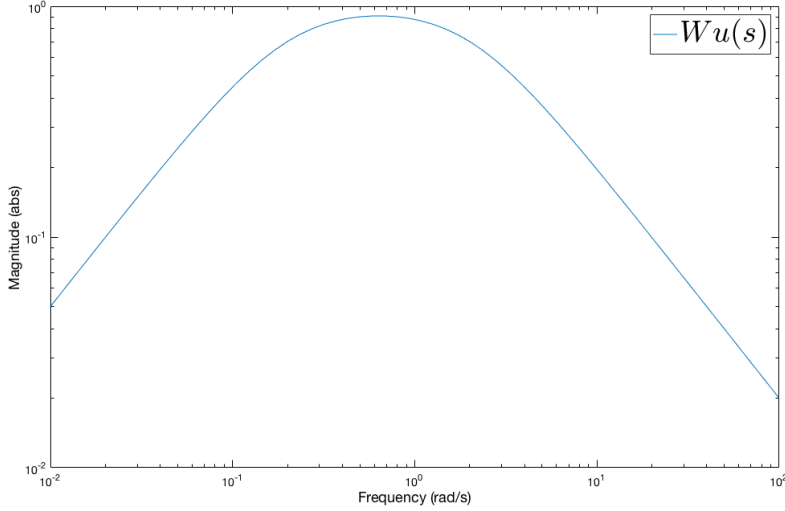


Figure 4.4: Weighting function for the disturbance input

Realization in the time domain

We let d be an arbitrarily component of \mathbf{d} , and w be the corresponding component of \mathbf{w}_1 . The transfer function in (4.19) can be rewritten as follows:

$$\begin{aligned} w_d(s) &= \frac{\omega_{d_H} s}{(s + \omega_{d_H})(s + \omega_{d_L})} = \frac{\omega_{d_H}(s + \omega_{d_H}) - \omega_{d_H}^2}{(s + \omega_{d_H})(s + \omega_{d_L})} \\ &= \frac{\omega_{d_H}}{s + \omega_{d_L}} - \frac{\omega_{d_H}^2}{(s + \omega_{d_H})(s + \omega_{d_L})} =: w_{d1}(s) + w_{d2}(s) \end{aligned} \quad (4.22)$$

Here we have split the transfer function into two terms denoted $w_{d1}(s)$ and $w_{d2}(s)$. Then, we can split the filtered signal d into the two parts

$$d_1 := A_d w_{d1}(s)w, \quad d_2 := A_d w_{d2}(s)w, \quad (4.23)$$

such that

$$d = A_d w_{d1}(s)w + A_d w_{d2}(s)w = d_1 + d_2. \quad (4.24)$$

First, we consider d_1 . From (4.23) we obtain

$$d_1 = A_d \frac{\omega_{d_H}}{s + \omega_{d_L}} w \Rightarrow s d_1 = -\omega_{d_L} d_1 + A_d \omega_{d_H} w. \quad (4.25)$$

Realized in the time domain, this gives the first order differential equation

$$\dot{d}_1 = -\omega_{d_L} d_1 + A_d \omega_{d_H} w. \quad (4.26)$$

Then, we consider d_2 . We have

$$w_{d2}(s) = \frac{-\omega_{d_H}^2}{(s + \omega_{d_H})(s + \omega_{d_L})} = \frac{-\omega_{d_H}^2}{s^2 + (\omega_{d_H} + \omega_{d_L})s + \omega_{d_H}\omega_{d_L}}. \quad (4.27)$$

From (4.23) we obtain

$$\begin{aligned} d_2 &= A_d \frac{-\omega_{d_H}^2}{s^2 + (\omega_{d_H} + \omega_{d_L})s + \omega_{d_H}\omega_{d_L}} w \\ \Rightarrow s^2 d_2 &= -(\omega_{d_H} + \omega_{d_L})s d_2 - \omega_{d_H}\omega_{d_L} d_2 - A_d \omega_{d_H}^2 w. \end{aligned} \quad (4.28)$$

Realized in the time domain, this gives the second order differential equation

$$\ddot{d}_2 = -(\omega_{d_H} + \omega_{d_L})\dot{d}_2 - \omega_{d_H}\omega_{d_L} d_2 - A_d \omega_{d_H}^2 w. \quad (4.29)$$

In order to augment this into the total frequency weighted state-space model, we have to rewrite it as a set of two first order differential equations. We define $d_{21} := \dot{d}_2$ and $d_{22} := \ddot{d}_2$. Hence,

$$\dot{d}_{21} = d_{22} \quad (4.30)$$

$$\dot{d}_{22} = -(\omega_{d_H} + \omega_{d_L})d_{22} - \omega_{d_H}\omega_{d_L} d_{21} - A_d \omega_{d_H}^2 w. \quad (4.31)$$

Now we have a set of three first order differential equations which in combination are relating each component of \mathbf{w}_1 to the corresponding component of \mathbf{d} . Considering disturbances in all three DOF, we have nine differential equations which can be arranged as a state-space model relating \mathbf{w}_1 to \mathbf{d} . We define $\mathbf{d}_1 \in \mathbb{R}^3$ as the vector containing d_1 for heave, roll and pitch, respectively. Similarly we define $\mathbf{d}_{21} \in \mathbb{R}^3$ and $\mathbf{d}_{22} \in \mathbb{R}^3$ as the vectors containing the heave roll and pitch components of d_{21} and d_{22} , respectively. The state-space model becomes

$$\begin{aligned} \underbrace{\begin{bmatrix} \dot{\mathbf{d}}_1 \\ \dot{\mathbf{d}}_{21} \\ \dot{\mathbf{d}}_{22} \end{bmatrix}}_{\mathbf{\dot{d}}_{\text{vec}}} &= \underbrace{\begin{bmatrix} \mathbf{A}_{d_1} & \mathbf{0}_{3 \times 3} & \mathbf{0}_{3 \times 3} \\ \mathbf{0}_{3 \times 3} & \mathbf{0}_{3 \times 3} & \mathbf{I}_{3 \times 3} \\ \mathbf{0}_{3 \times 3} & \boldsymbol{\Omega}_{d_2} & \boldsymbol{\Lambda}_{d_2} \end{bmatrix}}_{\mathbf{A}_d} \underbrace{\begin{bmatrix} \mathbf{d}_1 \\ \mathbf{d}_{21} \\ \mathbf{d}_{22} \end{bmatrix}}_{\mathbf{d}_{\text{vec}}} + \underbrace{\begin{bmatrix} \mathbf{B}_{d_1} \\ \mathbf{0}_{3 \times 3} \\ \mathbf{B}_{d_{22}} \end{bmatrix}}_{\mathbf{B}_d} \mathbf{w}_1 \\ \mathbf{d} &= \underbrace{\begin{bmatrix} \mathbf{I}_{3 \times 3} & \mathbf{I}_{3 \times 3} & \mathbf{0}_{3 \times 3} \end{bmatrix}}_{\mathbf{C}_d} \mathbf{d}_{\text{vec}}, \end{aligned} \quad (4.32)$$

where we have defined

$$\begin{aligned} \mathbf{A}_{d_1} &:= -\omega_{d_L} \mathbf{I}_{3 \times 3}, \quad \boldsymbol{\Omega}_{d_2} := -\omega_{d_H} \omega_{d_L} \mathbf{I}_{3 \times 3}, \quad \boldsymbol{\Lambda}_{d_2} := -(\omega_{d_H} + \omega_{d_L}) \mathbf{I}_{3 \times 3}, \\ \mathbf{B}_{d_1} &:= A_d \omega_{d_H} \mathbf{I}_{3 \times 3}, \quad \mathbf{B}_{d_{22}} := -A_d \omega_{d_H}^2 \mathbf{I}_{3 \times 3}. \end{aligned} \quad (4.33)$$

Using \mathbf{d}_{vec} , \mathbf{A}_d , \mathbf{B}_d and \mathbf{C}_d as defined by underbraces in (4.32), a more compact expression for the state-space model is

$$\begin{aligned} \dot{\mathbf{d}}_{\text{vec}} &= \mathbf{A}_d \mathbf{d}_{\text{vec}} + \mathbf{B}_d \mathbf{w}_1 \\ \mathbf{d} &= \mathbf{C}_d \mathbf{d}_{\text{vec}}. \end{aligned} \quad (4.34)$$

4.2 Augmented Plant and Weight Dynamics

With linear state-space models describing both the dynamics of the linearized plant and the weighting functions, everything can be augmented into one state-space model. We define the augmented state vector \mathbf{x}_{aug} :

$$\mathbf{x}_{aug} := \begin{bmatrix} \mathbf{x} \\ \mathbf{d}_{vec} \\ \mathbf{z}_1 \\ \mathbf{z}_{2LP} \end{bmatrix} \quad (4.35)$$

According to MathWorks Inc. (2017), the augmented input vector \mathbf{u}_{aug} has to contain the reference signal \mathbf{y}_d , the Gaussian white-noise vectors \mathbf{w}_1 and \mathbf{w}_2 , and the control input \mathbf{u} , in the respective order. Hence, we define

$$\mathbf{u}_{aug} := \begin{bmatrix} \mathbf{y}_d \\ \mathbf{w}_1 \\ \mathbf{w}_2 \\ \mathbf{u} \end{bmatrix}. \quad (4.36)$$

It is also required that the augmented output vector \mathbf{y}_{aug} contains the performance vectors \mathbf{z}_1 and \mathbf{z}_2 , and the error vector of measured states, \mathbf{y}_e , in the respective order. We define

$$\mathbf{y}_{aug} := \begin{bmatrix} \mathbf{z}_1 \\ \mathbf{z}_2 \\ \mathbf{y}_e \end{bmatrix}. \quad (4.37)$$

The frequency weighted plant dynamics, augmented according to the block diagram in Figure 4.1, becomes

$$\dot{\mathbf{x}}_{aug} = \mathbf{A}_{aug}\mathbf{x}_{aug} + \mathbf{B}_{aug}\mathbf{u}_{aug} \quad (4.38)$$

$$\mathbf{y}_{aug} = \mathbf{C}_{aug}\mathbf{x}_{aug} + \mathbf{D}_{aug}\mathbf{u}_{aug}, \quad (4.39)$$

where

$$\mathbf{A}_{aug} = \begin{bmatrix} \mathbf{A} & \mathbf{L}\mathbf{C}_d & \mathbf{0}_{12 \times 6} & \mathbf{0}_{12 \times 3} \\ \mathbf{0}_{9 \times 12} & \mathbf{A}_d & \mathbf{0}_{9 \times 6} & \mathbf{0}_{9 \times 3} \\ -\mathbf{B}_y\mathbf{C} & \mathbf{0}_{6 \times 9} & \mathbf{A}_y & \mathbf{0}_{6 \times 3} \\ \mathbf{0}_{3 \times 12} & \mathbf{0}_{3 \times 9} & \mathbf{0}_{3 \times 6} & \mathbf{B}_u \end{bmatrix} \quad (4.40)$$

$$\mathbf{B}_{aug} = \begin{bmatrix} \mathbf{0}_{12 \times 6} & \mathbf{0}_{12 \times 3} & \mathbf{B} \\ \mathbf{0}_{9 \times 6} & \mathbf{B}_d & \mathbf{0}_{9 \times 3} \\ \mathbf{B}_y & \mathbf{0}_{6 \times 3} & \mathbf{0}_{6 \times 3} \\ \mathbf{0}_{3 \times 6} & \mathbf{0}_{3 \times 3} & \mathbf{B}_u \end{bmatrix} \quad (4.41)$$

$$\mathbf{C}_{aug} = \begin{bmatrix} \mathbf{0}_{6 \times 12} & \mathbf{0}_{6 \times 9} & \mathbf{I}_{6 \times 6} & \mathbf{0}_{6 \times 3} \\ \mathbf{0}_{3 \times 12} & \mathbf{0}_{3 \times 9} & \mathbf{0}_{3 \times 6} & \mathbf{I}_{3 \times 3} \\ -\mathbf{C} & \mathbf{0}_{6 \times 9} & \mathbf{0}_{6 \times 6} & \mathbf{0}_{6 \times 3} \end{bmatrix} \quad (4.42)$$

$$\mathbf{D}_{aug} = \begin{bmatrix} \mathbf{0}_{6 \times 6} & \mathbf{0}_{6 \times 3} & \mathbf{0}_{6 \times 3} \\ \mathbf{0}_{3 \times 6} & \mathbf{0}_{3 \times 3} & \mathbf{I}_{3 \times 3} \\ \mathbf{I}_{6 \times 6} & \mathbf{0}_{6 \times 3} & -\mathbf{D} \end{bmatrix}. \quad (4.43)$$

4.3 \mathcal{H}_2 Controller

The `h2syn()` function in the Robust Control Toolbox in MATLAB is used in order to compute an \mathcal{H}_2 -optimal and frequency weighted controller for the augmented plant. With the `ss()` function in MATLAB, we create a state-space model \mathbf{P} for the augmented plant by using the numerical values of the matrices defined in (4.40) to (4.43). Then, the state-space model for the controller, here denoted by \mathbf{K} , is obtained by using the command

$$\mathbf{K} = \text{h2syn}(\mathbf{P}, \text{NMEAS}, \text{NCON}), \quad (4.44)$$

where $\text{NMEAS} = 6$ is the number of elements in \mathbf{y}_{aug} containing measured state errors being fed into the controller, and $\text{NCON} = 3$ is the number of elements in \mathbf{u}_{aug} containing input signals coming from the controller.

The controller can mathematically be presented as a state-space model with input \mathbf{y}_{aug} and output \mathbf{u}_{aug} :

$$\dot{\mathbf{x}}_c = \mathbf{A}_c\mathbf{x}_c + \mathbf{B}_c\mathbf{y}_e \quad (4.45)$$

$$\mathbf{u} = \mathbf{C}_c\mathbf{x}_c + \mathbf{D}_c\mathbf{y}_e \quad (4.46)$$

$\mathbf{A}_c \in \mathbb{R}^{27 \times 27}$, $\mathbf{B}_c \in \mathbb{R}^{27 \times 6}$, $\mathbf{C}_c \in \mathbb{R}^{3 \times 27}$ and $\mathbf{D}_c \in \mathbb{R}^{3 \times 6}$. Their numerical values are found by extracting the matrices stored in the state-space variable \mathbf{K} in MATLAB, and due to their large dimensionality, these are not provided in this report. The controller is implemented to the Simulink model as a state-space model with initial condition $\mathbf{x}_c(t_0) = \mathbf{0}$.

Combination of this dynamic controller and the linearized state-space model in (3.84) and (3.85), gives the following state-space model for the nominal closed-loop system:

$$\begin{bmatrix} \dot{\mathbf{x}} \\ \dot{\mathbf{x}}_c \end{bmatrix} = \begin{bmatrix} \mathbf{A} - \mathbf{B}\mathbf{D}_c\mathbf{C} & \mathbf{B}\mathbf{C}_c \\ -\mathbf{B}_c\mathbf{C} & \mathbf{A}_c \end{bmatrix} \begin{bmatrix} \mathbf{x} \\ \mathbf{x}_c \end{bmatrix} + \begin{bmatrix} \mathbf{B}\mathbf{D}_c & \mathbf{L} & -\mathbf{B}\mathbf{D}_c \\ \mathbf{B}_c & \mathbf{0} & -\mathbf{B}_c \end{bmatrix} \begin{bmatrix} \mathbf{y}_d \\ \mathbf{d} \\ \mathbf{v} \end{bmatrix} \quad (4.47)$$

$$\mathbf{y}_p = \begin{bmatrix} \mathbf{C} & \mathbf{0} \end{bmatrix} \begin{bmatrix} \mathbf{x} \\ \mathbf{x}_c \end{bmatrix} \quad (4.48)$$

Here, the reference values in \mathbf{y}_d , plant disturbances in \mathbf{d} , and sensor noise in \mathbf{v} are inputs, and the output \mathbf{y}_p is the vector containing the measurable states, not contaminated with any sensor noise. Figure 4.5 shows singular values for the closed-loop transfer functions relating generalized disturbance inputs in heave, roll and pitch to the corresponding states for position and velocity.

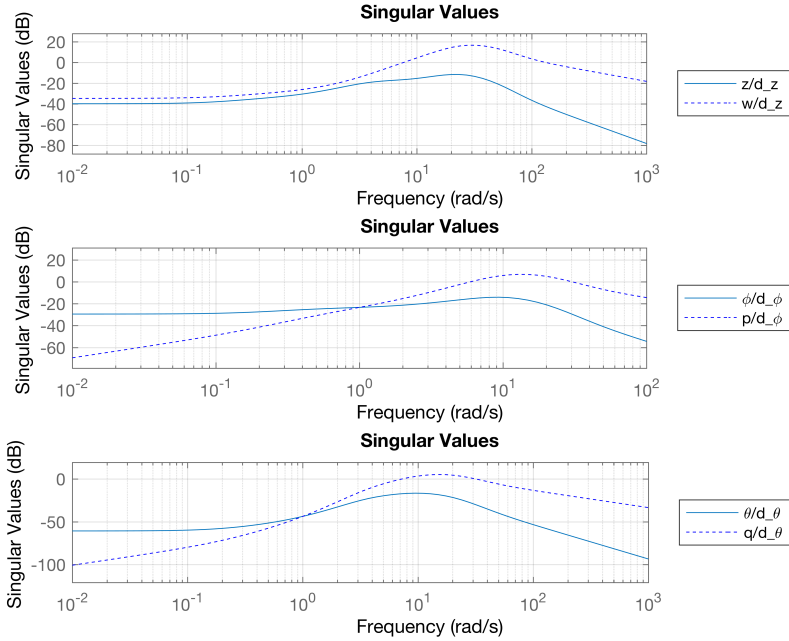


Figure 4.5: Singular values of closed-loop transfer functions from disturbance inputs in \mathbf{v} to position and velocity states in heave, roll and pitch

4.4 External Controllers

Since the simulation model has six DOF and the RCS only controls heave, roll and pitch, external controllers will be necessary to keep position and/or velocity in the remaining DOF constrained such that the assumptions applied when linearizing the model in Section 3 holds. This includes a *yaw-rate controller* using the rudders to keep the yaw rate r equal to zero, or a small value given as reference, and a *sideslip controller* keeping the sway velocity v to zero by adjusting the reference for ϕ . These controllers will also be essential in order to make the craft turn. They will be simple PID and PI controllers, respectively, and since the main objective of this study is to design and test the RCS in different conditions, we will not put in any big effort in making these controllers optimally tuned.

4.4.1 Yaw-rate Controller

Let r_d be the desired yaw rate. We define the error in yaw rate to be

$$r_e = r_d - r. \quad (4.49)$$

The control input for the rudders is then given by the following PID controller:

$$\delta_r^c(t) = k_{p_r} r_e(t) + k_{i_r} \int r_e(t) dt + k_{d_r} \dot{r}_e(t) \quad (4.50)$$

Recall from (2.69) that $\delta_r = \frac{20}{s+20} \delta_r^c$, and from (2.68) that

$$\begin{bmatrix} \delta_{FL}^r \\ \delta_{FR}^r \\ \delta_{AL}^r \\ \delta_{AR}^r \end{bmatrix} = \begin{bmatrix} 1 \\ 1 \\ -1 \\ -1 \end{bmatrix} \delta_r.$$

The controller gains are found from earlier work on a similar simulation model, done by Piene (2017):

$$k_{p_r} = 1.333, \quad k_{i_r} = 0.1, \quad k_{d_r} = 1.197 \quad (4.51)$$

4.4.2 Sideslip Controller

A roll angle ϕ different from zero will cause a sideways force acting on the craft. This because the lifting forces acting on the foils then will have a component in horizontal direction. Depending on environmental forces and centrifugal force from turning, the craft will experience a sway velocity different from zero. In the aircraft terminology this is called *sideslip*, and is measured by the angle $\beta := \sin^{-1}(v/\sqrt{u^2 + v^2 + w^2})$ (Beard and McLain, 2011). This sideslip can on the hydrofoil craft be controlled to zero by adjusting

the roll angle ϕ . In section 3.1.2, we linearized the kinetics for all 6 DOF, with respect to η_3 , ν_3 and δ , before extracting the kinetic equations for heave, roll and pitch with the selection matrix L_3 . Hence, we have the following differential equation relating the sway acceleration \dot{v} to the roll angle ϕ :

$$\dot{v} = g\phi + d_v, \quad (4.52)$$

where g is gravity acceleration, and d_v denotes the sum of terms not depending on ϕ . A transfer function relating v to ϕ becomes:

$$\frac{v}{\phi}(s) = \frac{1}{s}g \quad (4.53)$$

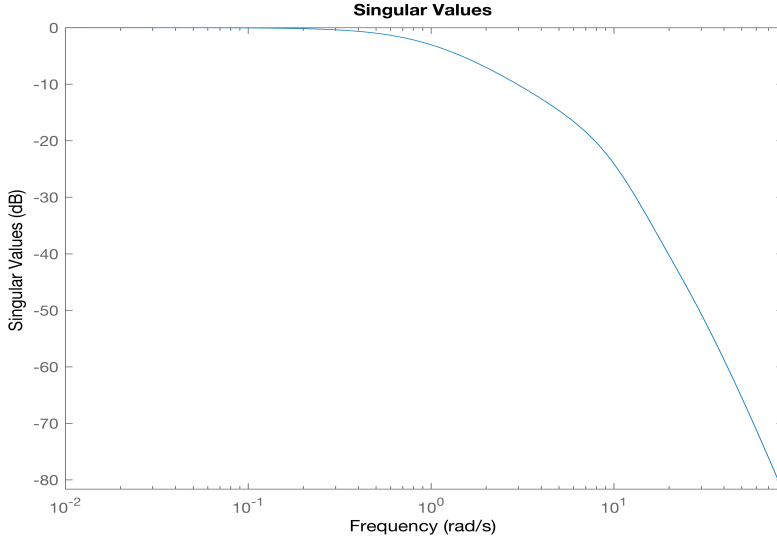


Figure 4.6: Singular values of $\phi/\phi_d(s)$

We will successively close an outer PI feedback loop around the RCS controlling ϕ . Figure 4.6 shows the singular-value plot of the transfer function $\frac{\phi}{\phi_d}(s)$, which is obtained from the nominal closed-loop system in (4.47) and (4.48). We see that roughly are $\frac{\phi}{\phi_d}(s) \approx 1$ for frequencies up to approximately 1 rad/s. Hence, for lower frequencies, the block diagram provided in Figure 4.7 is a good approximation of the successive loop closure. Here, v_d is the reference sway velocity, which in our case is supposed to equal zero, k_{p_v} is the proportional gain and k_{i_v} is integral gain. From the block diagram, we find that the transfer function from v_d to v becomes

$$\frac{v}{v_d}(s) = \frac{(k_{p_v} + \frac{1}{s}k_{i_v})\frac{g}{s}}{1 + (k_{p_v} + \frac{1}{s}k_{i_v})\frac{g}{s}} = \frac{k_{p_v}g(s + \frac{k_{i_v}}{k_{p_v}})}{s^2 + k_{p_v}gs + k_{i_v}g}. \quad (4.54)$$

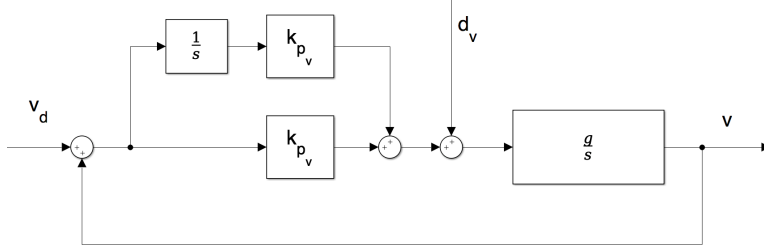


Figure 4.7: Outer feedback loop controlling sway velocity

This can be expressed in canonical form, using a suitable natural frequency ω_{n_v} and damping ratio ζ_v :

$$\frac{v}{v_d}(s) = \frac{2\zeta_v\omega_{n_v}s + \omega_{n_v}^2}{s^2 + 2\zeta_v\omega_{n_v}s + \omega_{n_v}^2} \quad (4.55)$$

Comparing coefficients in (4.54) and (4.55), we get

$$\omega_{n_v}^2 = k_{i_v}g \quad (4.56)$$

and

$$2\zeta_v\omega_{n_v} = k_{p_v}g. \quad (4.57)$$

Solving these equations with respect to k_{p_v} and k_{i_v} gives

$$k_{p_v} = \frac{2\zeta_v\omega_{n_v}}{g} \quad (4.58)$$

and

$$k_{i_v} = \frac{\omega_{n_v}^2}{g}. \quad (4.59)$$

From Figure 4.6 we see that we can pick $\omega_{n_v} = 0.5$ rad/s and still stay inside the interval where $\frac{\phi}{\phi_d}(s) \approx 1$ with an acceptable margin. By also choosing $\zeta_v = \sqrt{0.5} = 0.707$, we get the gains

$$k_{p_v} = 0.0721 \quad \text{and} \quad k_{i_v} = 0.0255. \quad (4.60)$$

Later tuning showed that these gains gave better performance than significantly higher and significantly lower values of ω_{n_v} .

4.4.3 Surge Speed Controller

Since both the foils and the rudders are experiencing drag forces in the body-frame's negative x-direction, this will slow down the surge speed of the craft until it stops, unless a thrust force is compensating. A change in the surge speed will also have an impact on the behavior of the lifting foils and the rudders. As described in Section 2.2 and 2.3, the lift and drag forces depends on the surge speed of the craft. It is important to keep a constant

surge speed of $u = U_0$, since the linearized model and the RCS are designed based on this as an assumption.

In order to keep the surge speed constant, the model has implemented a virtual thrust force \mathbf{u}_{thrust} acting in body-frame's positive x-direction, with point of attack in $(0, 0, 4)$ - which equals the same z-position as the origin of the lifting foils (see Table 2.1). Hence, \mathbf{u}_{thrust} will also compensate for the negative pitch moment caused by the drag forces acting on the foils. The body-fixed force vector acting on the craft's CO becomes

$$\boldsymbol{\tau}_{thrust} = [\mathbf{u}_{thrust} \quad 0 \quad 0 \quad 0 \quad 4 \cdot \mathbf{u}_{thrust} \quad 0]^\top. \quad (4.61)$$

\mathbf{u}_{thrust} is controlled by a simple PID controller, satisfying the formula

$$\mathbf{u}_{thrust}(t) = k_{p_u} u_e(t) + k_{i_u} \int u_e(t) dt + k_{d_u} \dot{u}_e(t), \quad (4.62)$$

where $u_e(t) = U_{ref} - u(t)$ is the error in surge speed from a desired value U_{ref} . The constants k_{p_u} , k_{i_u} and k_{d_u} are manually tuned as follows:

$$k_{p_u} = 93320, \quad k_{i_u} = 4000, \quad k_{d_u} = 80000 \quad (4.63)$$

4.5 Maneuvering

A simple maneuvering system making the craft able to perform *coordinated turns* will be implemented. During a coordinated turn, there will be no lateral acceleration in the body frame of the craft. This will increase the passenger comfort. The craft is tilted with a roll angle ϕ such that the centrifugal force acting on the craft counteracts the horizontal component of the lift force (Beard and McLain, 2011). The input will be a preferred turning radius R , measured in meters, commanded by e.g. a steering wheel or an autopilot.

We let F_{lift} denote the total lift force from the foils. The first condition we apply is that the vertical component F_{lift} shall be equal and opposite of the gravity force mg . Assuming the pitch θ is controlled to zero, this implies

$$F_{lift} \cos(\phi) = mg. \quad (4.64)$$

The second condition is that the horizontal component of F_{lift} equals the centripetal force making the craft turning with a radius R . If we let positive R denote turning radius when turning in clockwise direction, and use negative R for turns in counterclockwise direction, the condition becomes

$$F_{lift} \sin(\phi) \cos(\beta) = \frac{mU^2}{R}, \quad (4.65)$$

where $U = \sqrt{u^2 + v^2 + w^2}$ is the absolute speed of the craft (assumed to be in the horizontal plane), and β is a possible sideslip angle. Dividing (4.65) by (4.64) and solving with respect to $\tan(\phi)$, we obtain

$$\tan(\phi) = \frac{U^2}{Rg \cos(\beta)}. \quad (4.66)$$

During the turn, the craft will have an angular velocity about the center of rotation equal to U/R . In a perfect turn, the desired yaw rate of the craft has to be equal:

$$\dot{\psi}_d = \frac{U}{R} \quad (4.67)$$

In order to achieve the desired yaw rate, the body frame angular velocities has to be controlled. According to Fossen (2011), the angular velocities are related to the Euler-angle rates by the equation

$$\begin{bmatrix} p \\ q \\ r \end{bmatrix} = \begin{bmatrix} 1 & 0 & -s\theta \\ 0 & c\phi & c\theta s\phi \\ 0 & -s\phi & c\theta c\phi \end{bmatrix} \begin{bmatrix} \dot{\phi} \\ \dot{\theta} \\ \dot{\psi} \end{bmatrix}. \quad (4.68)$$

Assuming the RCS is controlling θ to zero and ϕ to a constant reference given by the sideslip controller, $\dot{\phi} = \dot{\theta} = \theta = 0$, and the angular velocities during a turn with yaw rate $\dot{\psi}$ becomes:

$$p = 0 \quad (4.69)$$

$$q = \sin(\phi)\dot{\psi} \quad (4.70)$$

$$r = \cos(\phi)\dot{\psi} \quad (4.71)$$

The q velocity is necessary to keep the craft in the water plane, and it will automatically be controlled by the RCS keeping $\theta = 0$. The r velocity has to be controlled by the rudders, getting a commanded input δ_r^c from the yaw-rate controller. Combining (4.67) and (4.71), the reference for r becomes

$$r^c = \cos(\phi) \frac{U}{R}, \quad (4.72)$$

which for small angles ϕ can be approximated to

$$r^c \approx \frac{U}{R}. \quad (4.73)$$

The roll angle ϕ will automatically be controlled to the value satisfying (4.66) for $\beta = 0$, because this is the only roll angle giving no sideslip when $\dot{\psi} = U/R$.

Alternatively, a feed-forward reference signal can be added to the reference signal coming from the sideslip controller. This might give better performance in the response of changes in R . ϕ might reach the optimal position faster since it do not have to wait for a sideslip to occur before the reference is changed. However, dependent on the tuning, a fast change in the reference of ϕ might give too fast responses and overshoot decreasing the passenger comfort.

Chapter 5

Results

Two different cases are simulated: one where the craft is driving straight forward without any command to actively perform a turn, and one where the craft is commanded to perform a coordinated turn with radius of 100 m. For the case when the craft is driving in a straight line, simulations in three different sea conditions will be performed: long-crested, regular waves, long-crested irregular waves and short-crested irregular waves. For each sea condition is the craft simulated in both following and head sea. The case with coordinated turn will only be simulated in short-crested irregular waves.

All simulations are done with the following initial conditions:

- $p_n = 0$ m
- $p_e = 0$ m
- $p_d = -2.5$ m
- $\phi = 0$ deg
- $\theta = 0$ deg
- $\psi = 0$ deg
- $u = 17$ m/s
- $v = 0$ m/s
- $w = 0$ m/s
- $p = 0$ deg/s
- $q = 0$ deg/s
- $r = 0$ deg/s

In all simulations the reference values for θ and v are zero, and the reference value for p_d is $-h_0 = -2.5$ m (p_d is defined as positive downwards). The reference value for ϕ will in the case of straight-line motion be zero, and for the case with coordinated turn it depends on the controller of sway velocity. The reference for r depends on turning radius, or is set equal to zero if no turn is performed. The controllers derived in Chapter 4 are used. Surge speed is kept constant in $U_0 = 17$ m/s, which equals approximately 33 knots (remark that

it may differ a bit in the first seconds of the simulation due to the initializing of the surge-speed controller). In many of the simulations, some of the states being plotted have some large fluctuations during the first seconds of the simulation. These are transient responses due to integrator build-up in both the \mathcal{H}_2 controller and in the external controllers with integral gains. Since this study is focusing on control in cruise conditions with constant speed, transient responses in the first seconds of the simulations will be neglected, and the plots will be zoomed in to focus on the results of interest. We have chosen to plot the actual, generalized deviations in the foil angles, and not the signals from the controller. The difference is the actuator dynamics. The reason is that there are the actual angles of the foils that affects the forces acting on the craft, and they are therefor more suitable to compare with the responses of the craft.

5.1 Driving Straight Forward

Simulations of the craft driving straight forward in direction north for 50 seconds. The side-slip controller is disconnected from the system, and the yaw-rate controller is active with the reference rate $r_d = 0$ rad/s. To change between following and head sea, the propagation direction of the waves is changed between 0° and 180° , respectively.

5.1.1 Regular Long-Crested Waves

Simulation with regular long-crested waves propagating in the north direction (0°), with amplitude $\zeta_a = 0.7$ m and frequency $\omega = 0.86$ rad/s. The chosen frequency equals approximately the peak frequency of the PM spectrum for $U_{19.4} = 10$ m/s, see Figure 2.8. The amplitude is chosen such that the energy of the wave approximately equals the total wave energy in the same PM spectrum.

Following Sea

Figure 5.1 plots the down position, roll angle and pitch angle for the craft when sailing in following sea with long-crested, regular waves. The performance seems good, with less than half a centimeter error in the heave position and almost no error in roll and pitch. Sensor noise is causing small fluctuations. Figure 5.2 plots the velocity components, which all stays small. Figure 5.3 plots the accelerations. There is some acceleration in roll and pitch when sensor noise is on. For pitch acceleration less than $1 \text{ deg/s}^2 = 0.0175 \text{ rad/s}^2$, the bow and stern of the craft will experience vertical accelerations less than $12 \cdot 0.0175 = 0.21 \text{ m/s}^2$. Figure 5.4 plots the actual control angles. For pitch and heave they follows sinus curves according to the encounter frequency of the waves. The two control angles have a phase shift of 90° . The sum of the control angles shows that the maximum absolute value for single foil angle is inside the range where linear lift-force can be assumed

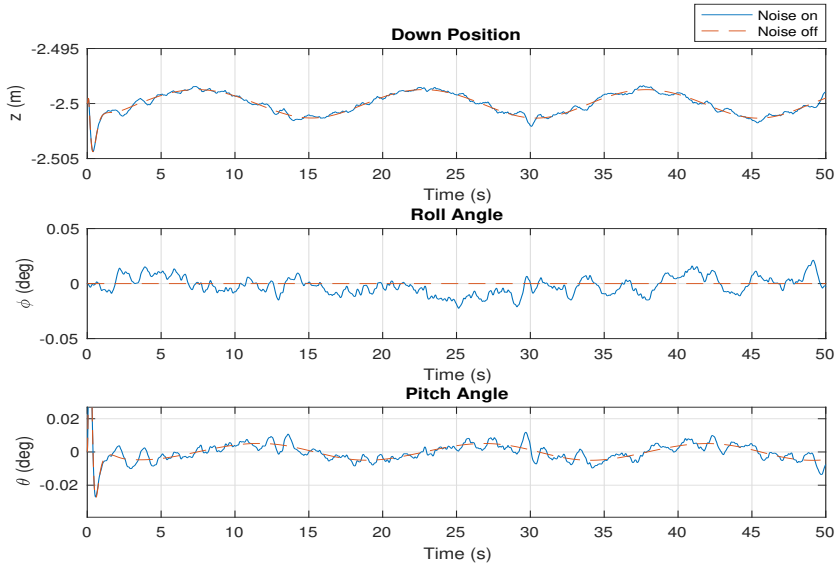


Figure 5.1: Evolution of Heave, Roll and Pitch, when sailing in following sea with regular, long-crested waves

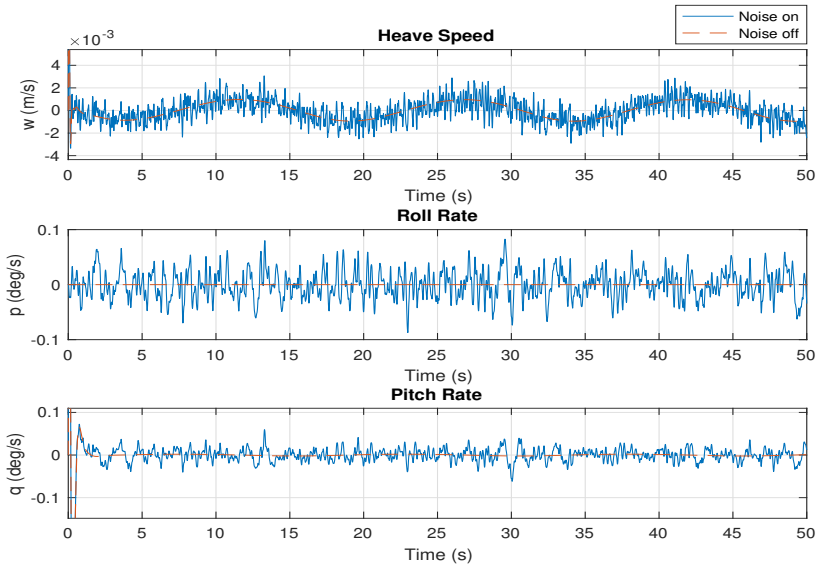


Figure 5.2: Evolution of Heave Speed, Roll Rate and Pitch Rate, when sailing in following sea with regular, long-crested waves

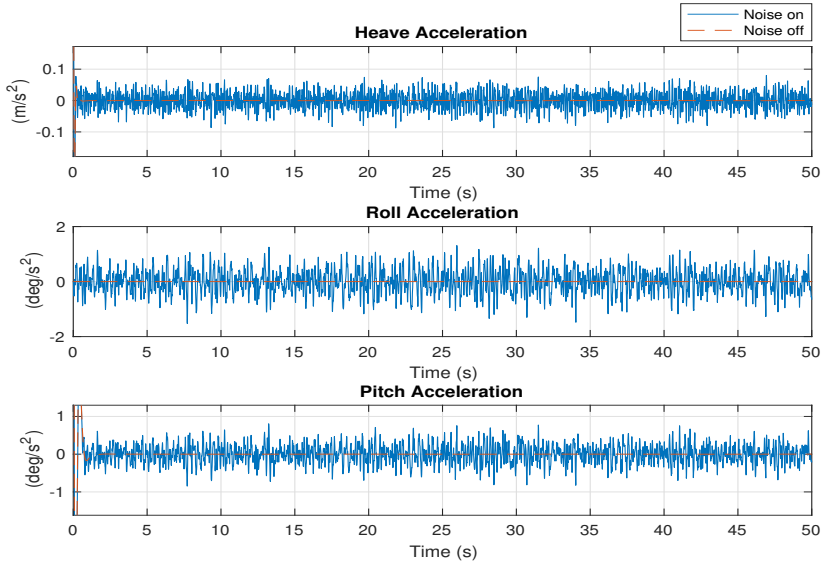


Figure 5.3: Evolution of Heave Acceleration, Roll Acceleration and Pitch Acceleration, when sailing in following sea with regular, long-crested waves

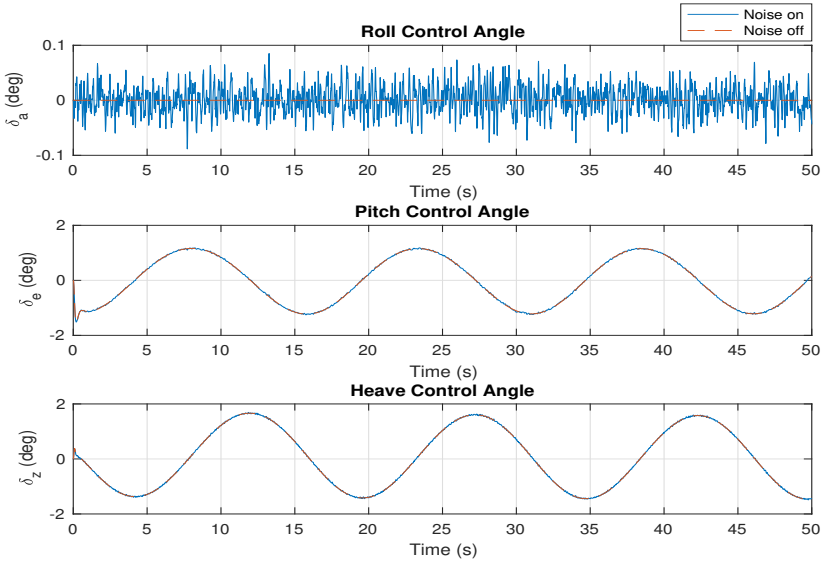


Figure 5.4: Evolution of deviations in foil angles giving forces/moments in Roll, Pitch and Heave, when sailing in following sea with regular, long-crested waves

Head Sea

Figure 5.5 plots the down position, roll angle and pitch angle for the craft when sailing in head sea with long-crested, regular waves. The performance is a bit less good compared to following sea, but still good, with approximately half centimeter error in the heave position and almost no error in roll and pitch. Sensor noise is causing small fluctuations. Figure 5.6 plots the velocity components. They are all small, but the pitch rate shows a sinusoidal evolution, which was not the case in following sea. Figure 5.7 plots the accelerations. Also here, the acceleration has a more sinusoidal shape. Otherwise, not very different from the case of following sea, with the same limitations in vertical acceleration at the bow or the stern of the craft. Figure 5.8 plots the actual control angles. Approximately same magnitudes and phase shift as for following sea, but higher frequency due to higher encounter frequency. Sum of the control angles shows that maximum absolute value for single foil angle is inside the range where linear lift-force can be assumed.

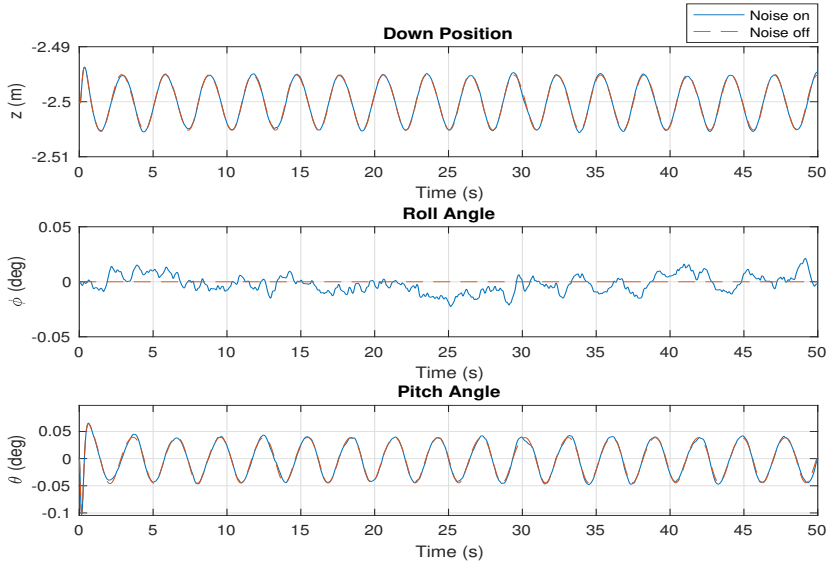


Figure 5.5: Evolution of Heave, Roll and Pitch, when sailing in head sea with regular, long-crested waves

5.1.2 Irregular Long-Crested Waves

An irregular sea state is simulated according to theory and methods provided in Section 2.5. A Pierson-Moskowitz frequency spectrum with 100 frequency components, for wind speed $U_{19,4} = 10$ m/s has been used. The components are uniformly distributed inside the

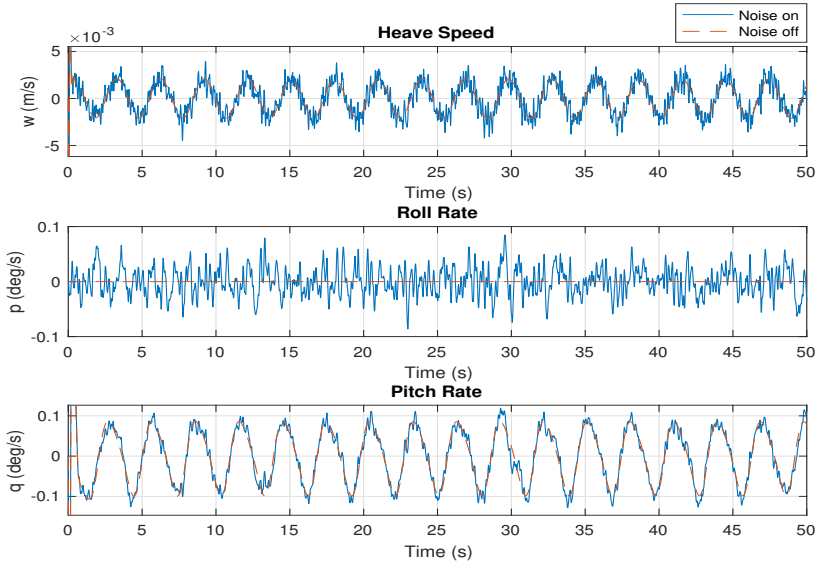


Figure 5.6: Evolution of Heave Speed, Roll Rate and Pitch Rate, when sailing in head sea with regular, long-crested waves

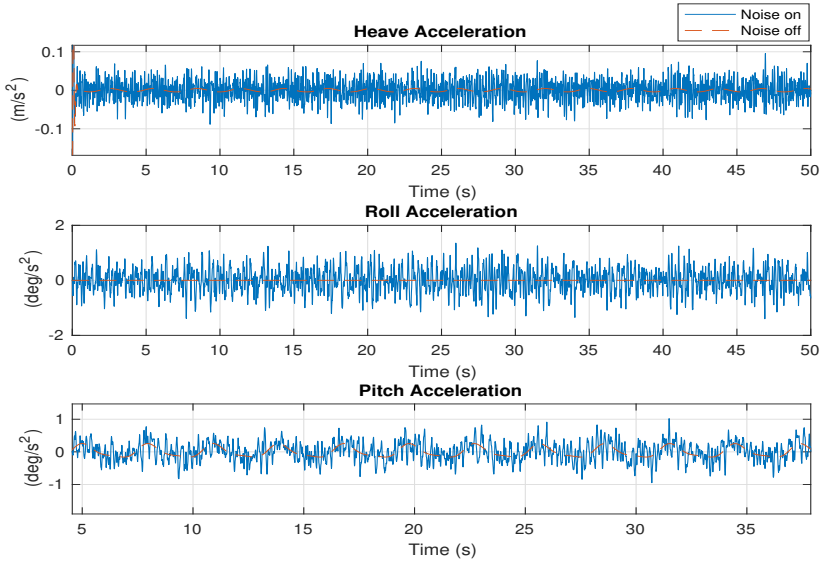


Figure 5.7: Evolution of Heave Acceleration, Roll Acceleration and Pitch Acceleration, when sailing in head sea with regular long-crested waves

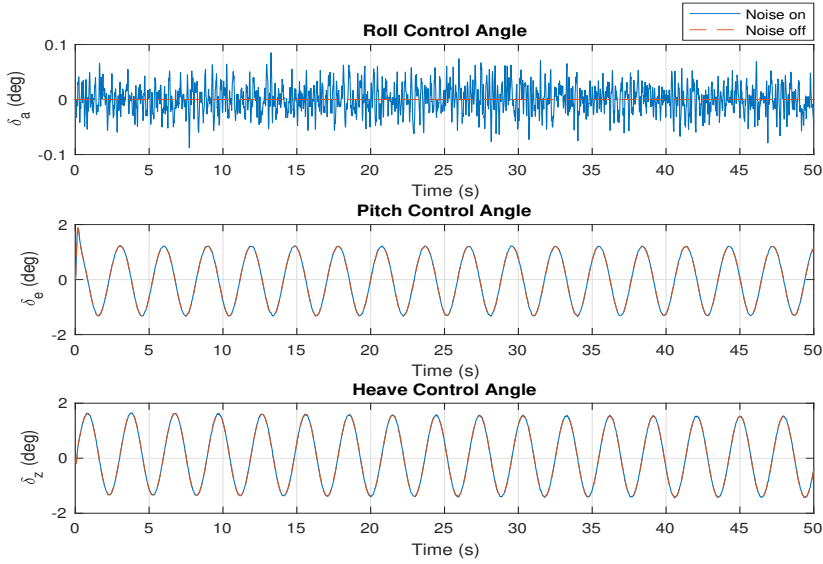


Figure 5.8: Evolution of deviations in foil angles giving forces/moments in Roll, Pitch and Heave, when sailing in head sea with regular, long-crested waves

range where $S(\omega) > 0.05$, and each component has a random phase angle between 0 and 360 degrees.

Following Sea

Figure 5.9 plots the down position, roll angle and pitch angle for the craft when sailing in following sea with long-crested, irregular waves. Also here, the performance seems good, with less than one centimeter error in the heave position, less than 0.05° error in pitch, and almost no error in roll. The irregularities of the waves are causing significant irregularities in the down and pitch position. Figure 5.10 plots the velocity components, where the maximum absolute heave speed is less than 0.01 m/s, and the maximum absolute pitch rate is less than 0.2 deg/s. The roll rate is zero in the case of no noise, but have high-frequency oscillations with amplitude less than 1 deg/s when noise is present. Figure 5.11 plots the accelerations. In absence of sensor noise, there are small variations in the heave and pitch accelerations, but no acceleration in roll. When sensor noise is on, there are high-frequency accelerations in all three DOF. Also here, the pitch acceleration stays less than 1 deg/s^2 , so the bow and stern of the craft will experience vertical accelerations less than 0.21 m/s^2 . Figure 5.12 plots the actual control angles. The angles controlling pitch and heave have irregular evolutions, where the first-mentioned has similarities to the evolution of heave and pitch position. Sum of the control angles shows that maximum absolute value for single foil angle is inside the range where linear lift-force can be assumed, but

with smaller margin compared to the cases with regular waves, since the maximum pitch control angle is approximately 4.5° . The roll control angle is only influenced by sensor noise, but stays small.

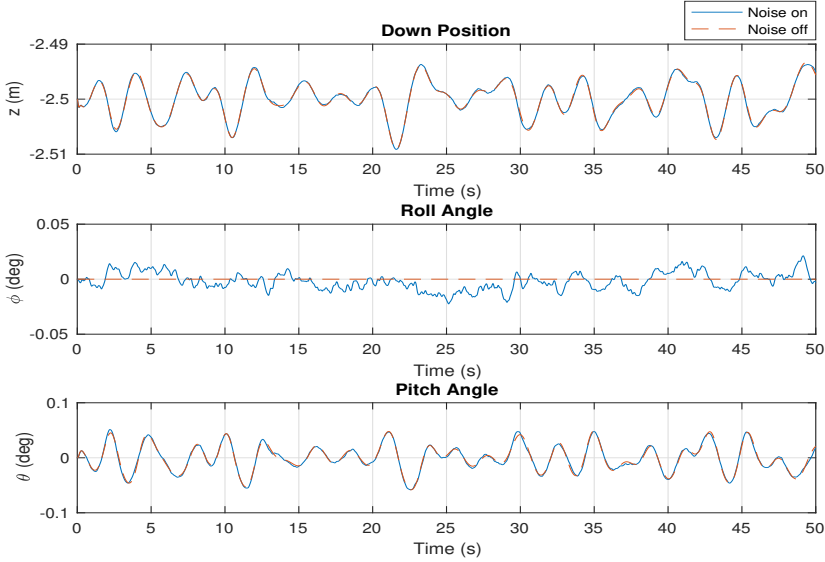


Figure 5.9: Evolution of Heave, Roll and Pitch, when sailing in following sea with irregular, long-crested waves

Head Sea

Figure 5.13 plots the down position, roll angle and pitch angle for the craft when sailing in head sea with long-crested, irregular waves. The performance is less good compared to following sea, with approximately two centimeter maximum error in the heave position and approximately 0.3 deg error in pitch. In roll there is no error when sensor noise is off, and when the noise is on it causes small fluctuations. Figure 5.14 plots the velocity components. In heave and pitch, the maximum values are significantly larger than for following sea, with a maximum heave speed of approximately 0.03 m/s, and a maximum pitch rate close to 2 deg/s. I.e. three and ten times as high, respectively. Figure 5.15 plots the accelerations. Roll acceleration is not very different from the case of following sea, but the acceleration in heave has a peak value close to 0.2 m/s^2 , which is twice as large, and the pitch acceleration has a peak value of approximately 9 deg/s^2 , which is nine times as large. For a pitch acceleration of $9 \text{ deg/s}^2 = 0.157 \text{ rad/s}^2$, the bow and stern of the craft will experience vertical accelerations of $12 \times 0.157 = 1.88 \text{ m/s}^2$, which is quite large. Figure 5.16 plots the actual control angles. Approximately same peak values as for following sea, but higher frequency due to higher encounter frequency. As for following

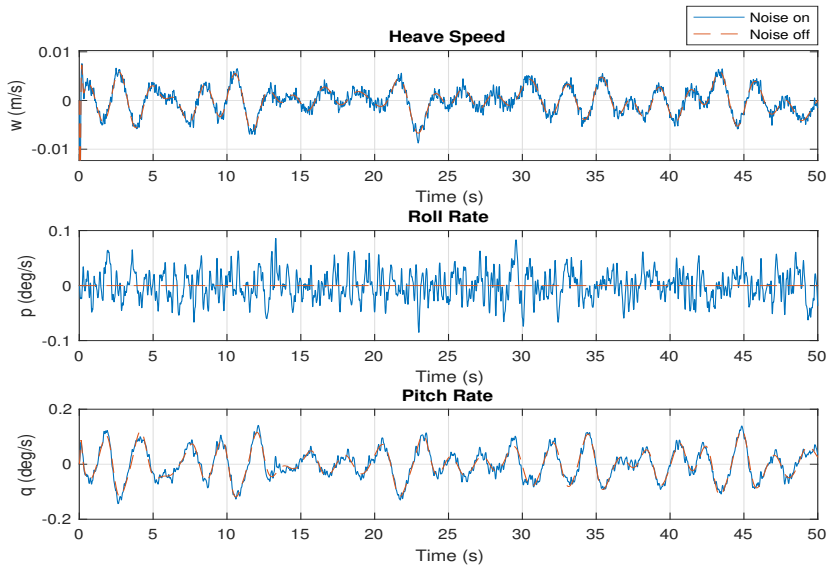


Figure 5.10: Evolution of Heave Speed, Roll Rate and Pitch Rate, when sailing in following sea with irregular, long-crested waves

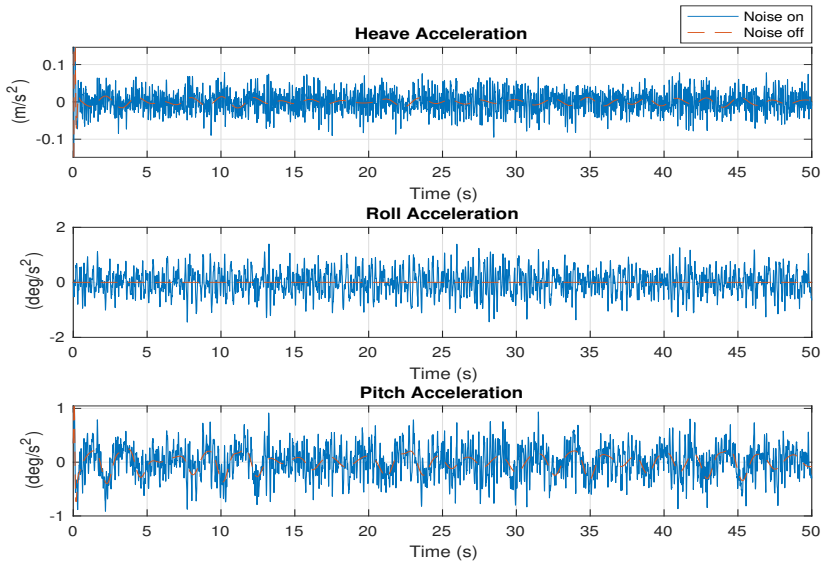


Figure 5.11: Evolution of Heave Acceleration, Roll Acceleration and Pitch Acceleration, when sailing in following sea with irregular, long-crested waves

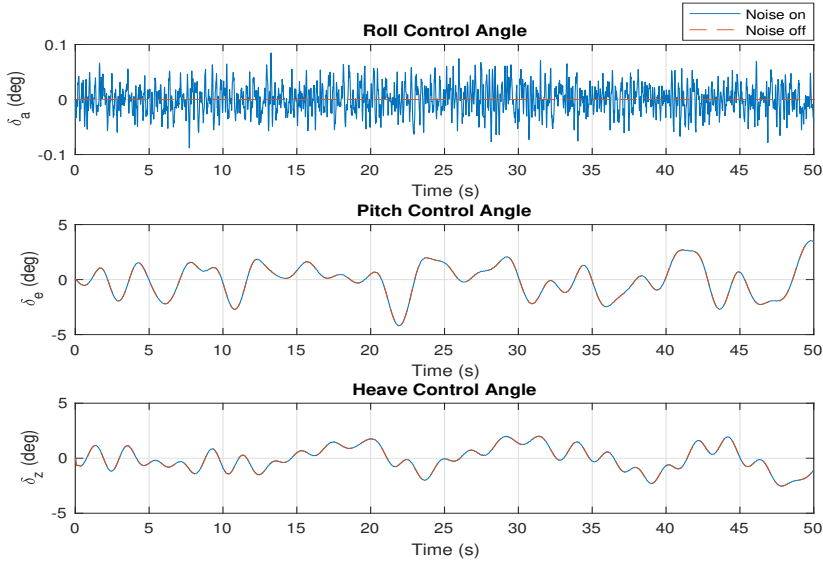


Figure 5.12: Evolution of deviations in foil angles giving forces/moments in Roll, Pitch and Heave, when sailing in following sea with irregular, long-crested waves

sea, the sum of the control angles shows that maximum absolute value for single foil angle is inside the range where linear lift-force can be assumed.

5.1.3 Irregular Short-Crested Waves

An irregular, short-crested sea state is simulated according to theory and methods provided in Section 2.5. A Pierson-Moskowitz (PM) frequency spectrum with 20 frequency components, uniformly distributed inside the range where $S(\omega) > 0.05$, is combined with a directional spectrum consisting of 5 components which are evenly distributed in the range $(-65^\circ, -65^\circ)$ relative to the mean wave-propagation direction, θ_0 . Hence, the total number of components in the wave spectrum becomes 100. Each component has a random phase angle between 0 and 360 degrees. For the PM spectrum, a wind speed of $U_{19.4} = 10$ m/s has been used. In following sea $\theta_0 = 0^\circ$, and in head sea $\theta_0 = 180^\circ$.

Following Sea

Figure 5.17 plots the down position, roll angle and pitch angle for the craft when sailing in following sea with short-crested, irregular waves. The performance seems good, with less than half a centimeter error in the heave position, and less than 0.05° error in pitch and

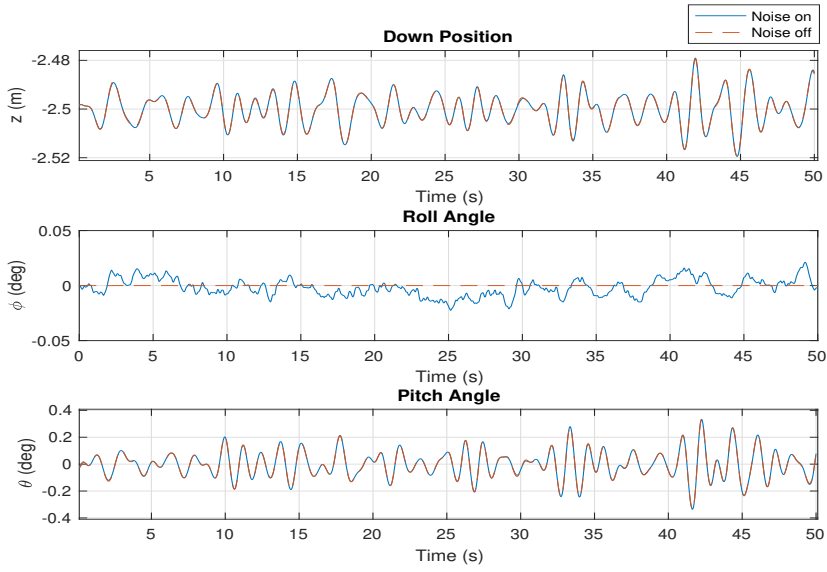


Figure 5.13: Evolution of Heave, Roll and Pitch, when sailing in head sea with irregular, long-crested waves

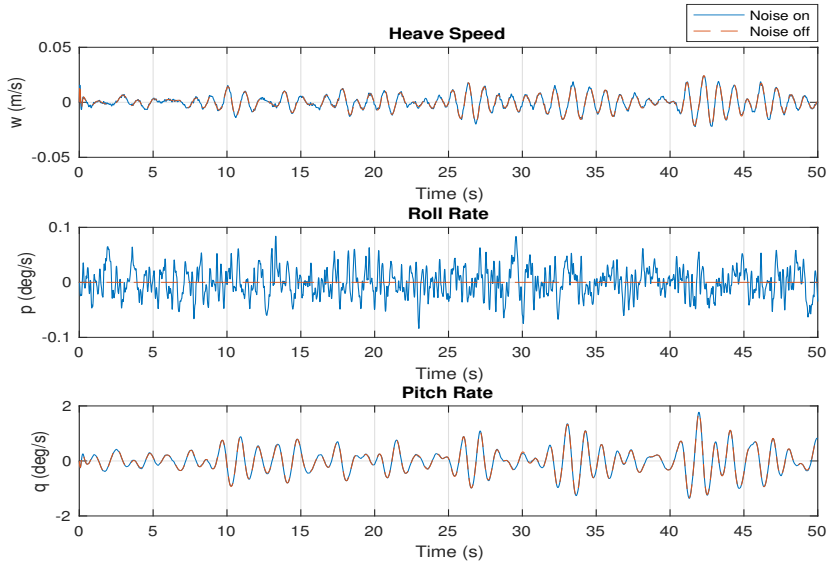


Figure 5.14: Evolution of Heave Speed, Roll Rate and Pitch Rate, when sailing in head sea with irregular, long-crested waves

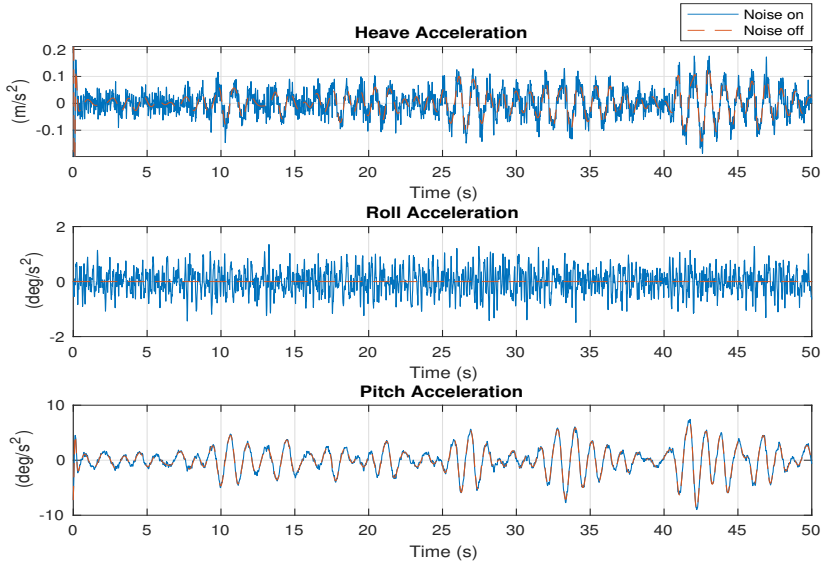


Figure 5.15: Evolution of Heave Acceleration, Roll Acceleration and Pitch Acceleration, when sailing in head sea with irregular, long-crested waves

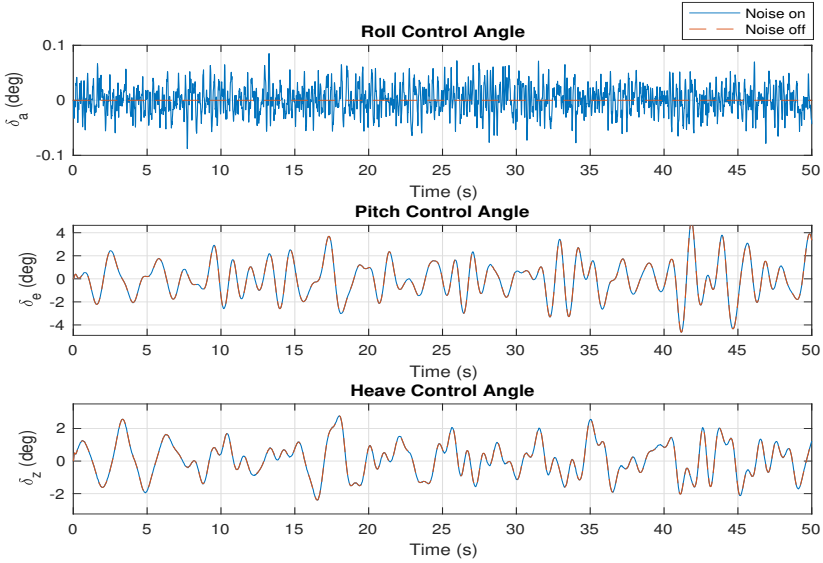


Figure 5.16: Evolution of deviations in foil angles giving forces/moments in Roll, Pitch and Heave, when sailing in head sea with irregular, long-crested waves

roll. The irregularities of the waves are causing significant irregularities in all the position components, and it can also be observed an inconsistency between the roll angles in the cases when noise was on and off. Figure 5.18 plots the velocity components, where the maximum absolute heave speed is less than 0.005 m/s, and the maximum absolute roll and pitch rates are less than 0.1 deg/s (when disregarding the transient responses in the beginning). When sensor noise is present, there are high-frequency oscillations on the top of the mean evolutions, especially for the roll rate. Figure 5.19 plots the accelerations. In absence of sensor noise, there are small variations in the pitch acceleration, but almost no acceleration in heave and roll. When sensor noise is on, there are high-frequency accelerations in all three DOF. The pitch acceleration stays less than 1 deg/s^2 , so the bow and stern of the craft will experience vertical accelerations less than 0.21 m/s^2 . Figure 5.20 plots the actual control angles. All three angles have irregular evolutions, and the roll control angle has significantly smaller magnitudes than the others. The plot of the roll control angle shows how the sensor noise is penetrating the controller. Sum of the control angles shows that maximum absolute value for single foil angle is inside the range where linear lift-force can be assumed.

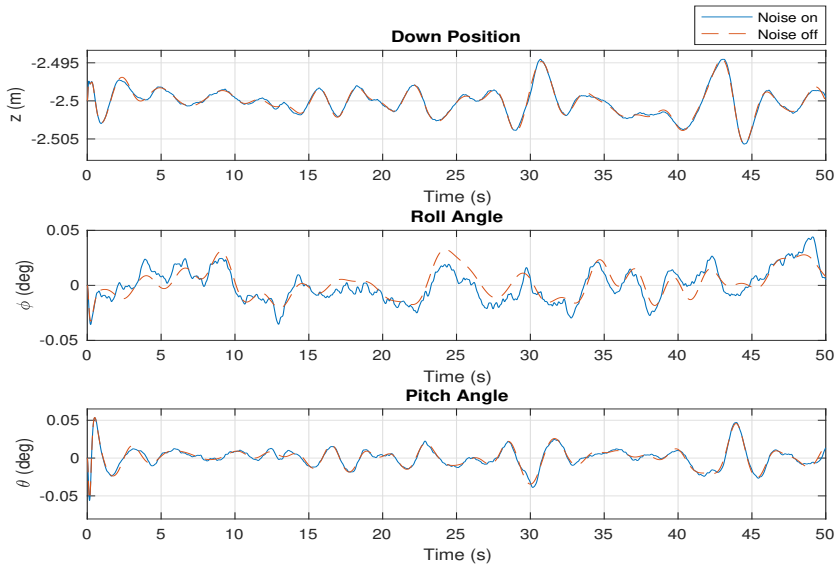


Figure 5.17: Evolution of Heave, Roll and Pitch, when sailing in following sea with irregular, short-crested waves

Head Sea

Figure 5.21 plots the down position, roll angle and pitch angle for the craft when sailing in head sea with short-crested, irregular waves. The performance is less good compared to following sea, with close to two centimeter maximum error in the heave position, ap-

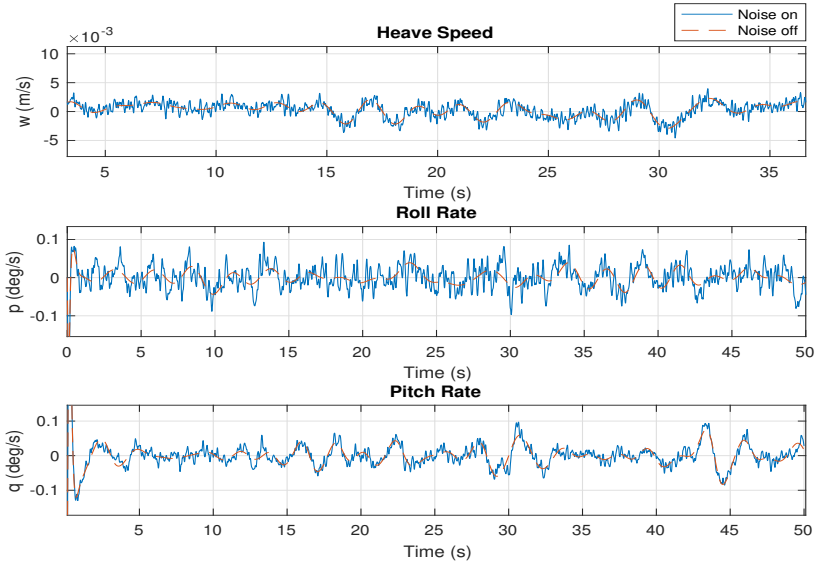


Figure 5.18: Evolution of Heave Speed, Roll Rate and Pitch Rate, when sailing in following sea with irregular, short-crested waves

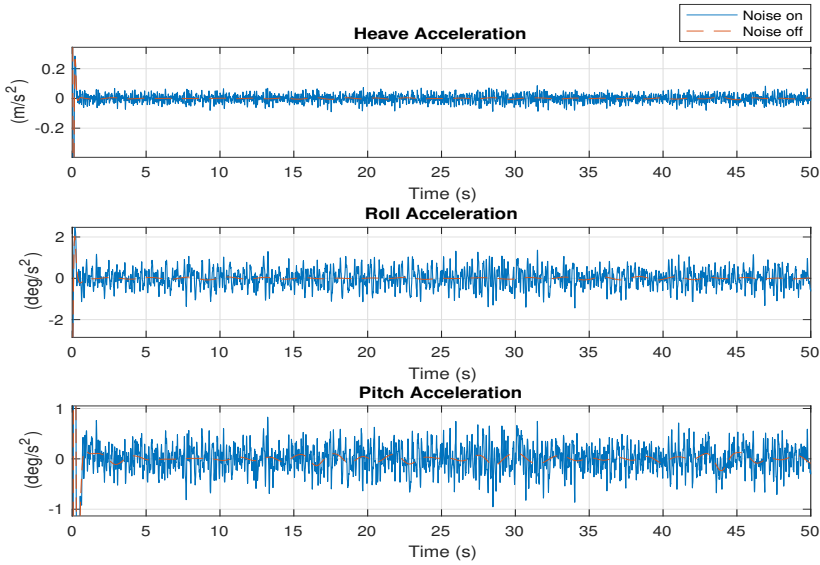


Figure 5.19: Evolution of Heave Acceleration, Roll Acceleration and Pitch Acceleration, when sailing in following sea with irregular, short-crested waves

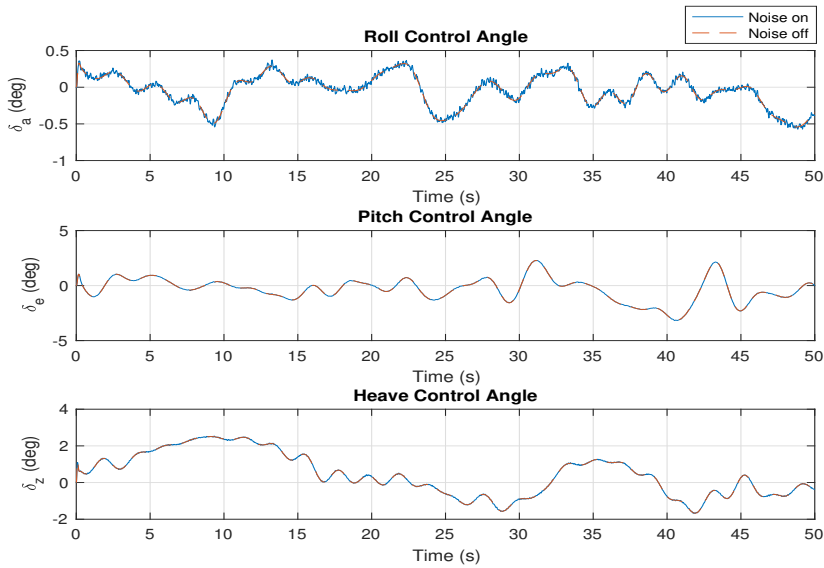


Figure 5.20: Evolution of deviations in foil angles giving forces/moments in Roll, Pitch and Heave, when sailing in following sea with irregular, short-crested waves

proximately 0.1° error in roll, and approximately 0.2° error in pitch. Figure 5.22 plots the velocity components. The maximum values are significantly larger than for following sea, with a maximum heave speed of approximately 0.01 m/s , a maximum roll rate of approximately 0.3 deg/s , and a maximum pitch rate close to 0.8 deg/s . Figure 5.23 plots the accelerations. In absence of sensor noise, there are small variations in the accelerations for heave and roll, compared to when sensor noise is on, while the difference is less for pitch. Maximum heave and roll accelerations are some higher than in the case of following sea, but the pitch acceleration has a peak value of approximately 4 deg/s^2 , which is more than four times as large as in following sea. For a pitch acceleration of 4 deg/s^2 , the bow and stern of the craft will experience vertical accelerations of 0.84 m/s^2 , which is quite large. Figure 5.24 plots the actual control angles. Peak values are higher than in the case of following sea, especially for the roll control angle, and frequency is higher due to higher encounter frequency. As for following sea, the sum of the control angles shows that maximum absolute value for single foil angle is inside the range where linear lift-force can be assumed. This is helped by a phase delay between the pitch and heave control angles, which can be observed in the last 20 seconds of the simulation.

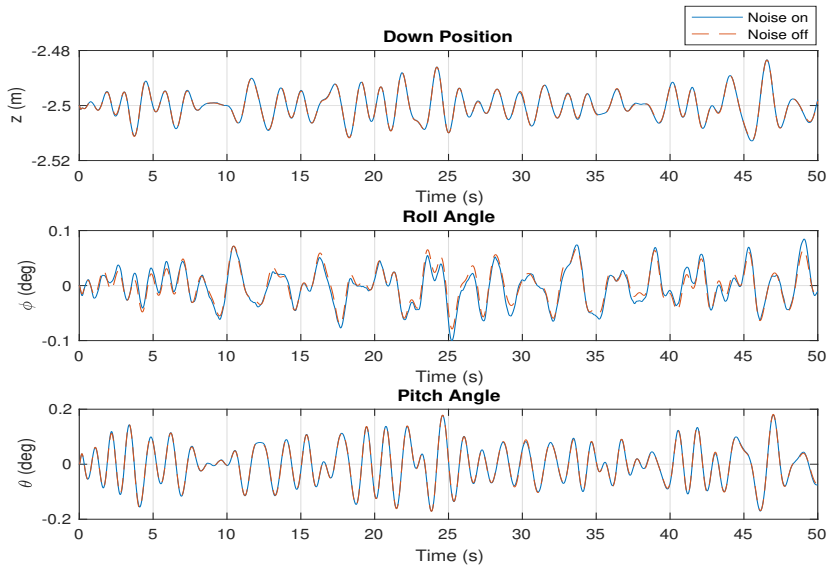


Figure 5.21: Evolution of Heave, Roll and Pitch, when sailing in head sea with irregular, short-crested waves

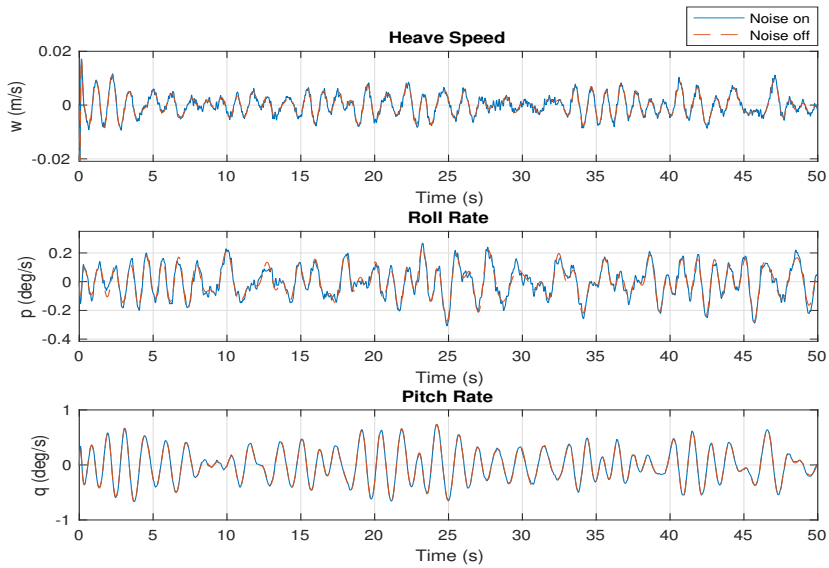


Figure 5.22: Evolution of Heave Speed, Roll Rate and Pitch Rate, when sailing in head sea with irregular, short-crested waves

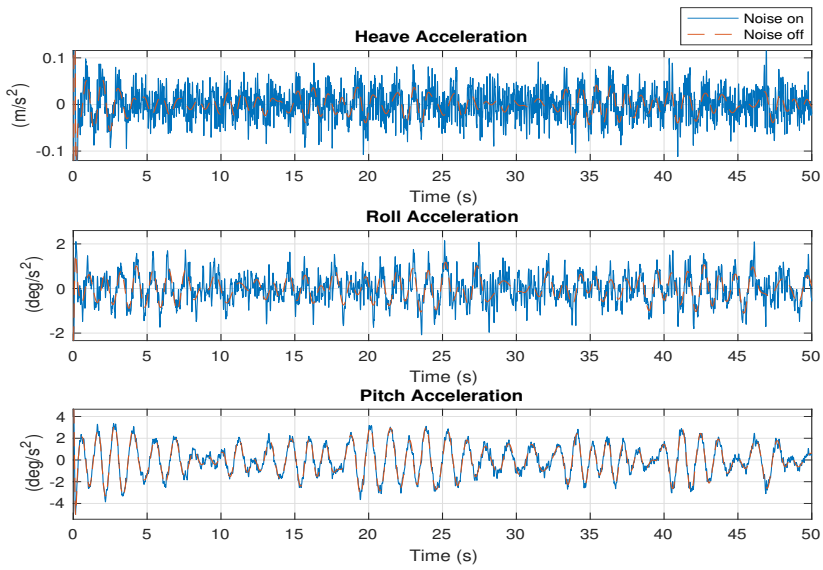


Figure 5.23: Evolution of Heave Acceleration, Roll Acceleration and Pitch Acceleration, when sailing in head sea with irregular, short-crested waves

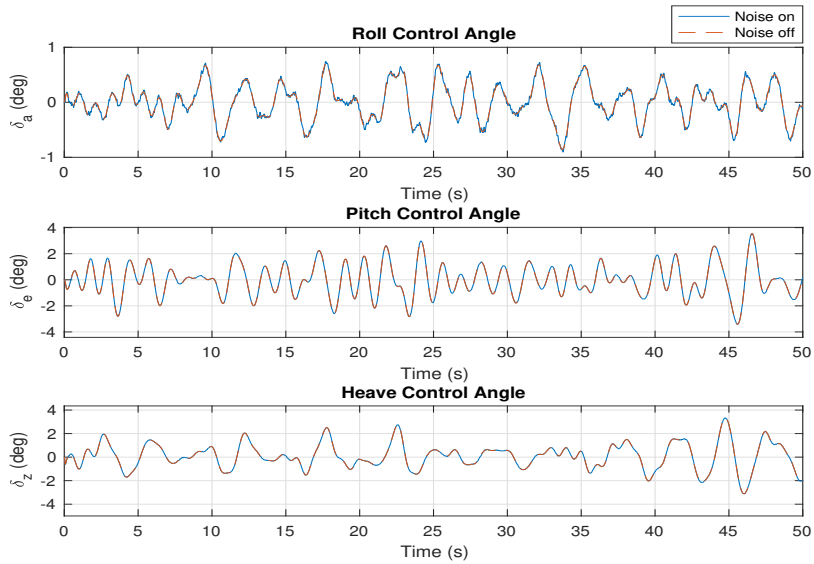


Figure 5.24: Evolution of deviations in foil angles giving forces/moments in Roll, Pitch and Heave, when sailing in head sea with irregular, short-crested waves

5.2 Turning In a Circle when Irregular Short-Crested Waves

One simulation of the craft driving in a coordinated turn with 100 meter radius. This equals a yaw rate of $r = U_0/R = 17/100 = 0.17$ rad/s, or 9.74 deg/s. The same sea state as in Section 5.1.3 will be used, i.e. irregular short-crested waves, with North as the mean propagation direction. The initial heading of the craft is North, and due to the continuous change in heading, the craft will experience both following and head sea, as well as waves coming in from the side. The total simulation has a duration of 200 seconds, in order to make a plot of the path for several rounds. However, only the first 50 seconds of the simulation data will be used when plotting the relevant states and control angles. This in order to have a good comparison to the simulations of straight-line motions.

Figure 5.25 shows the path of the craft in the North-East plane, for a simulation of 200 seconds duration. It is clear that the path does not converge into a perfect circle. Figure 5.26 plots the down position, roll angle and pitch angle for the craft. It seems clear that the mean down position is increased with five centimeters to -2.45 m, i.e. the CO of the craft is five centimeters closer to the mean water surface. The mean roll angle is increased to a mean value of approximately 17° , which is a consequence of the side-slip controller that updates the reference for roll in order to control the speed in sway to zero. For all three states, the wave-induced deviations away from the mean values seems larger than for the simulations with straight-line motion. Especially for pitch, where the maximum error is close to 1° at the time 10 seconds.

Figure 5.27 plots the velocity components. The heave speed drifts away from zero to a mean value of approximately -0.02 m/s, but the maximum wave-induced deviations away from this are of the same range as for straight-line motion in head sea with the same conditions. The roll rate has a large deviation from zero in the beginning, due to the change in the reference for the roll angle, but its mean value goes back to zero at the same time the roll angle stops increasing. After this, the maximum error is a bit larger than 1 deg/s. The mean value of the pitch rate increases to approximately 2.5 deg/s during the same time as the roll angle increases. This pitch rate different from zero is necessary according to (4.70). Deviations away from this mean value are less than 1.5 deg/s.

Figure 5.28 plots the heading, the speed in sway and the yaw rate. In the beginning, the yaw rate is increasing rapidly when the yaw-rate controller starts to act, with the consequence that the speed in sway increases due to the rotation of the craft. However, around 10 seconds into the simulation, when the roll angle increased, the sway speed goes back to a mean value around zero, with some wave-induced deviations that are less than 0.5 m/s. It can also be observed that the yaw rate is not converging perfectly to its reference value, but maintain small wave-induced deviations.

Figure 5.29 the accelerations in heave, roll and pitch. The heave acceleration has a peak value of approximately 0.1 m/s^2 when noise is on, and less when off. The roll acceleration has a peak value of approximately 2.5 deg/s^2 , and the pitch acceleration has a peak value of approximately 4 deg/s^2 , which is the same as in the case of straight-line motion in head

sea of irregular, short-crested waves. This peak value appear at the same time as the craft has a heading of approximately 200° , which equals sailing in almost head sea.

Figure 5.30 plots the actual control angles for roll, pitch and heave. For the first 10 seconds, the roll control angle is large in order to tilt the craft in direction of the desired roll angle. After that, it has a mean value of approximately zero. The control angles for pitch and heave behave like for straight-line motion in the same sea conditions, and the frequency varies with the heading. The sum of the control angles shows that maximum absolute value for single foil angle is inside the range where linear lift-force can be assumed.

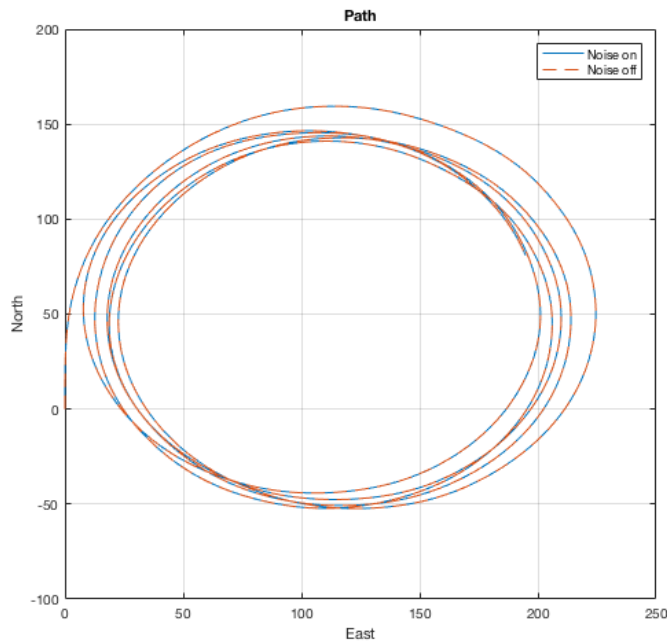


Figure 5.25: Path in the horizontal plane when driving in a circle with radius 100 m. Irregular, short-crested waves with mean direction North. Compared to results from controller designed for no sensor noise

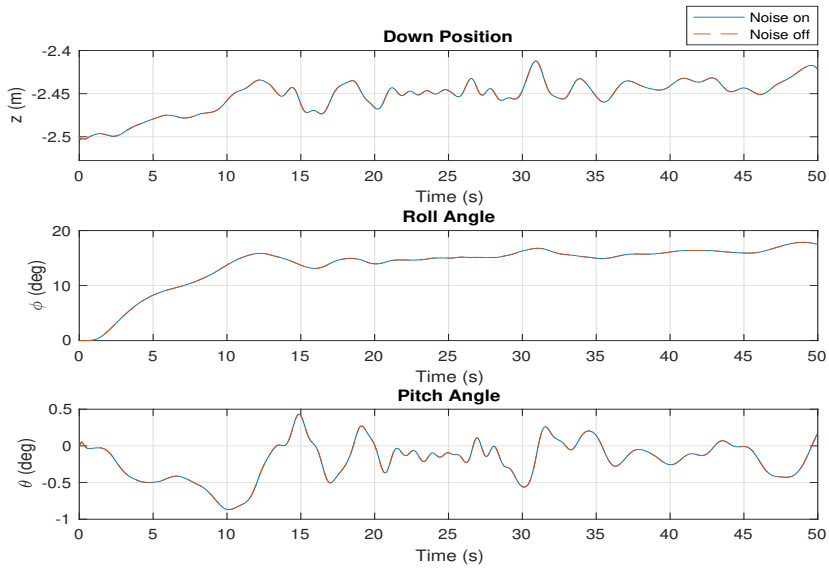


Figure 5.26: Evolution of Heave, Roll and Pitch, when sailing in a circle path, in sea with irregular, short-crested waves

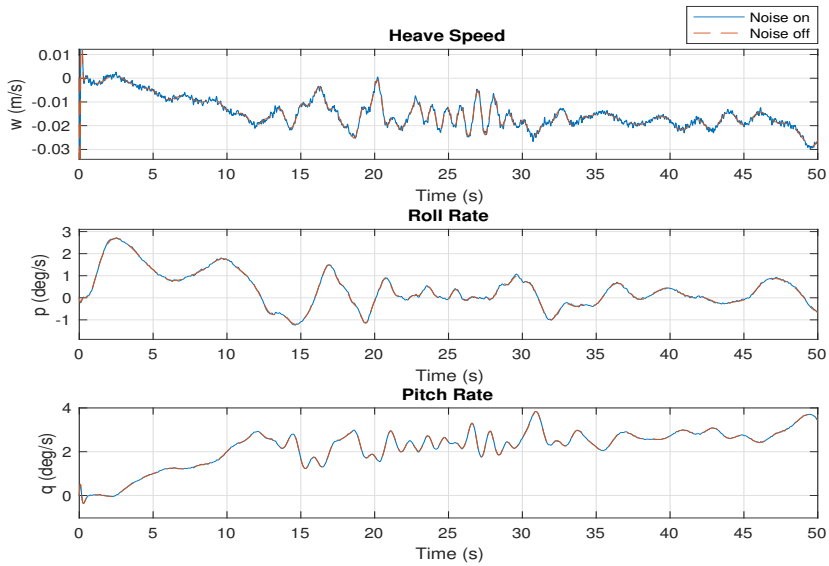


Figure 5.27: Evolution of Heave Speed, Roll Rate and Pitch Rate, when sailing in a circle path, in sea with irregular, short-crested waves

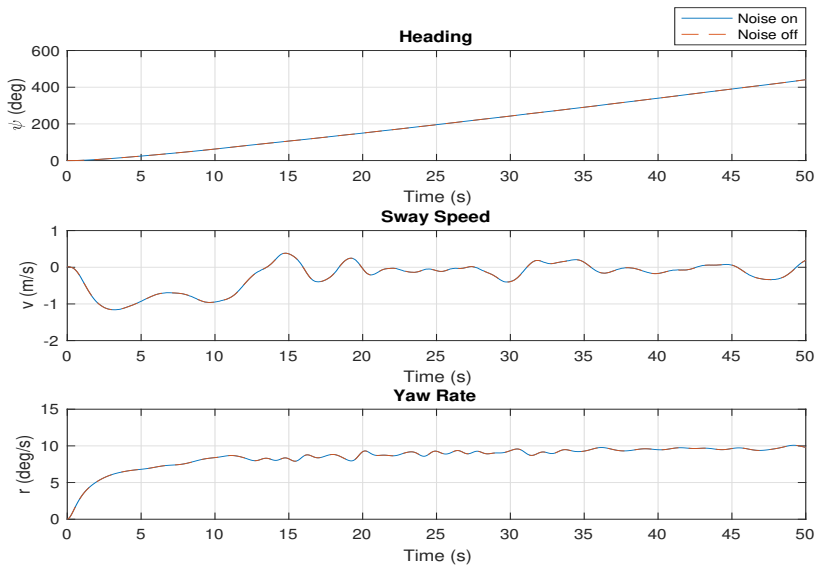


Figure 5.28: Evolution of Heading, Sway Speed and Yaw Rate, when sailing in a circle path, in sea with irregular, short-crested waves

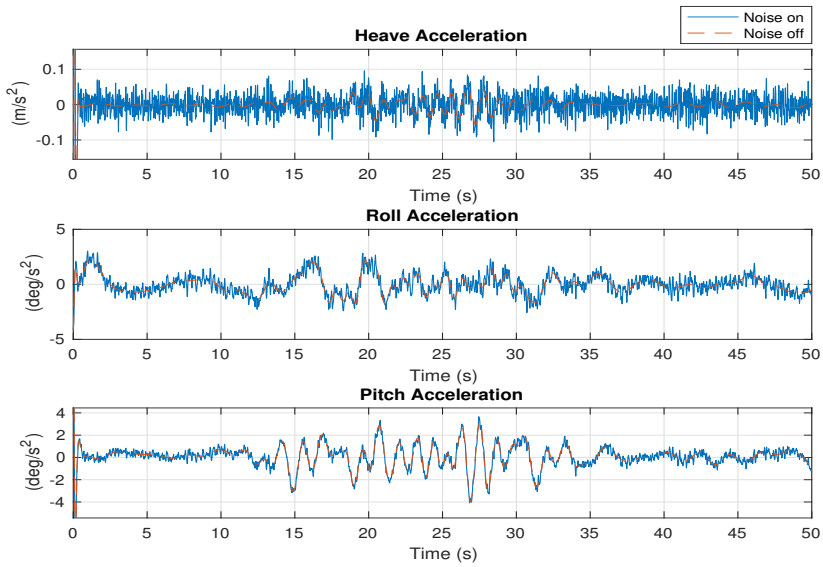


Figure 5.29: Evolution of Heave Acceleration, Roll Acceleration and Pitch Acceleration, when sailing in a circle path, in sea with irregular, short-crested waves

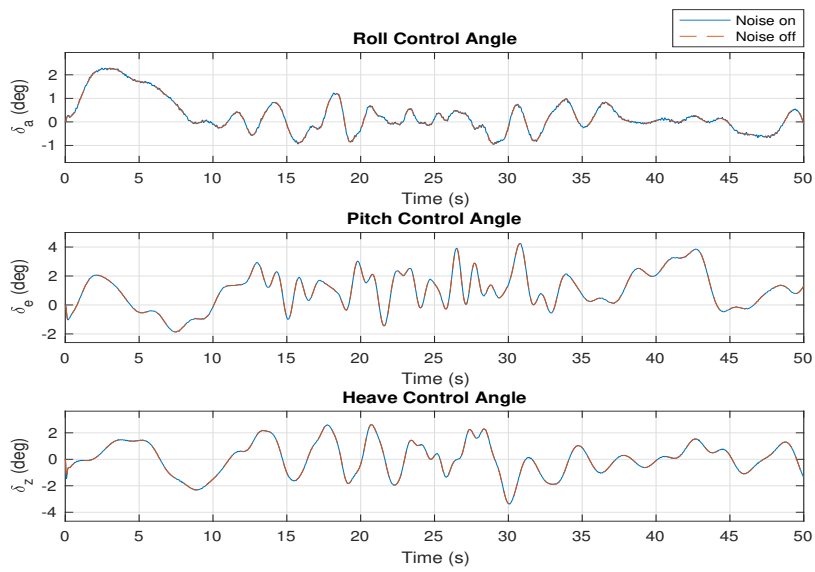


Figure 5.30: Evolution of deviations in foil angles giving forces/moments in Roll, Pitch and Heave, when sailing in a circle path, in sea with irregular, short-crested waves

Discussion

The general observations from the straight-line simulations are that the performance is better in regular than irregular waves, and it is better in following sea than in head sea. The latter is not consistent with the experiences from industry and earlier experimental studies, according to Kim and Yamato (2004). However, we have in this study not accounted for any effect of proximity to the water surface. A good explanation for less good performance in head sea is the use of frequency weighting on the performance signals, more exactly low-pass filters with a cut-off frequency of 1 rad/s. Hence, the encounter frequency in the case of head sea is inside the transition region of the low-pass filter, and will get less penalty than in the case of following sea, where the encounter frequency is lower. This is even more significant for irregular waves, where we from Section 4.1.1 know that the encounter frequency for the given sea state and craft speed can reach 13.33 rad/s. From Figure 4.5 we see that the resonance frequencies roll and pitch, and roll rate and pitch rate, due to generalized wave disturbances in pitch, are in the range 10-20 rad/s, and the peak singular values for roll and pitch rate are greater than 1. For heave is the singular value from disturbance to heave speed significantly greater, but the resonance frequency is approximately 30 rad/s. It can also be discussed whether irregular sea in some cases causes such abrupt changes in the disturbance forces that the controller consider this as disturbances with higher frequency than it is supposed compensate. More like a step input. Anyway, an abrupt change in the disturbance force is in general more difficult to handle for a feedback controller, compared to more smooth changes, like e.g. a pure sinusoidal curve. An interesting observation is the difference in maximum pitch acceleration when sailing in head sea with irregular long-crested and irregular short-crested waves. The first has a peak (absolute) value of approximately 9 deg/s^2 , while the latter has a peak (absolute) value of approximately 4 deg/s^2 . This might be because of just randomness due to the random generation of phase angles for the wave components. Another reason can be the number of frequencies, where the long-crested waves did consist of 100 different frequencies, while the short-crested waves only had 20 different frequencies. The higher number

of frequencies, the higher probability of large abrupt changes in the load. A third theory is that the wave components not propagating along the North-South axis (i.e. parallel to the mean craft velocity) will have a lower impact on the lifting foils, since the water particles velocity component parallel to the foil's x-axis, x_f , is less than their total speed. Remark that foil forces due to relative velocity parallel to the lifting foil's y-axis, y_f , are neglected in the simulation model. Hence, when parts of the wave energy is distributed over components in non-parallel direction, this will reduce the total impact on the lifting foils. A fourth explanation is that the interference between wave components with different directions causes effective encounter frequencies outside the frequency region for resonance, or the interference reduces the amplitudes of disturbance forces inside that region. Anyway, a maximum pitch acceleration of 9 deg/s^2 , giving vertical accelerations of 1.88 m/s^2 at the bow and the stern is quite large, and it can be further discussed whether this is more than we can accept on real craft transporting passengers. A possible solution to reduce the accelerations is to include them as additional states in the augmented state-space model and let the performance vector \mathbf{z}_1 also include these states with a desired frequency weighting.

The performance during the coordinated turn was less good compared to straight line motions. This is probably due to the roll angle θ and yaw rate r deviating too much away from zero, such that the linearized model, and hence also the estimation performed by the \mathcal{H}_2 controller becomes less accurate. There are several possible ways to improve the performance in this situation. One method is to include the yaw rate and the sway velocity as states in the linearized frequency weighted model in order to optimize the control when considering all DOF, except of surge. It may also be possible to include the yaw angle ψ , but this requires a guidance system continuously updating the reference by e. g. integrating the desired yaw rate. A good reason for including the yaw rate, especially, is that the Coriolis-and-centripetal matrix of the 6 DOF model depends on it, and the Coriolis and centripetal forces becomes significant for high surge speeds. When including the yaw rate, and eventually also the sway velocity, it is obviously a good idea to also include the rudders as actuators. Further, by including all four rudders as separate actuators with separate control inputs, the control system could be even more optimized with the possibility to use the rudders to control other DOF than yaw. However, an optimized MIMO controller using more actuators will be less reliable, and should on a real craft be designed with redundancy with respect to losing one of the actuators.

We see that during the coordinated turn, the pitch rate was different from zero. According to (4.70), the craft needs to have a pitch rate different from zero when both the derivative of the heading angle ψ and the roll angle ϕ are different from zero. It is good that controller did not force q back to zero, even though $q_d = 0$ was the reference. Another observation was the change in the down position, p_d , and the heave speed, w . We see that the pitch angle was negative for the first 14 seconds, which explains why the down position changed in the first place. Further will the vertical component of the lift force from a lifting foil be reduced for a roll angle $\phi \neq 0$. This should be compensated by the RCS increasing the control input for heave, and according to (4.65) will this give the horizontal force component necessary to obtain the desired centripetal acceleration. However, we see that the errors in down position and heave speed are of opposite sign, so the heave control input from one will equalize the heave control input from the other. The error could have

been removed by designing the controller with an integrator feedback for the position states. This solved the problem for Hatzakis and Sclavounos (2006), which also simulated a hydrofoil craft without restoring forces. For the \mathcal{H}_2 -controller, this could be implemented by including states for integrated position errors in the augmented state-space model, and included these in the performance output \mathbf{z}_1 . However, the error in down position was not large compared to the height of the craft, and for a real craft it would anyway be a good idea to place CO more close to the water surface when tilting in roll, since we do not want the foils to get too close to the water surface. Since the craft stayed stable for both straight-line motions and coordinated turn with 100 m turning radius, we can assume it also will for coordinated turns with longer radii. However, we cannot assume the same for shorter radii, since this involves larger ϕ , q and r , and makes our linear model less accurate.

When comparing results from simulations with and without sensor noise, we see that the noise has an influence of the most of the states and control angles. Especially for the accelerations, and for the roll angle, roll rate and roll control angle in the simulations of the craft sailing in a straight-line. It seems like the \mathcal{H}_2 controller is not able to filter away all the sensor noise when estimating the state vector of \mathbf{x} , so some noise is penetrating the controller, where it gets amplified and causes noisy signals of control inputs. The most of the noise in these control signals is filtered away in the actuator dynamics, which actually work as a low-pass filter, but there are still some high-frequency vibrations in the foil angles, and hence also the control forces. Since the accelerations are directly related to the control forces, they will also experience high-frequency vibrations, while the velocity components, which are the integrals of the accelerations, have smaller vibrations. The vibrations are even more reduced for the down position and roll and pitch angles, while heading, sway speed and yaw rate are not directly affected, since we in this study are providing the external controllers with perfect measurements.

The process of selecting the weighting matrices $\mathbf{W}_y(s)$ and $\mathbf{W}_u(s)$, as well as the gain matrix for sensor noise, \mathbf{W}_v , was challenging. The goal was to select a cut-off frequency for $\mathbf{W}_y(s)$, ω_y , high enough to penalize wave induced state errors, but not high-frequency errors due to sensor noise and unmodelled dynamics, and let the cut-off frequency for $\mathbf{W}_u(s)$, ω_u , be a bit higher in order to penalize control inputs with higher frequencies. However, when selecting too high values for ω_y or the performance gain A_p , a lot of high-frequency sensor noise penetrated the \mathcal{H}_2 controller and caused really noisy control signals. This gave very good performance with almost no state errors, but we cannot expect that the actuators on a real hydrofoil craft is handling these high-frequency vibrations. This could be counteracted by further increasing the noise gain A_v in the gain matrix for sensor noise, \mathbf{W}_v , but this gave bad performance and instability in some simulations with coordinated turn in irregular waves. Decreasing ω_u did not have any good effect on removing the noise from the control inputs, but rather decreased the performance for high-frequency wave loads. In the end, we had to go for a trade-off where we allowed some noise penetrating the controller, but with small impact on the actual control angles of the foils, and where the performance not was optimal in all situations, e.g. in irregular head sea. A possible solution of the problem will be to implement higher order frequency-weighting functions for the performance signals, in order to narrow the transition regions. Hence, less high-frequency sensor noise will have impact on the performance signals in

\mathbf{z}_1 , such that higher values for ω_y and/or A_p can be used. However, higher order low-pass and high-pass filters will have a larger phase shift (Sørensen, 2013). Since the process of selecting the weighting functions was a trial and error method, there is no guarantee that the selected cut-off frequencies and gains were the optimal choices, and there might exist first order weighting functions getting rid of the problem with noise penetration. We also have to remark that when a too high value of A_v is giving bad performance, it seems like the linearized model is not enough accurate to make good estimations of the states subject to control.

Further we have to look at the limitations of the RCS we have designed. It was designed under the assumption of a constant surge speed of $u = U_0 = 17$ m/s, but for a real hydrofoil craft in commercial traffic it will probably be desirable to operate in different surge speeds. E.g. it may be desirable to have a lower speed in rough sea conditions compared to calm water, both due to safety and passenger comfort. However, recall that the lift forces are modelled as $F_L = \frac{1}{2}\rho S V_\infty^2 C_L(\alpha_r)$, so the surge speed has an important impact on how large control angles are necessary in order to achieve a given lift force. A hybrid control system with multiple controllers designed for different nominal surge speeds is a possible solution. These controllers will require a robustness design with respect to the parametric uncertainty in u in order to guarantee stability and performance when u is different from the nominal values. The method of Robust Multiple Model Adaptive Control can be used (Hassani et al., 2011). Anyway, since the RCS we designed only guarantee performance and stability for the nominal plant model, i.e. the linearized model assuming a trim condition of $\phi = \theta = v = w = p = q = r = 0$ and $u = U_0$, it will be necessary to include robustness design if an \mathcal{H}_2 controller, or another controller assuming a linear plant, is going to be applied on the real *Flying Foil* hydrofoil craft in the end. As we can see from the simulation results, there will always be some deviations away from the trim condition due to disturbances or reference signals different from the trim condition. There will also be some unmodelled dynamics not included in the linearized model. A possible method is to use mixed- μ synthesis in order to guarantee robustness and a desired performance for a given range of parametric uncertainty and unmodelled dynamics (Athans, 2004).

It is also worth to emphasize that we in this study only has simulated a limited number of possible wave loads, and we have neither performed simulations where wind loads and/or currents are acting on the craft at the same time as the wave loads. Hence, we have no guarantee that the RCS designed in this study will give the satisfying performance, or keep the craft stable, in such situations.

Conclusions and Further Work

7.1 Conclusions

Based on the results obtained in this study, we can draw the following main conclusions:

- The frequency weighted \mathcal{H}_2 -optimized feedback controller for heave, roll and pitch was able to control the attitude of, and reduce wave-induced disturbances on, a 6 DOF simulation model of a fully submerged hydrofoil craft, both when sailing in straight line motions and when performing a coordinated turn. The yaw rate, and the speed in surge and sway were controlled by external, independent controllers.
- Sensor noise is penetrating the controller, and affects the actuators, for the first-order weighting functions used. A trade-off between performance and low noise penetration was necessary. Higher order weighting functions or a more accurate linearized model of the craft can reduce the problem.
- Low-pass frequency weighting of the performance signal for state errors gave less good performance in head sea than in following sea, due to the necessary choice of a cut-off frequency lower than the encounter frequencies in head sea. It also made it more difficult to handle abrupt disturbances in head sea with irregular waves.
- In general best performance in long-crested, regular waves, and least good performance in long-crested, irregular waves.
- Less good performance during coordinated turns than for straight-line motions, because of nonzero roll angle, pitch rate and yaw rate.

The conclusions above are limited to the simulations performed in this study. No guarantee of the same performance or stability for different sea conditions or sharper turns.

7.2 Further Work

In the further work in developing the control system for *Flying Foil*, a deeper study into the following topics will be of great interest:

- Try to solve the problem with noise penetration by using higher order weighting functions.
- Studying whether penalty on states representing acceleration can reduce the pitch acceleration in irregular head sea, without giving bad performance in other states or instability.
- Designing the frequency weighted \mathcal{H}_2 controller for a case where only states we expect can be measured, are measured. Compare the performance with a system measuring all states subject to control.
- Study whether the position in heave can be measured with e.g. a laser rangefinder measuring the distance to the water surface, for then designing an \mathcal{H}_2 controller with a band-pass frequency-weighting function on the sensor noise for the given measurement, in order to filter away the influence from the waves and estimate the distance to the mean surface. An external processing unit with notch filtering removing the wave frequencies can also be used. This can also be used for a smooth transition between platforming in short waves and contouring in long waves.
- Designing a frequency weighted \mathcal{H}_2 or \mathcal{H}_∞ -optimal controller, which is robust with respect to parametric uncertainties and unmodelled dynamics. The mixed- μ synthesis can be used.
- Using nonlinear control theory in order to design a feedback controller which do not require a linearized model of the hydrofoil craft, and where stability can be theoretically proved. Further comparing the performance of this with the linear feedback controllers.
- Study whether a feed-forward controller, in combination with sensors and an observer estimating the incoming waves, can increase the performance in irregular sea.
- Assemble a simulation model with higher fidelity, including air resistance, added-mass forces and hydrodynamic resistance from foil struts and other submerged parts. It is also of interest to model the craft with a more realistic shape and mass distribution, as well as a configuration of foils that is different in the front and the aft. A high-fidelity model should also include more accurate hydrodynamics of the foils, including moments, change in lift and drag coefficients due to rotation of the foils, and the effect of the front foils affecting the water entering the aft foils. Using flaps as actuators instead of changing the angle of attack should also be considered.

Bibliography

- Athans, M., 2004. Viewgraphs on design of robust multivariable feedback control systems. Tech. rep., ISR/IST, Lisbon.
- Bai, J., Kim, Y., 2010. Control of the vertical motion of a hydrofoil vessel. *Ships and Offshore Structures* 5 (3), 189–198.
- Beard, R. W., McLain, T. W., 2011. *Small Unmanned Aircraft: Theory and Practice*. Princeton University Press, New Jersey.
- Brødrene AA, 2017. *Trondheimsfjord I*.
URL <http://www.braa.no/trondheimsfjord-i>
- Doyle, J. C., Glover, K., Khargonekar, P. P., Francis, B. A., Aug 1989. State-space solutions to standard h_2 and h_∞ control problems. *IEEE Transactions on Automatic Control* 34 (8), 831–847.
- Faltinsen, O. M., 1990. *Sea Loads on Ships and Offshore Structures*. Cambridge University Press, Cambridge.
- Faltinsen, O. M., 2005. *Hydrodynamics of High-Speed Marine Vehicles*. Cambridge University Press, Cambridge.
- Fossen, T. I., 2011. *Handbook of Marine Craft Hydrodynamics and Motion Control*. John Wiley & Sons, Chichester.
- Hassani, V., Hespanha, J. P., Pascoal, A. M., Athans, M., 2011. Stability analysis of robust multiple model adaptive control. *IFAC Proceedings Volumes* 18 (1), 350–355.
- Hassani, V., Sorensen, A., A. M. Pascoal, M. A., 2017. Robust dynamic positioning of offshore vessels using mixed- μ synthesis modeling, design, and practice. *Oceanic Engineering* 129, 389–400.
- Hatzakis, I., Sclavounos, P. D., 2006. Active motion control of high-speed hydrofoil vessels by state-space methods. *Journal of Ship Research* 50 (1), 49–62.

-
- Kim, S.-H., Yamato, H., 2004. An experimental study of the longitudinal motion control of a fully submerged hydrofoil model in following seas. *Ocean Engineering* 31, 523–537.
- Kim, S.-H., Yamato, H., 2005. The estimation of wave elevation and wave disturbance caused by the wave orbital motion of a fully submerged hydrofoil craft. *Journal of Marine Science and Technology* 10 (1), 22–31.
- Lee, S. Y., Rhee, K. P., 2002. Design of ship motion regulators for foil catamaran in irregular sea waves. *IEEE Journal of Oceanic Engineering* 27 (3), 738–752.
- MathWorks Inc., 2017. H2 control synthesis for LTI plant. MATLAB R2017b, Robust Control Toolbox.
URL <https://se.mathworks.com/help/robust/ref/h2syn.html>
- Myrhaug, D., 2007. *Kompendium TMR4180 Marin Dynamikk: Uregelmessig sjø*. Akademika Forlag, Trondheim.
- Piene, E. B., 2017. Motion control of a hydrofoil craft, unpublished.
- Pierson, W. J., Moskowitz, L., 1963. A proposed spectral form for fully developed wind seas based on the similarity theory of s. a. kitaigorodskii. Tech. rep., U.S. Naval Oceanographic Office under contract N62306-1042.
- Steen, S., 2011. *Kompendium: TMR 4247 Marin teknikk 3 - Hydrodynamikk*. Akademika forlag, Trondheim.
- Sørensen, A. J., 2013. Lecture notes on marine control systems. Tech. rep., UK-13-76. Norwegian University of Science and Technology.

Appendix

A: Matrices in Linearized Plant

$$\mathbf{A} = \begin{bmatrix} -20.0 & 0 & 0 & 0 & 0 & 0 & 0 & 0 & 0 \\ 0 & -20.0 & 0 & 0 & 0 & 0 & 0 & 0 & 0 \\ 0 & 0 & -20.0 & 0 & 0 & 0 & 0 & 0 & 0 \\ 0 & 0 & 0 & 0 & 0 & -17.0 & 1.0 & 0 & 0 \\ 0 & 0 & 0 & 0 & 0 & 0 & 0 & 1.0 & 0 \\ 0 & 0 & 0 & 0 & 0 & 0 & 0 & 0 & 1.0 \\ 0 & 0 & -122.42 & 0 & 0 & 0 & -7.2128 & 0 & 12.383 \\ 18.787 & 0 & 0 & 0 & 0 & 0 & 0 & -1.5497 & 0 \\ 0 & 21.463 & -0.3206 & 0 & 0 & 0 & 0.0409 & 0 & -11.394 \end{bmatrix}$$

$$\mathbf{B} = \begin{bmatrix} 20.0 & 0 & 0 \\ 0 & 20.0 & 0 \\ 0 & 0 & 20.0 \\ 0 & 0 & 0 \\ 0 & 0 & 0 \\ 0 & 0 & 0 \\ 0 & 0 & 0 \\ 0 & 0 & 0 \\ 0 & 0 & 0 \end{bmatrix}$$

$$\mathbf{C} = \begin{bmatrix} 0 & 0 & 0 & 1.0 & 0 & 0 & 0 & 0 & 0 \\ 0 & 0 & 0 & 0 & 1.0 & 0 & 0 & 0 & 0 \\ 0 & 0 & 0 & 0 & 0 & 1.0 & 0 & 0 & 0 \\ 0 & 0 & 0 & 0 & 0 & 0 & 1.0 & 0 & 0 \\ 0 & 0 & 0 & 0 & 0 & 0 & 0 & 1.0 & 0 \\ 0 & 0 & 0 & 0 & 0 & 0 & 0 & 0 & 1.0 \end{bmatrix}$$

$$\mathbf{L} = \begin{bmatrix} 0 & 0 & 0 \\ 0 & 0 & 0 \\ 0 & 0 & 0 \\ 0 & 0 & 0 \\ 0 & 0 & 0 \\ 0 & 0 & 0 \\ 0 & 0 & -122.42 \\ 18.787 & 0 & 0 \\ 0 & 21.463 & -0.3206 \end{bmatrix}$$